MIMICAD TECHNICAL REPORT NO. 5

Effect of Strip Edge Shape on Microstrip Conductor Loss

by

Edward L. Barsotti

Department of Electrical and Computer Engineering
University of Colorado
Boulder, Colorado 80309-0425

Work described in this report has been supported by the Center for Microwave/Millimeter-Wave Computer-Aided Design

July 1990

Barsotti, Edward L. (M.S., Electrical Engineering)

Effect of Strip Edge Shape on Microstrip Conductor Loss

Thesis directed by Professor J. M. Dunn

The effect of strip edge shape on conductor loss in planar transmission lines, particularly microstrip, has been examined. The method of performing a loss integration on the current density of an infinitely thin strip, originally outlined by Lewin and Vainshtein, has been fully developed here and compared with available published results. A table of integration stopping distances for these calculations for various edge shapes is given. Another technique is presented to examine the relative effects of edge shape when only an inductance expression is available. The approximations upon which these results are based are discussed, and experimental verification is proposed with relevant measurement techniques described.

CONTENTS

TABLES

TABLE

FIGURES

FIGURE

CHAPTER 1

INTRODUCTION

1.1 Background

As integrated and hybrid electronic circuits operate at higher frequencies, even into the microwave region, effects such as radiation and reflections due to mismatch become increasingly important. These problems can be alleviated by using a transmission line, which has a geometry of two (or more) conductors separated in such a way as to have a constant electric field to magnetic field ratio, or characteristic impedance. One such transmission line which has become popular in microwave integrated circuits because of its ease of fabrication and use is commonly called microstrip. As seen in Figure 1.1, it consists of a strip conductor as well as a ground plane separated by an insulating substrate material.

As with any physical electronic system, microstrip has losses. These losses are especially important near frequencies of resonance and in circuit bandwidth considerations. The three types of loss in microstrip are dielectric, radiation, and conductor loss, the latter of which is the focus of this thesis. Dielectric loss is a physical property of the substrate, determined by its equivalent conductivity. Radiation loss, which includes excitation of surface wave modes along the substrate/air interface, is important mostly at discontinuities such as gaps, open ends, and bends. Both of these are discussed further in Chapter 6. Conductor loss is caused by nonideal (resistive) conductors. Similar to the

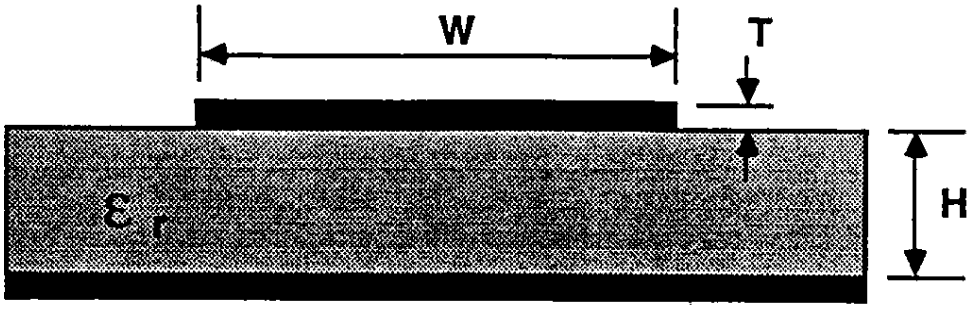

Figure 1.1. Microstrip transmission line, with strip width W and thickness T, and substrate height H and relative dielectric constant ϵ_r.

definition of dissipated power in network theory $P = I^2R$, the most general form of power lost in a conductor volume V is [1]

$$P_L = \frac{1}{2\sigma}\int_V |J_V|^2 dV, \tag{1.1}$$

where σ is the conductivity and $|J_V|$ is the volume current density.

The solution to the wave equation in a good conductor occupying a half-space $y > 0$ yields fields (and hence current density) which behave as $e^{-\gamma y}$, where y is distance from the conductor surface and the propagation constant γ is approximated by [2]

$$\gamma \approx \sqrt{i\omega\mu\sigma} = (1+i)\sqrt{\frac{\omega\mu\sigma}{2}}. \tag{1.2}$$

Therefore, the fields, current density, and conductor loss ($\sim |J|^2$) decay exponentially away from the surface. At DC (f=0), the current density will be uniform throughout the conductor, but at higher frequencies, this skin effect becomes more pronounced. Most of the current density, as well as loss, is

concentrated within a skin depth of the conductor surface. At the skin depth

$$\delta = \frac{1}{\sqrt{\pi f \mu \sigma}} = \frac{1}{\Re(\gamma)}, \tag{1.3}$$

the field magnitude has decayed by a factor $1/e$. Current density increases at a conductor corner, becoming even larger as the corner gets sharper [3],[4]. As a result, a large amount of the conductor loss occurs at the edges of the strip in a microstrip configuration. This thesis makes a careful examination of the skin effect and its associated increase in loss near various edges.

Currently, the formulas of Pucel [1], which were derived from Wheeler's incremental inductance method [5], are commonly used to calculate conductor loss for most microstrip applications, including computer-aided design (CAD) applications. These results are in closed-form and are easily utilized, while the effect of strip thickness is included in a correction term. However, the effect of edge shape is neglected, even though it is believed to be a significant factor. On the other hand, the rigorous solution of (1.1) in a real situation would require a full-wave analysis by computer, a very unreasonable, time-intensive proposition for computer-aided design. This thesis examines the effect of edge shape while, like Wheeler and Pucel, making some assumptions and approximations to (1.1) to derive a conductor loss calculation process amenable to CAD.

1.2 Approximations and assumptions

1.2.1 Quasi-TEM assumption It can be shown ([6]) that in any two perfect conductor cylindrical system with homogeneous dielectric, a purely transverse electromagnetic, or TEM, mode exists which has longitudinal field components $E_z = H_z = 0$, where z is the direction of propagation. The

propagation constant γ is the solution to

$$\gamma^2 + k^2 = 0, \quad \gamma = \pm ik = \pm i\omega\sqrt{\mu\epsilon}. \tag{1.4}$$

Since (1.4) is true, the wave equations for the transverse field components reduce to the two-dimensional Laplace's equation, and as a result the field distribution in the transverse plane is identical to the static field distribution.

When an imperfect conductor and the inhomogeneous dielectric environment of a microstrip is introduced, however, longitudinal field components E_z and H_z must result. Yet, at sufficiently low frequencies, there exists a quasi-TEM mode which closely resembles the TEM mode, since the longitudinal field components are very small compared to the transverse fields [7]. If the wavelength corresponding to the operating frequency is large compared to the transverse dimensions of the structure, this quasi-TEM assumption may be taken, implying two factors which simplify loss calculations. First, from the boundary condition on a perfect conductor [8]

$$\overline{J} = \overline{a}_n \times \overline{H}, \tag{1.5}$$

where $\overline{J}$ is a surface current and $\overline{a}_n$ is the outward unit normal vector from the conductor surface, the longitudinal magnetic field at the surface is equivalent to a transverse surface current. When H_z is ignored, the transverse surface current can also be ignored. The relative magnitude of the transverse surface current is investigated further by Kobayashi [9]. Also, the quasi-TEM assumption allows the problem to become two-dimensional, enabling static field analysis of the transmission line fields. This permits transmission line quantities such as inductance (L), capacitance (C), voltage (V), current (I), characteristic impedance (Z_o) and effective relative dielectric constant (ϵ_{re}) to be reasonably

defined. Therefore, when the quasi-TEM assumption is taken, the loss of a section of line between $z = 0$ and $z = z_o$ reduces to a two-dimensional integral on the longitudinal current

$$P_L = \frac{1}{2\sigma}\int_V |J_V|^2 dV = \frac{1}{2\sigma}\int_S |J_z|^2 \int_0^{z_o} dz\, dS = \frac{z_o}{2\sigma}\int_S |J_z|^2 dS. \qquad (1.6)$$

By removing the longitudinal length z_o, the dissipated power is expressed per longitudinal unit length.

1.2.2 Surface impedance boundary condition assumption

The surface impedance boundary condition, which is often taken in good conductors with thickness of at least a few skin depths, is assumed in the work of Chapters 2-4. This boundary condition, often called the Leontovich boundary condition [10], establishes a relationship between the fields at the surface of a highly conductive, relatively flat conductor. It eliminates the need to calculate internal fields and currents under the assumption that both decay exponentially away from the surface in a known way, thus reducing the surface integral of (1.6) to a contour integral around the conductor surface. If the current density $|J_z|$ is described by $|J_z| = |J_{sz}|e^{-y/\delta}$, where $|J_{sz}|$ is the magnitude of the current density on the surface and y the normal distance into the conductor, then (1.6) becomes the contour integral around C

$$\begin{aligned} \frac{1}{2\sigma}\int_S |J_z|^2 dS &\approx \frac{1}{2\sigma}\oint_C \int_0^{\infty} |J_{sz}|^2 e^{-2y/\delta} dy\, dl = \frac{1}{2\sigma}\oint_C |J_{sz}|^2 dl\, \frac{2}{\delta} \qquad (1.7) \\ &= \frac{1}{\sigma\delta}\oint_C |J_{sz}|^2 dl = R_s \oint_C |J_{sz}|^2 dl \end{aligned}$$

A more rigorous proof is given by Senior [11]. Here, $R_s = \frac{1}{\sigma\delta} = \sqrt{\frac{\pi f \mu}{\sigma}}$ is the surface resistance, the real part of the complex surface impedance $Z_s = (1 + i)\, R_s$, and the approximation of an infinitely thick metal is taken so

that the fields decay completely. Also assumed is that this derivation is valid completely around the conductor surface. Of course, this derivation will be inaccurate for thin strips, and of particular interest here, at points where the radius of curvature of the surface is less than 2 or 3 skin depths, such as at sharp edges. When the Leontovich condition is assumed throughout, as is commonly done by many authors including Pucel, it seems clear that the error in loss calculation will become worse as the edge shape gets sharper. Chapter 5 will further investigate its validity.

1.2.3 Perfectly conducting metal approximation A further assumption which simplifies calculation of fields and currents is that the fields at the surface, as required in (1.7), are approximately the same as when the conductor has infinite conductivity [8]. This assumption is desirable because it is easier to solve for the fields or transmission line characteristics of a system with perfect conductors. This will also allow the next approximation of an infinitely thin strip, since a perfect conductor has no field penetration. A singularity in some field components is predicted at sharp edges in a perfect conductor system ([3],[4]), and the error induced by this assumption will once again be investigated in Chapter 5. But in the next three chapters, the longitudinal current J_{sz} is assumed to be the surface current of a perfectly conducting strip.

1.2.4 Infinitely thin strip approximation In a typical microstrip system, the strip thickness T is much smaller than its width W, and the approximation of an infinitely thin strip can be taken. This does not change the fields much, except at the edges. According to [3], [4], the fields of an infinitely thin strip have an inverse square root singularity ($r^{-1/2}$, where

r is distance from the edge), while, for example, a square edge has the singularity $r^{-1/3}$. It is considerably easier to find the fields and currents of an infinitely thin strip than for a strip with nonzero thickness, and closed-form expressions are available for the longitudinal current of a infinitely thin strip in the literature ([9],[12]).

A problem arises when this approximation is used in the loss calculation around the edges. First, since the field behavior changes there, accuracy will be lost in the solution. Second, because of the inverse square root singularity in J_{sz}, integrating the current squared $|J_{sz}|^2$ will result in a logarithmic divergence. Both problems have been solved by Lewin [13] and Vainshtein [14], who independently came up with the idea of a distance, dependent only on local edge geometry, by which to avoid the edge singularity in the loss calculation on the infinitely thin strip. This distance Δ eliminates the divergence while maintaining the accuracy of the nonzero strip by virtue of its solution. It is found by comparing the loss of the actual, nonzero thickness strip with the loss of the infinitely thin strip, while maintaining all of the above assumptions. Of course, the loss calculation of the latter will diverge, and so by proposing to stop the loss integral some distance Δ short of the singularity and equating the two loss integrals, an appropriate value of Δ which depends only on local edge parameters is obtained. Because of the small dimensions around the edge, where the thickness is very much smaller than the free-space wavelength, the fields near the edge can be examined by quasi-static analysis. This statement should be true for a larger range of frequencies than the quasi-TEM assumption above. Obtaining the correct current profiles for various edge shapes, and finding the stopping distance for the edges is a task investigated in Chapter 2.

1.3 Overview of thesis

In this thesis, the effects of edge shape in microstrip are examined, and many of the concepts can be extended to other similar planar transmission lines.

In Chapter 2, a quasistatic examination of the fields near the edges of both the actual nonzero thickness strip and the infinitely thin strip is done. This is achieved by the method of conformal transformations, specifically the Schwarz-Christoffel transformation. By comparing the losses of each for various edge shapes, a table of integration stopping points is obtained.

In Chapter 3, an expression for the attenuation constant in microstrip is obtained from the simplifications of (1.1) and the integration stopping points. The total strip current is separated by Green's function technique into its components on the top and bottom of the strip. A comparison of various strip current models is done, and the closed-form expression by Kobayashi [9] is chosen. Other numerical and analytical results based on the surface impedance boundary condition, especially Pucel's formulas, are surveyed and compared with results obtained with this newly developed Lewin/Vainshtein current integration technique. Ground plane loss has been ignored in this procedure, and a justification is attempted. Finally, a comparison of losses of strips with different edges is shown.

In Chapter 4, an alternative formulation to examine the effect of edge shape on loss is developed. Instead of requiring an expression for the total current on an infinitely thin strip, a simple result is obtained by perturbation techniques which requires only an expression for the inductance of the transmission line having infinitely thin strips. What results becomes an analog

of Wheeler's incremental inductance rule. This method is demonstrated on a transmission line which does not have available closed-form current expressions, the open coplanar waveguide. Then, this technique is compared with the current integration technique of Chapter 3 to ensure that both predict similar edge effects for microstrip lines.

In Chapter 5, a careful examination of two of the assumptions is done, namely, the surface impedance boundary condition and the perfect conductor approximation. Extra losses due to sharp trapezoidal edges, as predicted in the previous chapters, seem too high, and it is believed that these assumptions fail to some degree. An examination of the current distributions of various edges is done for perfect conductors, and these results are compared with available distributions in the literature. A thorough modified surface impedance condition is formulated, and a qualitative discussion is given on its use with actual current distributions.

In Chapter 6, a proposal for experimental verification of this theory is presented. A survey of undesirable experimental losses is given. An electromagnetic scaling experiment is outlined. Ring and linear resonator measurements are contrasted, and it is shown that a linear resonator in a waveguide below cutoff is preferable. Extraction of the unloaded resonator quality factor Q_0 is demonstrated for both transmission (two-port) and reflection (one-port) measurements, and the various choices in resonator feeding mechanisms are mentioned. Finally, results of a study of experimental repeatability are discussed.

CHAPTER 2

INTEGRATION STOPPING POINTS

2.1 Introduction

In the previous chapter, a method to quickly calculate the strip portion of microstrip conductor loss was outlined, based on a series of assumptions, approximations, and perturbations. The longitudinal current density of an infinitely thin strip can be squared and integrated over the strip width, excluding small distances from each edge known as integration stopping points. In microstrip circuitry, the ground plane also contributes to the conductor loss, but this loss, as discussed in Chapter 3, will be ignored for practical microstrip circuits. The present emphasis is on the strip only, and so the described technique may be applied to similar planar lines.

In this chapter, the calculation of these integration stopping point distances (Δ) will be done. The loss in the vicinity of the edge of an actual strip will be equated with the loss of an infinitely thin strip for which the integration stops short of the edge by a small distance Δ. The result should be in terms of local edge parameters, such as shape of the edge and strip metallization thickness T, since the error incurred by taking the infinitely thin strip approximation occurs only locally at the strip edges, where the actual current deviates from the infinitely thin strip's $r^{-1/2}$ behavior. Near the strip edges, as described before, the fields behave quasi-statically, and can be approximated by static fields. Because of this, the local edge field examination can be done

by the method of conformal mapping.

2.2 Conformal mapping solution of edge static field problem

2.2.1 Static fields In the case of a static field, both the electric field $\overline{E}$ and the magnetic field $\overline{H}$ satisfy Laplace's equation in rectangular coordinates [6]

$$\nabla^2\overline{E} = \nabla^2\overline{H} = 0, \quad \frac{\partial^2\Psi}{\partial x^2} + \frac{\partial^2\Psi}{\partial y^2} + \frac{\partial^2\Psi}{\partial z^2} = 0, \tag{2.1}$$

where Ψ is any of the x, y, or z components of the fields. Since each component satisfies Laplace's equation, each is said to be a harmonic function [15]. Excluding the longitudinal variation of all fields $e^{-i\beta z}$, there is field variation only in the transverse plane, and (2.1) becomes a two-dimensional Laplace's equation. Due to the fact that the tangential electric field $\overline{E}_{tan}$ and the normal magnetic field $\overline{B}_{nor}$ are continuous at a boundary, which makes them both equal to zero at the boundary of a perfect conductor, the field solutions to $\overline{E}$ and $\overline{H}$ are orthogonal to each other [6], and are called harmonic conjugates. The same orthogonality relation exists between the scalar harmonic electrostatic (Φ) and magnetostatic (Φ_m) potentials. From these potentials the fields can be defined by [6]

$$\overline{E} = -\nabla\Phi, \quad \overline{H} = -\nabla\Phi_m. \tag{2.2}$$

Hence, at a general perfect conductor surface, the nonzero field components are $\overline{E}_{nor} = -(\partial\Phi/\partial n)\overline{a}_n$ and $\overline{H}_{tan} = -(\partial\Phi_m/\partial l)\overline{a}_l$, where $\overline{a}_n$ is the unit normal vector away from the conductor, and $\overline{a}_l$ is the unit tangential vector along the surface. From $\overline{H}_{tan}$, the longitudinal current can be obtained by the boundary condition at a perfect conductor [8]

$$\overline{J}_s = \overline{a}_n \times \overline{H} = H_{tan}\overline{a}_z = \frac{\partial\Phi_m}{\partial l}\overline{a}_z. \tag{2.3}$$

Thus the solution of the static fields near the edge can be used to obtain the local longitudinal currents. The approximation of the quasi-static nature of the edge fields should remain valid over a large range of frequencies, unlike the quasi-TEM approximation of Chapter 1. When the quasi-TEM approximation is accurate, however, the transverse field distribution is identical to the static field distribution [6]. Because of this, the transverse static field distribution obtained by conformal mapping could also be used to describe the fields of the entire strip, if it were an isolated strip. Due to the ground plane in the microstrip configuration, however, the field distribution is different than in the isolated strip, and the fields are concentrated between the bottom of the strip and the ground plane.

2.2.2 Schwarz-Christoffel conformal transformations By complex variable theory [15], a harmonic function, transformed from one domain to a second by an analytic function, is also harmonic in the second domain. In fact, both the real and imaginary parts of an analytic function are harmonic in the second domain. Consider the w-plane and z-plane, where $w = u + iv$ and $z = x + iy$. If a uniform field is established in the upper half of the w-plane, with a perfect conductor on the u-axis, the equipotential contours are $\Phi = v$ and $\Phi_m = u$, and they both satisfy Laplace's equation by being harmonic. If an analytic function transforms these coordinates to a z-plane, the w-plane orthogonal equipotential contours will be correctly mapped with their boundary conditions to z-plane equipotential contours satisfying Laplace's equation and possessing orthogonality. The gradients of the transformed magnetostatic potential function will yield the required longitudinal current functions, which can be squared and integrated along the strip surface

contour to obtain a quantity proportional to the conductor power lost. Two separate analytic mapping functions must be obtained to map the upper half of the w-plane onto both a semi-infinite nonzero-thickness strip and the corresponding infinitely thin strip. Equating the powers dissipated on both will result in the desired value of the small integration stopping distance Δ.

The Schwarz-Christoffel transformation [15] is the desired analytic mapping function. It maps the u-axis and the upper half of the w-plane onto a simple closed polygon and either its interior or exterior. In the present application, it is desired to map the region $v \geq 0$ onto the degenerate polygon of a semi-infinite strip and its exterior. The function

$$F'(w) = C_1 \prod_{j=1}^{n-1} (w - u_j)^{-k_j}, \tag{2.4}$$

where n is the number of sides of the polygon and $k_j\pi$ is the exterior angle at the vertex z_j corresponding to u_j on the u-axis, has its argument jump by the angle $k_j\pi$ to a different constant value at each point u_j. In this way, as one traverses in the positive direction along the u-axis, a side of the polygon is traversed. At each argument discontinuity point u_j, the polygon side reaches a vertex, and begins a new side. The multiplicand with the vertex at infinity can be ignored, and so, for example, the $F'(w)$ for a trapezoidal edge strip of three sides will be a product of two terms. The integral of $F'(w)$ is analytic, continuous, and single-valued everywhere in the upper half-plane $v \geq 0$, and it is the desired transformation. The constant C_1 controls the scaling and orientation of the polygon, while the integration constant C_2 controls the position of the polygon in the z-plane.

The technique of rounding a vertex is thoroughly discussed by Henrici [16]. It involves splitting the multiplicand term of the vertex of interest into a

sum of two terms, or

$$(w-u_j)^{-k_j} = a(w-u_j^{'})^{-k_j}+b(w-u_j^{''})^{-k_j}, \quad a+b=1,\ u_j^{'}=u_j-\epsilon,\ u_j^{''}=u_j+\epsilon. \tag{2.5}$$

This technique has been implemented by Vainshtein [14] to obtain the integration stopping point Δ_{circ} for the circular edge.

2.3 Solution of the integration stopping point for the 60° trapezoidal edge

The first step in finding the stopping point for a specific edge shape is to find the Schwarz-Christoffel transformations for both the zero-thickness strip and the actual nonzero-thickness strip. This technique is performed on the trapezoidal edge with a 60° corner as shown in Figure 2.1, where T is the strip thickness and d is a distance far from the edge. The transformation mapping the outside of the strip to the upper-half plane $v \geq 0$ is given by

$$z_{60}(w) = C_{1a}\int_0^w w^{2/3}(w-1)^{1/3}dw + C_{2a} \quad (60°). \tag{2.6}$$

For region $\Re(w) > 0$, which includes the top and side surfaces of the strip, the substitution $\alpha_a = \sqrt[3]{\frac{w-1}{w}}$ can be made, and the integral becomes

$$z_{60}(w) = C_{1a}\int_{-\infty}^{\alpha_a} \frac{3\alpha_a^3 d\alpha_a}{(1-\alpha_a^3)^3} + C_{2a}, \quad \Re(w) > 0. \tag{2.7}$$

By applying reduction formulas[17], the transformation becomes

$$z_{60}(w) = 3C_{1a}\left[\frac{\alpha_a}{6(1-\alpha_a^3)^2}\Big|_{-\infty}^{\alpha_a} - \frac{\alpha_a}{18(1-\alpha_a^3)}\Big|_{-\infty}^{\alpha_a} + \frac{1}{9}\int_{-\infty}^{\alpha_a}\frac{d\alpha_a}{\alpha_a^3-1}\right] + C_{2a}. \tag{2.8}$$

By dividing the region of integration of the last term of (2.8) into $-\infty$ to 0 and 0 to α, and returning back to the w variable for all but the last term of (2.9),

$$z(w) = C_{1a}[\sqrt[3]{\frac{w-1}{w}}\left(\frac{w^2}{2}-\frac{w}{6}\right)\Big|_0^w - \frac{1}{3}\int_0^1 \frac{1}{3}(w-1)^{-2/3}w^{-1/3}dw \tag{2.9}$$

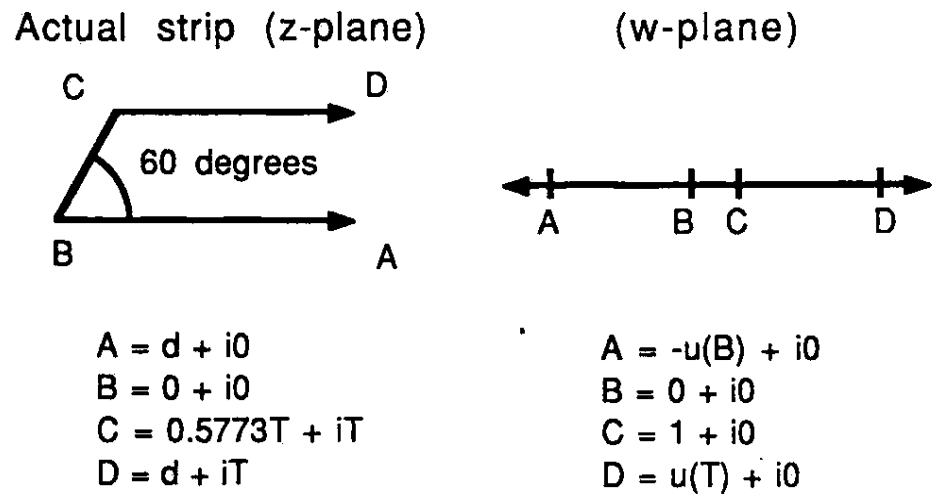

Figure 2.1: Geometry of the solution of Δ for the 60° trapezoidal edge.

$$+ \quad \frac{1}{3}\int_0^{\alpha_a} \frac{d\alpha_a}{\alpha_a^3 - 1}] + C_{2a}.$$

When a factor of $(-1)^{-2/3} = e^{-2\pi i/3}$ is extracted from the first integral term, the result is the Beta function $B(\frac{2}{3}, \frac{1}{3})$, which evaluates to $\frac{2\pi}{\sqrt{3}}$ [15]. The last term of (2.9) can be factored according to ([18])

$$\frac{t^{q-p-1}}{t^q - 1} = \frac{1}{q}\sum_{\nu=0}^{q-1} \frac{1}{t_\nu^p}\frac{1}{t - t_\nu}, \quad t_\nu = e^{2\nu\pi i/q}. \tag{2.10}$$

The integration of the separate terms is done with the arbitrary integration constant set to $-\ln(-t_\nu)$,

$$\int_0^t \frac{dt}{t - t_\nu} = \ln(t - t_\nu) + constant = \ln(1 - \frac{t}{t_\nu}), \tag{2.11}$$

so that the integral is zero when $t = 0$. Thus the transformation becomes

$$\begin{aligned} z(w) \;=\; & C_{1a}\{\sqrt[3]{\frac{w-1}{w}}\left(\frac{w^2}{2} - \frac{w}{6}\right) - \frac{2\pi}{9\sqrt{3}}e^{\frac{-2\pi i}{3}} \\ & + \frac{1}{9}\left[\ln(1-\alpha_a) + e^{\frac{2\pi i}{3}}\ln(1 - e^{\frac{4\pi i}{3}}\alpha_a) + e^{\frac{4\pi i}{3}}\ln(1 - e^{\frac{2\pi i}{3}}\alpha_a)\right]\} + C_{2a}. \end{aligned} \tag{2.12}$$

To solve for the constants according to Figure 2.1, use the transformation pairs $w = 0 \rightarrow z = 0$ and $w = 1 \rightarrow z = \frac{T}{\sqrt{3}} + iT$ to find $C_{1a} = \frac{9T}{\pi}$ and $C_{2a} = 0$. The final transformation for the region $\Re(w) > 0$ is

$$\begin{aligned} z(w) &= \frac{9T}{\pi}\sqrt[3]{\frac{w-1}{w}}\left(\frac{w^2}{2} - \frac{w}{6}\right) + \frac{2T}{\sqrt{3}}e^{\frac{\pi i}{3}} \\ &+ \frac{T}{\pi}\left[\ln(1-\alpha_a) + e^{\frac{2\pi i}{3}}\ln(1 - e^{\frac{4\pi i}{3}}\alpha_a) + e^{\frac{4\pi i}{3}}\ln(1 - e^{\frac{2\pi i}{3}}\alpha_a)\right]. \end{aligned} \tag{2.13}$$

For a point on the side or top strip surface, which transforms into $w = (u_t, 0), \quad u_t > 0 \quad (\alpha_{at} = \sqrt[3]{\frac{u_t - 1}{u_t}})$, the logarithms can be combined, with the real parts being equal to

$$\ln\left(\frac{1-\alpha_{at}}{\sqrt{1 - e^{4\pi i/3}\alpha_{at}}\sqrt{1 - e^{2\pi i/3}\alpha_{at}}}\right) = \ln\left(\frac{1-\alpha_{at}}{\sqrt{1 + \alpha_{at} + \alpha_{at}^2}}\right) \tag{2.14}$$

and the imaginary parts being equal to

$$\begin{aligned} i\frac{\sqrt{3}}{2}\ln\left(\frac{1 - e^{4\pi i/3}\alpha_{at}}{1 - e^{2\pi i/3}\alpha_{at}}\right) &= i\frac{\sqrt{3}}{2}\ln\left(\frac{1 + \frac{\alpha_{at}}{2} + i\frac{\sqrt{3}\,\alpha_{at}}{2}}{1 + \frac{\alpha_{at}}{2} - i\frac{\sqrt{3}\,\alpha_{at}}{2}}\right) \\ &= -\sqrt{3}\,\tan^{-1}\left(\frac{\alpha_{at}\sqrt{3}}{\alpha_{at} + 2}\right). \end{aligned} \tag{2.15}$$

Thus for a point on the side or top strip surface, the transformation is

$$\begin{aligned} z(u > 0) &= \frac{9T}{\pi}\sqrt[3]{\frac{u_t - 1}{u_t}}\left(\frac{u_t^2}{2} - \frac{u_t}{6}\right) + \frac{T}{\sqrt{3}} + iT \\ &+ \frac{T}{\pi}\left[\ln\left(\frac{1-\alpha_{at}}{\sqrt{1 + \alpha_{at} + \alpha_{at}^2}}\right) - \sqrt{3}\,\tan^{-1}\left(\frac{\alpha_{at}\sqrt{3}}{\alpha_{at} + 2}\right)\right]. \end{aligned} \tag{2.16}$$

The transformation of the region $\Re(w) < 0$ uses the substitution $\beta_a = \sqrt[3]{\frac{w}{w-1}}$ on (2.6) to give

$$z(w) = \frac{9T}{\pi}\int_0^{\beta_a} \frac{3\beta_a^4 d\beta_a}{(1 - \beta_a^3)^3}, \quad \Re(w) < 0. \tag{2.17}$$

Again the integral can be reduced to

$$z(w) = \frac{27T}{\pi}\left[\frac{\beta_a^2}{6(1-\beta_a^3)^2}\Big|_0^{\beta_a} - \frac{\beta_a^2}{9(1-\beta_a^3)}\Big|_0^{\beta_a} + \frac{3}{27}\int_0^{\beta_a}\frac{\beta_a d\beta_a}{\beta_a^3 - 1}\right]. \tag{2.18}$$

Since the lower limit of integration is now 0 instead of $-\infty$, there is no Beta function term which results. By (2.10) and (2.11), the last term is converted to logarithms. The final transformation for the region $\Re(w) < 0$ is

$$\begin{aligned} z(w) &= \frac{9T}{\pi}\left(\frac{w}{w-1}\right)^{2/3}\left(\frac{w^2}{2}-\frac{2w}{3}+\frac{1}{6}\right) \\ &+ \frac{T}{\pi}\left[\ln(1-\beta_a)+e^{4\pi i/3}\ln(1-e^{4\pi i/3}\beta_a)+e^{2\pi i/3}\ln(1-e^{2\pi i/3}\beta_a)\right]. \end{aligned} \tag{2.19}$$

For a point on the bottom strip surface, which transforms into $w = (u_b, 0), \quad u_b < 0 \quad (\beta_{ab} = \sqrt[3]{\frac{u_b}{u_b-1}})$, the logarithms are again combined, with the real parts being equal to

$$\ln\left(\frac{1-\beta_{ab}}{\sqrt{1-e^{2\pi i/3}\beta_{ab}}\sqrt{1-e^{4\pi i/3}\beta_{ab}}}\right) = \ln\left(\frac{1-\beta_{ab}}{\sqrt{1+\beta_{ab}+\beta_{ab}^2}}\right) \tag{2.20}$$

and the imaginary parts being equal to

$$\begin{aligned} i\frac{\sqrt{3}}{2}\ln\left(\frac{1-e^{2\pi i/3}\beta_{ab}}{1-e^{4\pi i/3}\beta_{ab}}\right) &= i\frac{\sqrt{3}}{2}\ln\left(\frac{1+\frac{\beta_{ab}}{2}-i\frac{\beta_{ab}\sqrt{3}}{2}}{1+\frac{\beta_{ab}}{2}+i\frac{\beta_{ab}\sqrt{3}}{2}}\right) \\ &= \sqrt{3}\,\tan^{-1}\left(\frac{\beta_{ab}\sqrt{3}}{\beta_{ab}+2}\right). \end{aligned} \tag{2.21}$$

The final transformation for a point on the bottom strip surface is then

$$\begin{aligned} z(u<0) &= \frac{9T}{\pi}\left(\frac{u_b}{u_b-1}\right)^{2/3}\left(\frac{u_b^2}{2}-\frac{2u_b}{3}+\frac{1}{6}\right) \\ &+ \frac{T}{\pi}\left[\ln\left(\frac{1-\beta_{ab}}{\sqrt{1+\beta_{ab}+\beta_{ab}^2}}\right)+\sqrt{3}\,\tan^{-1}\left(\frac{\beta_{ab}\sqrt{3}}{\beta_{ab}+2}\right)\right]. \end{aligned} \tag{2.22}$$

The corresponding equation for the infinitely thin strip is found from another Schwarz-Christoffel transformation integral,

$$z(w) = C_{3a}\int_0^w w dw + C_{4a}. \tag{2.23}$$

This also becomes the limiting form of (2.13) and (2.19) when $C_{3a} = C_{1u}$,

$$\begin{aligned} z(w) &= \frac{9T}{\pi}\frac{w^2}{2} \\ x(u) &= \frac{9T}{\pi}\frac{u^2}{2}. \end{aligned} \tag{2.24}$$

where the second equation is true on the strip.

The loss of the actual, nonzero-thickness strip is found by integrating $(du/dl)^2$ around the z-plane strip surfaces shown in Figure 2.1. This can be reduced to an integration of du/dl along the u-axis [13]. The parametric equations for these surfaces are $z = x + iT$ for the top, $z = x$ for the bottom, and, for the side, $z = \frac{\gamma}{\sqrt{3}} + i\gamma = \frac{2}{\sqrt{3}} e^{\pi i/3}\gamma$, since $x = \frac{y}{\sqrt{3}}$ on the side strip surface, and γ is used to parameterize the equation. Thus the power lost on the actual strip is proportional to

$$\begin{aligned} P_{1a} &= \int_d^0 \left(\frac{du}{dx}\right)^2 (-dx) + \int_0^T \frac{2}{\sqrt{3}} e^{i\pi/3} \left(\frac{du}{d\gamma}\right)^2 d\gamma + \int_{T/\sqrt{3}}^d \left(\frac{du}{dx}\right)^2 dx \quad (2.25) \\ &= \int_{-u_B}^0 \frac{du}{dx} du + \int_0^1 \frac{2}{\sqrt{3}} e^{i\pi/3} \frac{du}{d\gamma} du + \int_1^{u_T} \frac{du}{dx} du = P_{3a} + P_{4a} + P_{5a}, \end{aligned}$$

where $du/dx = du/d\gamma = \frac{\pi}{9T}(u-1)^{-1/3}u^{-2/3}$ from the reciprocal of dx/du, the derivative of (2.6). Using the same substitutions as before, the first and third terms are reduced to

$$P_{3a} = \int_0^{u_B} \frac{\pi}{9T}(u-1)^{-1/3}u^{-2/3}du = \frac{-\pi}{3T}\int_0^{\beta_{aB}} \frac{d\beta_a}{\beta_a^3 - 1} \qquad (2.26)$$

and

$$P_{5a} = \int_1^{u_T} \frac{\pi}{9T}(u-1)^{-1/3}u^{-2/3}du = \frac{-\pi}{3T}\int_0^{\alpha_{aT}} \frac{\alpha_a d\alpha_a}{\alpha_a^3 - 1} \qquad (2.27)$$

where $\alpha_T = \sqrt[3]{\frac{u_T - 1}{u_T}}$ and $\beta_B = \sqrt[3]{\frac{u_B}{u_B - 1}}$. Except for a change of variables, these terms are identical to the last terms in the expressions (2.9) and (2.18), respectively, which have already been solved. Since these integrals are along the strip surfaces, the purely real expressions in (2.14), (2.15) and (2.20), (2.21) can be used, so

$$P_{3a} = \frac{-\pi}{9T}\left[\ln\left(\frac{1-\beta_{aB}}{\sqrt{1+\beta_{aB}+\beta_{aB}^2}}\right) - \sqrt{3}\,\tan^{-1}\left(\frac{\beta_{aB}\sqrt{3}}{\beta_{aB}+2}\right)\right] \qquad (2.28)$$

and

$$P_{5a} = \frac{-\pi}{9T}\left[\ln\left(\frac{1-\alpha_{aT}}{\sqrt{1+\alpha_{aT}+\alpha_{aT}^2}}\right) + \sqrt{3}\,\tan^{-1}\left(\frac{\alpha_{aT}\sqrt{3}}{\alpha_{aT}+2}\right)\right]. \tag{2.29}$$

The second term is simply a beta function and reduces to

$$P_{4a} = \int_0^1 \frac{2\pi}{9T\sqrt{3}}\, e^{\pi i/3}(\gamma-1)^{-1/3}\gamma^{-2/3}d\gamma = \frac{2\pi}{9T\sqrt{3}}\,\frac{\pi}{\sin(\pi/3)} = \frac{4\pi^2}{27T}. \tag{2.30}$$

The corresponding loss calculation on the infinitely thin strip is

$$\begin{aligned} P_{2a} &= \int_d^{\Delta_{60}}\left(\frac{du}{dx}\right)^2(-dx) + \int_{\Delta_{60}}^{d}\left(\frac{du}{dx}\right)^2 \\ &= \int_{-u_B}^{-u_{\Delta_{60}}}\frac{du}{dx}du + \int_{u_{\Delta_{60}}}^{u_T}\frac{du}{dx}du = \frac{\pi}{9T}\ln\left(\frac{u_T u_B}{u_{\Delta_{60}}^2}\right), \end{aligned} \tag{2.31}$$

where $du/dx = \frac{\pi}{9Tu}$ is obtained by differentiating (2.24) and $u_{\Delta_{60}} = \sqrt{\frac{2\pi\Delta_{60}}{9T}}$ is the transformed value of the integration stopping point Δ_{60}. When the two values P_{1a} and P_{2a} are set equal,

$$\begin{aligned} &\frac{\pi}{9T}[\ln\left(\frac{\sqrt{1+\alpha_{aT}+\alpha_{aT}^2}}{1-\alpha_{aT}}\right) + \ln\left(\frac{\sqrt{1+\beta_{aB}+\beta_{aB}^2}}{1-\beta_{aB}}\right) + \frac{4\pi}{3} \\ &+\sqrt{3}\left(\tan^{-1}\frac{\beta_{aB}\sqrt{3}}{\beta_{aB}+2} - \tan^{-1}\frac{\alpha_{aT}\sqrt{3}}{\alpha_{aT}+2}\right)] = \frac{\pi}{9T}\ln\left(\frac{u_T u_B}{u_{\Delta_{60}}^2}\right), \end{aligned} \tag{2.32}$$

and rearranging to solve for Δ_{60},

$$\begin{aligned} \Delta_{60} &= \frac{9T}{2\pi}\{\frac{u_T u_B(1-\beta_{aB})(1-\alpha_{aT})}{\sqrt{1+\beta_{aB}+\beta_{aB}^2}\sqrt{1+\alpha_{aT}+\alpha_{aT}^2}} \\ &\quad \exp\left[\sqrt{3}\tan^{-1}\left(\frac{\alpha_{aT}\sqrt{3}}{\alpha_{aT}+2}\right) - \sqrt{3}\tan^{-1}\left(\frac{\beta_{aB}\sqrt{3}}{\beta_{aB}+2}\right) + \frac{4\pi}{3}\right]\}. \end{aligned} \tag{2.33}$$

When the magnitudes of the variables u_T and u_B are taken to be very large, corresponding to a nearly infinitely wide strip, the asymptotic value of the variable Δ_{60} is found to be $\Delta_{60} = \frac{T}{1243}$. This is the desired stopping point

Table 2.1. Values of the 60° trapezoid edge integration stopping point (Δ_{60}) vs. microstrip width over thickness (W/T).

Strip W/T	x in $\Delta_{60} = T/x$	Strip W/T	x in $\Delta_{60} = T/x$
2	1193.93	200	1242.99
4	1231.09	400	1242.99
8	1239.89	800	1242.99
20	1242.47	2000	1243.00
40	1242.86	4000	1242.99
80	1242.96	10000	1242.99

in terms of the actual strip thickness, a local edge parameter only. To find the value of Δ_{60} in actual finite width strips, the z-plane coordinates of the strip surface midpoints, $z_B = \frac{W}{2}$ and $z_T = \frac{W}{2} + iT$ (so $d = \frac{W}{2}$), can be used with transformations (2.16) and (2.22) to iteratively find values of u_T and u_B, and hence, α_{aT} and β_{aB}. These values can be used in (2.33) to obtain the altered values of Δ_{60}. In actual strips, the value of Δ_{60} does not deviate significantly from the asymptotic value, as seen in Table 2.1. This is true even in the case of a thick strip with a very small width, but in that situation, however, other assumptions upon which this loss formulation is based begins to break down. Therefore, using the value of the asymptotic Δ_{60} for all cases, instead of finding the slightly altered Δ_{60} for each geometry, can be considered a valid approximation for the 60° trapezoid case. This will also be shown to be true for the 45°, 30°, and 90° cases.

2.4 Solution of the integration stopping points for the 45°, 30°, and 90° trapezoidal edges

The Δ stopping points for the sharper trapezoids with corners of 45° and 30°, shown in Figure 2.2, were also found using similar techniques. The 90° edge, or rectangular edge, was done by this method in order to verify the

results obtained by Lewin[13] and Vainshtein[14].

The first step in each of these edges is to derive the Schwarz-Christoffel transformation mapping the outside of each of the strips to the upper-half plane $v \geq 0$. The transformations are given by

$$z_{45}(w) = C_{1b}\int_0^w w^{3/4}(w-1)^{1/4}dw + C_{2b} \quad (45°), \tag{2.34}$$

$$z_{30}(w) = C_{1c}\int_0^w w^{5/6}(w-1)^{1/6}dw + C_{2c} \quad (30°), \tag{2.35}$$

$$z_{90}(w) = C_{1d}\int_0^w w^{1/2}(w-1)^{1/2}dw + C_{2d} \quad (90°). \tag{2.36}$$

As was done for the 60° edge, the integrals are simplified by a substitution for both the $\Re(w) > 0$ and $\Re(w) < 0$ regions. For the $\Re(w) > 0$ region. these are $\alpha_b = \sqrt[4]{\frac{w-1}{w}}$, $\alpha_c = \sqrt[6]{\frac{w-1}{w}}$, and $\alpha_d = \sqrt{\frac{w-1}{w}}$ for the 45°, 30°, and 90° edges, respectively. For the $\Re(w) < 0$ region, the substitutions are $\beta_b = \sqrt[4]{\frac{w}{w-1}}$, $\beta_c = \sqrt[6]{\frac{w}{w-1}}$, and $\beta_d = \sqrt{\frac{w}{w-1}}$. Using these substitutions, as well as setting the constants C_{2b}, C_{2c}, and C_{2d} to zero as in the previous case, and using the same general reduction formulas as before, the transformations become

$$\begin{aligned} z_{45}(u>0) &= 4C_{1b}\left[\left(\frac{\alpha_b}{8(1-\alpha_b^4)^2} - \frac{\alpha_b}{32(1-\alpha_b^4)}\right)\Big|_{-\infty}^{\alpha_b} + \frac{3}{32}\int_{-\infty}^{\alpha_b}\frac{d\alpha_b}{\alpha_b^4-1}\right], \\ z_{45}(u<0) &= 4C_{1b}\left[\left(\frac{\beta_b^3}{8(1-\beta_b^4)^2} - \frac{3\beta_b^3}{32(1-\beta_b^4)}\right)\Big|_{0}^{\beta_b} + \frac{3}{32}\int_{0}^{\beta_b}\frac{\beta_b^2 d\beta_b}{\beta_b^4-1}\right], \end{aligned} \tag{2.37}$$

$$\begin{aligned} z_{30}(u>0) &= 6C_{1c}\left[\left(\frac{\alpha_c}{12(1-\alpha_c^6)^2} - \frac{\alpha_c}{72(1-\alpha_c^6)}\right)\Big|_{-\infty}^{\alpha_c} + \frac{5}{72}\int_{-\infty}^{\alpha_c}\frac{d\alpha_c}{\alpha_c^6-1}\right], \\ z_{30}(u<0) &= 6C_{1c}\left[\left(\frac{\beta_c^5}{12(1-\beta_c^6)^2} - \frac{5\beta_c^5}{72(1-\beta_c^6)}\right)\Big|_{0}^{\beta_c} + \frac{5}{72}\int_{0}^{\beta_c}\frac{\beta_c^4 d\beta_c}{\beta_c^6-1}\right], \end{aligned} \tag{2.38}$$

$$z_{90}(u>0) = 2C_{1d}\left[\left(\frac{\alpha_d}{4(1-\alpha_d^2)^2} - \frac{\alpha_d}{8(1-\alpha_d^2)}\right)\Big|_{-\infty}^{\alpha_d} + \frac{1}{8}\int_{-\infty}^{\alpha_d}\frac{d\alpha_d}{\alpha_d^2-1}\right].$$

$$z_{90}(u<0) = 2C_{1d}\left[\left(\frac{\beta_d}{4(1-\beta_d^2)^2}-\frac{\beta_d}{8(1-\beta_d^2)^2}\right)\Big|_0^{\beta_d}+\frac{1}{8}\int_0^{\beta_d}\frac{d\beta_d}{\beta_d^2-1}\right]. \tag{2.39}$$

Once again, the region of integration of each of the $\Re(w)>0$ last terms is divided into $-\infty$ to 0 and 0 to α. If the region of $-\infty$ to 0 is converted back to the w variable and a phase term extracted, Beta functions can be obtained by

$$\begin{aligned}
\int_{-\infty}^{0}\frac{d\alpha_b}{\alpha_b^4-1} &= \int_0^1(-1)^{-3/4}\frac{(1-w)^{-3/4}dw}{-4w^{1/4}} = \frac{e^{\frac{i\pi}{4}}}{4}B\left(\frac{3}{4},\frac{1}{4}\right) = \frac{\pi\sqrt{2}}{4}e^{\frac{i\pi}{4}},\\
\int_{-\infty}^{0}\frac{d\alpha_c}{\alpha_c^6-1} &= \int_0^1(-1)^{-5/6}\frac{(1-w)^{-5/6}dw}{-6w^{1/6}} = \frac{e^{\frac{i\pi}{6}}}{6}B\left(\frac{5}{6},\frac{1}{6}\right) = \frac{\pi}{3}e^{\frac{i\pi}{6}},\\
\int_{-\infty}^{0}\frac{d\alpha_d}{\alpha_d^2-1} &= \int_0^1(-1)^{-1/2}\frac{(1-w)^{-1/2}dw}{-2w^{1/2}} = \frac{e^{\frac{i\pi}{2}}}{2}B\left(\frac{1}{2},\frac{1}{2}\right) = \frac{i\pi}{2}.
\end{aligned} \tag{2.40}$$

By (2.10) and (2.11), the last terms of (2.37)-(2.39) are converted to logarithms. The constants of these equations are solved using Figure 2.2. For the 45° edge, the transformation $w=1\rightarrow z=T+iT$ leads to $C_{1b}=\frac{32T}{3\pi}$. The transformation $w=1\rightarrow z=T\sqrt{3}+iT$ makes $C_{1c}=\frac{72T}{5\pi}$ for the 30° edge, and the rectangular edge constant $C_{1d}=\frac{8T}{\pi}$ from $w=1\rightarrow z=iT$. The final transformation for the 45° edge is

$$\begin{aligned}
z_{45}(u>0) &= \frac{32T}{3\pi}\sqrt[4]{\frac{w-1}{w}}\left(\frac{w^2}{2}-\frac{w}{8}\right)+T+iT\\
&+ \frac{T}{\pi}\left[\ln\left(\frac{1-\alpha_b}{1+\alpha_b}\right)+i\ln\left(\frac{1+i\alpha_b}{1-i\alpha_b}\right)\right]\\
z_{45}(u<0) &= \frac{32T}{3\pi}\left(\frac{w}{w-1}\right)^{3/4}\left(\frac{w^2}{2}-\frac{5w}{8}+\frac{1}{8}\right)\\
&+ \frac{T}{\pi}\left[\ln\left(\frac{1-\beta_b}{1+\beta_b}\right)+i\ln\left(\frac{1-i\beta_b}{1+i\beta_b}\right)\right].
\end{aligned} \tag{2.41}$$

The transformation for the 30° edge is

$$z_{30}(u>0) = \frac{72T}{5\pi}\sqrt[6]{\frac{w-1}{w}}\left(\frac{w^2}{2}-\frac{w}{12}\right)+T\sqrt{3}+iT+\frac{T}{\pi}[\ln\left(\frac{1-\alpha_c}{1+\alpha_c}\right)$$

$$+ \quad e^{\frac{i\pi}{3}} \ln\left(\frac{1+e^{\frac{2i\pi}{3}}\alpha_c}{1-e^{\frac{2i\pi}{3}}\alpha_c}\right) + e^{\frac{2i\pi}{3}} \ln\left(\frac{1+e^{\frac{i\pi}{3}}\alpha_c}{1-e^{\frac{i\pi}{3}}\alpha_c}\right)]$$

$$z_{30}(u<0) = \frac{72T}{5\pi}\left(\frac{w}{w-1}\right)^{5/6}\left(\frac{w^2}{2}-\frac{7w}{12}+\frac{1}{12}\right) + \frac{T}{\pi}[\ln\left(\frac{1-\beta_c}{1+\beta_c}\right)$$

$$+ \quad e^{\frac{i\pi}{3}} \ln\left(\frac{1-e^{\frac{i\pi}{3}}\beta_c}{1+e^{\frac{i\pi}{3}}\beta_c}\right) + e^{\frac{2i\pi}{3}} \ln\left(\frac{1-e^{\frac{2i\pi}{3}}\beta_c}{1+e^{\frac{2i\pi}{3}}\beta_c}\right)] \tag{2.42}$$

and for the 90° rectangular edge is

$$z_{90}(u>0) = \frac{8T}{\pi}\sqrt{\frac{w-1}{w}}\left(\frac{w^2}{2}-\frac{w}{4}\right) + iT + \frac{T}{\pi}\ln\left(\frac{1-\alpha_d}{1+\alpha_d}\right) \tag{2.43}$$

$$z_{90}(u<0) = \frac{8T}{\pi}\sqrt{\frac{w}{w-1}}\left(\frac{w^2}{2}-\frac{3w}{4}+\frac{1}{4}\right) + \frac{T}{\pi}\ln\left(\frac{1-\beta_d}{1+\beta_d}\right).$$

For a point on the any of the strip surfaces ($v = 0$), the logarithm terms of (2.41),(2.42) can be combined into purely real terms, as was done in (2.14),(2.15). The resulting transformations for points on a strip surface are

$$z_{45}(u>0) = \frac{32T}{3\pi}\sqrt[4]{\frac{u_t-1}{u_t}}\left(\frac{u_t^2}{2}-\frac{u_t}{8}\right) + T + iT \tag{2.44}$$

$$+ \quad \frac{T}{\pi}\left[\ln\left(\frac{1-\alpha_{bt}}{1+\alpha_{bt}}\right) - 2\tan^{-1}\alpha_{bt}\right]$$

$$z_{45}(u<0) = \frac{32T}{3\pi}\left(\frac{u_b}{u_b-1}\right)^{3/4}\left(\frac{u_b^2}{2}-\frac{5u_b}{8}+\frac{1}{8}\right)$$

$$+ \quad \frac{T}{\pi}\left[\ln\left(\frac{1-\beta_{bb}}{1+\beta_{bb}}\right) + 2\tan^{-1}\beta_{bb}\right].$$

for the 45° edge,

$$z_{30}(u>0) = \frac{72T}{5\pi}\sqrt[6]{\frac{u_t-1}{u_t}}\left(\frac{u_t^2}{2}-\frac{u_t}{12}\right) + \sqrt{3}\,T + iT + \frac{T}{\pi}[\ln\left(\frac{1-\alpha_{ct}}{1+\alpha_{ct}}\right)$$

$$+ \quad \frac{1}{2}\ln\left(\frac{1-\alpha_{ct}+\alpha_{ct}^2}{1+\alpha_{ct}+\alpha_{ct}^2}\right) - \sqrt{3}\,\tan^{-1}\left(\frac{\alpha_{ct}\sqrt{3}}{1-\alpha_{ct}^2}\right)]$$

$$z_{30}(u<0) = \frac{72T}{5\pi}\left(\frac{u_b}{u_b-1}\right)^{5/6}\left(\frac{u_b^2}{2}-\frac{7u_b}{12}+\frac{1}{12}\right) + \frac{T}{\pi}[\ln\left(\frac{1-\beta_{cb}}{1+\beta_{cb}}\right)$$

$$+ \quad \frac{1}{2}\ln\left(\frac{1-\beta_{cb}+\beta_{cb}^2}{1+\beta_{cb}+\beta_{cb}^2}\right) + \sqrt{3}\,\tan^{-1}\left(\frac{\beta_{cb}\sqrt{3}}{1-\beta_{cb}^2}\right)] \tag{2.45}$$

for the 30° edge, and

$$z_{90}(u>0) = \frac{8T}{\pi}\sqrt{\frac{u_t-1}{u_t}}\left(\frac{u_t^2}{2}-\frac{u_t}{4}\right)+iT+\frac{T}{\pi}\ln\left(\frac{1-\alpha_{dt}}{1+\alpha_{dt}}\right) \quad (2.46)$$
$$z_{90}(u<0) = \frac{8T}{\pi}\sqrt{\frac{u_b}{u_b-1}}\left(\frac{u_b^2}{2}-\frac{3u_b}{4}+\frac{1}{4}\right)+\frac{T}{\pi}\ln\left(\frac{1-\beta_{db}}{1+\beta_{db}}\right)$$

for the rectangular 90° edge.

The corresponding equation for the infinitely thin strip in each of these three cases is identical in form to (2.24), but in each case the constant $C_{3a}=\frac{9T}{\pi}$ is replaced with the appropriate constant, either $C_{1b}=\frac{32T}{3\pi}$, $C_{1c}=\frac{72T}{5\pi}$, or $C_{1d}=\frac{8T}{\pi}$.

The power lost on the actual, nonzero-thickness strips is once again found by integrating $(du/dl)^2$ around the z-plane strip surfaces as shown in Figure 2.2, and this can be reduced to an integration of du/dl along the u-axis. The power lost on the strips with 45°, 30°, and 90° edges are

$$P_{1b} = \int_{-u_B}^{0}\frac{du}{dx}du+\int_0^1\sqrt{2}\,e^{\pi i/4}\frac{du}{d\gamma}du+\int_1^{u_T}\frac{du}{dx}du = P_{3b}+P_{4b}+P_{5b},$$
$$P_{1c} = \int_{-u_B}^{0}\frac{du}{dx}du+\int_0^1 2e^{\pi i/3}\frac{du}{d\gamma}du+\int_1^{u_T}\frac{du}{dx}du = P_{3c}+P_{4c}+P_{5c},$$
$$P_{1d} = \int_{-u_B}^{0}\frac{du}{dx}du+\int_0^1 i\frac{du}{dy}du+\int_1^{u_T}\frac{du}{dx}du = P_{3d}+P_{4d}+P_{5d}, \quad (2.47)$$

respectively, where $du/dx = du/dy = du/d\gamma = \frac{1}{C_1}(u-1)^{-\tau}u^{\tau-1}$ from the reciprocal of dx/du, as before, and the appropriate constants τ is used and C_{1b}, C_{1c}, or C_{1d} is used for C_1. When the appropriate β and α substitutions are made in the bottom strip (P_3) and top strip (P_5) terms, respectively, the integrals obtained are identical to the last terms of (2.37)-(2.39). The solutions of these integrals, found as logarithmic terms in (2.41)-(2.43), can be converted into their purely real forms since these power integrals are along strip surfaces. These terms are found in (2.44)-(2.46), and so the components of the power

due to the top and bottom strip surfaces are

$$P_{3b} = \frac{-3\pi}{32T}\int_0^{\beta_{bB}} \frac{4d\beta_{bB}}{\beta_{bB}^4 - 1} = \frac{3\pi}{32T}\left[\ln\left(\frac{1+\beta_{bB}}{1-\beta_{bB}}\right) + 2\tan^{-1}\beta_{bB}\right] \quad (2.48)$$
$$P_{5b} = \frac{-3\pi}{32T}\int_0^{\alpha_{bT}} \frac{4\alpha_{bT}^2 d\alpha_{bT}}{\alpha_{bT}^4 - 1} = \frac{3\pi}{32T}\left[\ln\left(\frac{1+\alpha_{bT}}{1-\alpha_{bT}}\right) - 2\tan^{-1}\alpha_{bT}\right]$$

for the 45° edge,

$$P_{3c} = \frac{-5\pi}{72T}\left[\ln\left(\frac{1+\beta_{cB}}{1-\beta_{cB}}\right) + \ln\sqrt{\frac{1+\beta_{cB}+\beta_{cB}^2}{1-\beta_{cB}+\beta_{cB}^2}} + \sqrt{3}\,\tan^{-1}\left(\frac{\beta_{cB}\sqrt{3}}{1-\beta_{cB}^2}\right)\right]$$
$$P_{5c} = \frac{-5\pi}{72T}\left[\ln\left(\frac{1+\alpha_{cT}}{1-\alpha_{cT}}\right) + \ln\sqrt{\frac{1+\alpha_{cT}+\alpha_{cT}^2}{1-\alpha_{cT}+\alpha_{cT}^2}} - \sqrt{3}\,\tan^{-1}\left(\frac{\alpha_{cT}\sqrt{3}}{1-\alpha_{cT}^2}\right)\right] \quad (2.49)$$

for the 30° edge, and

$$P_{3d} = \frac{-\pi}{8T}\int_0^{\beta_{dB}} \frac{2d\beta_{dB}}{\beta_{dB}^2 - 1} = \frac{\pi}{8T}\ln\left(\frac{1+\beta_{dB}}{1-\beta_{dB}}\right) \quad (2.50)$$
$$P_{5d} = \frac{-\pi}{8T}\int_0^{\alpha_{dT}} \frac{2d\alpha_{dT}}{\alpha_{dT}^2 - 1} = \frac{\pi}{8T}\ln\left(\frac{1+\alpha_{dT}}{1-\alpha_{dT}}\right)$$

for the 90° rectangular edge. The P_4 terms, representing power on the strip sides, are all Beta functions, and are found from (2.40).

For the infinitely thin strip, the corresponding loss calculation is

$$P_2 = \int_{-u_B}^{-u_\Delta} \frac{du}{dx}du + \int_{u_\Delta}^{u_T} \frac{du}{dx}du = \frac{1}{C_1}\ln\left(\frac{u_T u_B}{u_\Delta^2}\right), \quad (2.51)$$

where the appropriate C_1 is used. The desired variables u_Δ are related to the stopping points Δ by $u_{\Delta_{60}} = \sqrt{\frac{3\pi\Delta_{45}}{16T}}$, $u_{\Delta_{30}} = \sqrt{\frac{5\pi\Delta_{30}}{36T}}$, and $u_{\Delta_{90}} = \sqrt{\frac{\pi\Delta_{90}}{4T}}$ from (2.24).

When the two power values P_1 and P_2 are set equal for each of the three strips, the values of the variable Δ can be obtained. In the case of a nearly infinitely wide strip, the variables u_T and u_B can be taken to be very large,

Table 2.2. Asymptotic values of all known integration stopping points (Δ) for strips with width W and metallization thickness T.

Geometry of Strip Edge	Integration Stopping Point Δ
Rectangular (90°) Edge	$\Delta_{90} = \Delta_{rect} = T/290.8$
60° Trapezoidal Edge	$\Delta_{60} = T/1243$
45° Trapezoidal Edge	$\Delta_{45} = T/20187.3$
30° Trapezoidal Edge	$\Delta_{30} = T/54052000$
Circular Edge ([14])	$\Delta_{circ} = T/124.77$
Elliptic Strip ([13])	$\Delta_{ell} = T^2/16W$

leading to the asymptotic values of Δ. The values obtained are $\Delta_{45} = \frac{T}{20187.3}$, $\Delta_{30} = \frac{T}{54052000}$, and $\Delta_{90} = \frac{T}{290.8}$, all in terms of the strip thickness T. Table 2.2 lists all known asymptotic Δ distances. Figure 2.3 shows circular and elliptic strips. It should be noted that the stopping point for the elliptic strip is still a local parameter, since W is used to define the radius of curvature at the edge.

To find the stopping points in actual strips, once again the technique of transforming the z-plane coordinates of the strip surface midpoints, $z_B = \frac{W}{2}$ and $z_T = \frac{W}{2} + iT$ ($d = \frac{W}{2}$), and using the resultant values of u_T, u_B, α_T, and β_T, can be performed on each of the strips. As with the case of the 60° edge, the asymptotic values of Δ are good approximations. Their ranges of validity definitely will surpass the ranges of other assumptions, especially the statement that the fields of the infinitely thin strip approximate the fields of the actual strip away from the edges, which is true only for a strip width much larger ($W > 10T$) than the metallization thickness. Table 2.3 lists values for Δ_{45}, Δ_{30}, and Δ_{90} for a variety of W/T ratios.

The stopping point for the rectangular edge, Δ_{rect}, is in agreement with the results obtained by Lewin[13] and Vainshtein[14], who used slightly

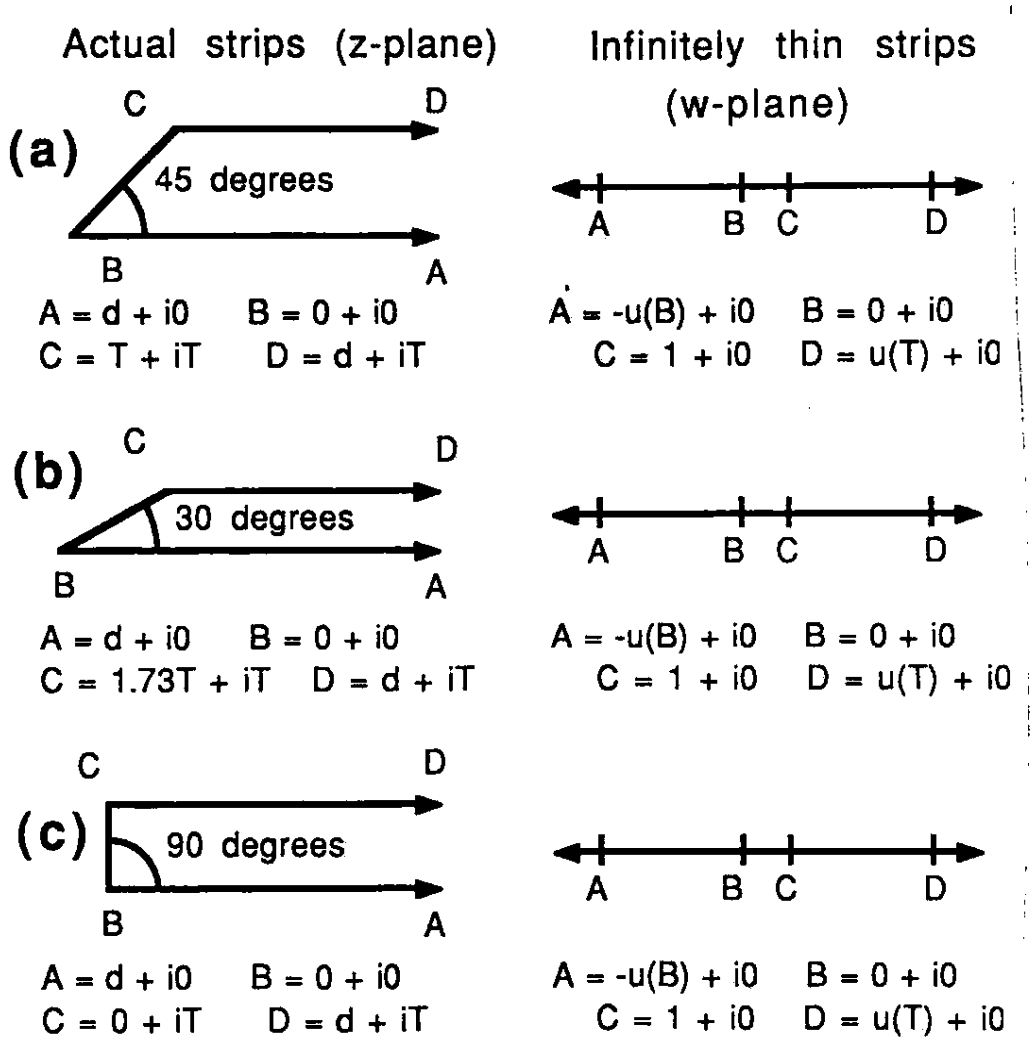

Figure 2.2. Geometry for solutions of Δ for the 45°, 30°, and 90° trapezoidal edges.

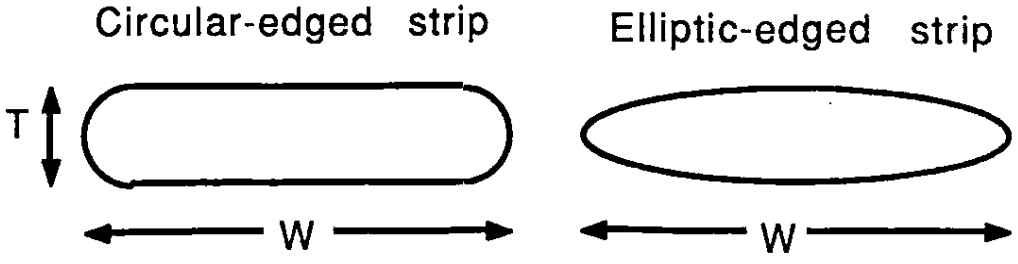

Figure 2.3: Geometries of the circular and elliptic edged strips.

Table 2.3. Values of the 45°, 30° , and 90° trapezoid edge integration stopping points vs. microstrip width over thickness (W/T).

Strip W/T	x in $\Delta_{45} = T/x$	x in $\Delta_{30} = T/x$	x in $\Delta_{90} = T/x$
2	Impossible	Impossible	325.07
4	17309.1	49638000	309.80
8	19191.7	52526000	301.02
20	19899.5	53518000	295.14
80	20138.3	53925000	291.93
200	20171.3	54001000	291.25
800	20184.3	54039000	290.91
2000	20186.4	54046000	290.84
10000	20187.4	54050000	290.80
100000	20187.3	54052000	290.78

different Schwarz-Christoffel transformations. Lewin used the transformation

$$\begin{aligned} z(w) &= C_{1c}\int_0^w \sqrt{w-1}\sqrt{w+1}\,dw + C_{2c} \\ &= \frac{T}{\pi} w\sqrt{w^2-1} - \ln\left(w+\sqrt{w^2-1}\right) \end{aligned} \tag{2.52}$$

which transforms the points $w = 1 \rightarrow z = 0$ and $w = -1 \rightarrow z = -iT$. As expected, both integral transformations result in an identical stopping point, $\Delta_{rect} = \frac{T}{290.8}$.

The results obtained for the integration stopping distances agree with intuition. At sharper edges, the current density should be larger, and as a result of squaring the current, the conductor loss should also be larger. For similar microstrips with geometries differing only in edge shape, the loss calculations will be performed on identical infinitely thin strips with identical current distributions. The only difference will be the integration stopping points. As seen in Table 2.2, the strips with sharper edges have smaller stopping distances, and as a result, will have more loss. As the trapezoidal corner becomes sharper,

however, the validity of approximations such as the surface impedance boundary condition, which is based on the assumption of a flat boundary, are subject to question. This issue will be investigated in Chapter 5. The next chapter will focus on the actual use of the stopping points in loss calculations, with comparison to other published results.

CHAPTER 3

MICROSTRIP LOSS CALCULATIONS WITH THE CURRENT INTEGRATION METHOD

3.1 Introduction

Microstrip conductor loss in a quasi-TEM planar transmission line using the standard Leontovich surface impedance boundary condition can be expressed by [1]

$$\alpha_c = \frac{R_s}{2Z_o} \oint_C \frac{|J_s|^2}{|I|^2} dl, \tag{3.1}$$

where α_c is the attenuation constant in $\frac{nepers}{meter}$ and C is the boundary of the nonzero-thickness strip cross section as in Figure 3.1a. Here R_s is the surface skin resistance, Z_o is the characteristic impedance of the transmission line, J_s is the z-directed surface current density on the longitudinally invariant ($\partial/\partial z = 0$) strip, and I is the total current of the strip. This formulation ignores the ground plane loss contribution, and this will be discussed later in this chapter. According to Lewin [13] and Vainshtein [14], this contour integral can be replaced by a line integral using an infinitely thin, perfectly conducting strip with its correspondingly simpler total longitudinal current distribution J_{zo}. This total current function includes the surface currents on both sides of the infinitely thin strip, and can not be used directly. Dividing this current into $J_{zo,top}$ and $J_{zo,bot}$, the top and bottom surface currents of the strip, respectively, the loss becomes

$$\alpha_c = \frac{R_s}{2Z_o I^2} \left[\int_{\frac{W}{2}-\Delta_r}^{\frac{-W}{2}+\Delta_l} J^2_{zo,bot}(x)(-dx) + \int_{\frac{-W}{2}+\Delta_l}^{\frac{W}{2}-\Delta_r} J^2_{zo,top}(x)dx \right]$$

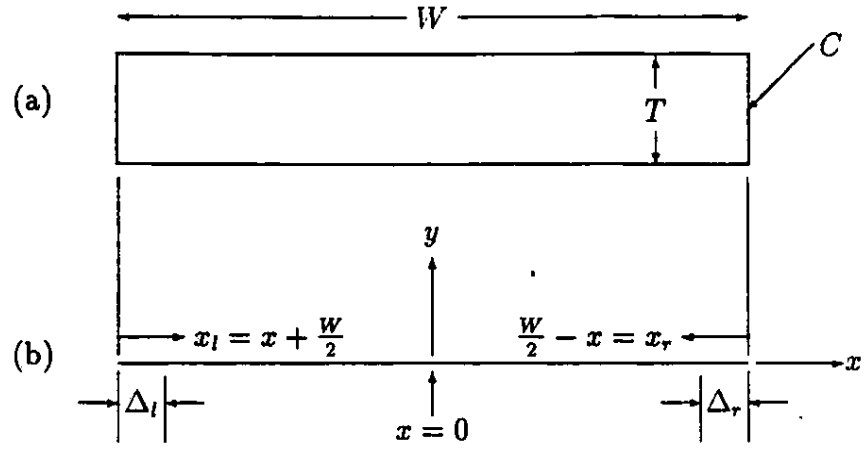

Figure 3.1. (a) Nonzero-thickness strip with a rectangular edge, an example of a general edge shape; (b) Zero-thickness strip with integration stopping points Δ_l and Δ_r (here Δ_{rect}) and Cartesian coordinates (x, y).

$$= \frac{R_s}{2Z_o I^2} \int_{\frac{-W}{2}+\Delta_l}^{\frac{W}{2}-\Delta_r} \left[J_{zo,top}^2(x) + J_{zo,bot}^2(x) \right] dx \tag{3.2}$$

where Δ_l and Δ_r are the integration stopping points for the left and right edges, respectively (see Figure 3.1b), and W is the strip width. The contour integral has been converted into a line integral by summing the top and bottom strip current components. If a line integration of J_{zo} had been incorrectly performed instead, the resulting loss would have been higher, in fact, twice as high for the case of a transmission line in which J_{zo} is equally divided such that $J_{zo,top} = J_{zo,bot} = \frac{1}{2} J_{zo}$. The division of the ideal total current J_{zo} into $J_{zo,top}$ and $J_{zo,bot}$ is dependent on the planar transmission line configuration. As an example, the currents of the microstrip line of Figure 3.2 will be separated by a Green's function technique. Qualitatively, the presence of the ground plane causes more of the field to concentrate between the strip and the ground plane, and so $J_{zo,bot}$ should exceed $J_{zo,top}$ throughout the width of the strip.

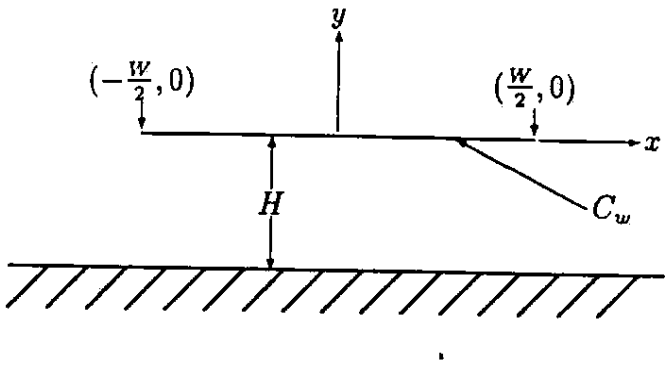

Figure 3.2. Geometry of the microstrip used in the Lewin/Vainshtein current integration method.

3.2 Microstrip current division

Assuming the geometry for the microstrip as in Figure 3.2, the magnetic vector potential $\overline{A}$ can be expressed by the integral [8]

$$\overline{A}(x,y) = \mu \oint_{C_W} G\overline{J}_{zo}\left(\overline{\rho}'\right) dl'. \tag{3.3}$$

An appropiate Green's function G for this microstrip configuration is

$$G(\overline{\rho},\overline{\rho}') = \frac{1}{2\pi} \ln\left[\frac{\sqrt{(x-x')^2+(y+2H)^2}}{\sqrt{(x-x')^2+y^2}}\right], \tag{3.4}$$

where the denominator of the logarithmic function is due to the strip, and the numerator is due to its image below the approximately perfectly conducting ground plane. This is a transverse, quasistatic function, which can be used according to the quasi-TEM assumption. When this Green's function is used and only the longitudinal component of surface current, J_{zo}, is considered, the single vector potential component A_z is

$$A_z(x,y) = \frac{\mu}{2\pi} \oint_{C_W} J_{zo}(x') \ln\left[\frac{\sqrt{(x-x')^2+(y+2H)^2}}{\sqrt{(x-x')^2+y^2}}\right] dl'. \tag{3.5}$$

The transverse variation of the magnetic field $\overline{H}$ of a quasi-TEM mode in the quasi-static limit can be expressed in terms of the Lorentz potential as

[8]

$$\overline{H} = \frac{1}{\mu}\nabla_T \times \overline{A}, \tag{3.6}$$

where the subscript T indicates transverse variation only, or $\frac{\partial}{\partial z} = 0$. Using (3.6) with $\overline{A} = A_z\overline{a}_z$, the magnetic field in Cartesian coordinates is

$$\overline{H}(x,y) = \overline{a}_x\frac{1}{\mu}\frac{\partial A_z}{\partial y} - \overline{a}_y\frac{1}{\mu}\frac{\partial A_z}{\partial x}. \tag{3.7}$$

This expression for the magnetic field can be used to find the surface currents on both sides of the infinitely thin strip by the boundary condition

$$\overline{J}_{so} = \overline{a}_n \times \overline{H}\,|_S. \tag{3.8}$$

Here $\overline{a}_n$ is the outward unit normal vector from the surface S, which is the surface of the strip in Figure 3.2. On the top of the strip, $\overline{a}_n = \overline{a}_y$, y approaches zero from the positive direction ($y = 0^+$), and

$$\overline{a}_z J_{zo,top}(x) = \overline{a}_y \times \overline{a}_x\left[-H_x(x,y)\,|_{y=0^+}\right], \tag{3.9}$$

so

$$J_{zo,top}(x) = -H_x(x,0^+). \tag{3.10}$$

Thus only the x-component of the magnetic field needs to be considered. Likewise, on the bottom of the strip, $\overline{a}_n = -\overline{a}_y$, y approaches zero from the negative direction ($y = 0^-$),

$$\overline{a}_z J_{zo,bot}(x) = -\overline{a}_y \times \overline{a}_x\left[H_x(x,y)\,|_{y=0^-}\right], \tag{3.11}$$

so

$$J_{zo,bot}(x) = H_x(x,0^-). \tag{3.12}$$

Solving for H_x from (3.5) and (3.7),

$$H_x(x,y) = \frac{\partial}{\partial y}\left[\frac{1}{2\pi}\oint_{C_W} J_{zo}(x')\ln\left(\frac{\sqrt{(x-x')^2+(y+2H)^2}}{\sqrt{(x-x')^2+y^2}}\right)dl'\right] \quad (3.13)$$

$$= \frac{1}{4\pi}\oint_{C_W} J_{zo}(x')\left[\frac{2(y+2H)}{(x-x')^2+(y-2H)^2} - \frac{2y}{(x-x')^2+y^2}\right]dl'$$

Since $J_{zo} = J_{zo,top} + J_{zo,bot}$, the current on each side of the strip can be subdivided as

$$J_{zo,top}(x) = \frac{1}{2}J_{zo}(x) - \delta J_{zo}(x) \quad (3.14)$$

and

$$J_{zo,bot}(x) = \frac{1}{2}J_{zo}(x) + \delta J_{zo}(x), \quad (3.15)$$

where

$$\delta J_{zo}(x) = \frac{1}{2}(J_{zo,bot}(x) - J_{zo,top}(x)) = \frac{1}{2}(H_x(x,0^-) + H_x(x,0^+)) \quad (3.16)$$

is a nonsingular difference term which approaches zero near the edges. If (3.13) is rewritten by the change of variable $-y \to y$ as

$$H_x(x,-y) = \oint_{C_W} \frac{J_{zo}(x')}{4\pi}\left[\frac{2(-y+2H)}{(x-x')^2+(-y-2H)^2} - \frac{-2y}{(x-x')^2+(-y)^2}\right]dl', \quad (3.17)$$

then the sum of (3.13) and (3.17) is

$$H_x(x,-y) + H_x(x,y) = \frac{1}{4\pi}\oint_{C_W} J_{zo}(x')[\frac{2(y+2H)}{(x-x')^2+(y-2H)^2} \quad (3.18)$$

$$+ \frac{2(-y+2H)}{(x-x')^2+(-y-2H)^2}]dl'.$$

In the limit as y approaches zero from the positive direction, or $y \to 0^+$ and $-y \to 0^-$, half the sum (3.18) becomes δJ_{zo} from (3.16), and since J_{zo} is the total current of both sides of the strip, the contour integral for δJ_{zo} becomes the line integral

$$\delta J_{zo}(x) = \frac{H}{\pi}\int_{-W/2}^{W/2} \frac{J_{zo}(x')dx'}{(x-x')^2+4H^2}. \quad (3.19)$$

In terms of J_{zo} and δJ_{zo}, the integral (3.2) is then

$$\begin{aligned} \alpha_c &= \frac{R_s}{2Z_o I^2} \int_{-\frac{W}{2}+\Delta_l}^{\frac{W}{2}-\Delta_r} \left[\frac{1}{2} J_{zo}^2(x) + 2\delta J_{zo}^2(x)\right] dx \\ &\approx \frac{R_s}{2Z_o I^2} \left[\int_{-\frac{W}{2}+\Delta_l}^{\frac{W}{2}-\Delta_r} \frac{1}{2} J_{zo}^2(x) dx + \int_{-\frac{W}{2}}^{\frac{W}{2}} 2\delta J_{zo}^2(x)\right] dx. \end{aligned} \tag{3.20}$$

The approximation is possible since $\delta J_{zo} \approx 0$ near the edges. The integration (3.20) can now be done with an expression for the total current $J_{zo}(x)$ on an infinitely thin strip in a microstrip system.

In the most general case of two similar strips, having the same widths but different edge shapes, the unperturbed current distribution $J_{zo}(x)$ will be the same for both. However, due to the different edge shapes, the losses are

$$\begin{aligned} \alpha_{cn} &= \frac{R_s}{2Z_o I^2} \int_{-\frac{W}{2}+\Delta_{nl}}^{\frac{W}{2}-\Delta_{nr}} \left[J_{zo,top}^2(x) + J_{zo,bot}^2(x)\right] dx \\ &= \frac{R_s}{2Z_o I^2} \int_{-\frac{W}{2}+\Delta_{nl}}^{\frac{W}{2}-\Delta_{nr}} \left[\frac{1}{2} J_{zo}^2(x) + 2\delta J_{zo}^2(x)\right] dx \end{aligned} \tag{3.21}$$

where $n = 1$ and $n = 2$ for the first and second strip, respectively. The difference in attenuation constants becomes

$$\begin{aligned} \alpha_{c2} - \alpha_{c1} &= \frac{R_s}{2Z_o I^2} \Big(\int_{-\frac{W}{2}+\Delta_{2l}}^{-\frac{W}{2}+\Delta_{1l}} [J_{zo,top}^2(x) + J_{zo,bot}^2(x)] dx - \\ &\quad \int_{\frac{W}{2}-\Delta_{1r}}^{\frac{W}{2}-\Delta_{2r}} [J_{zo,top}^2(x) + J_{zo,bot}^2(x)] dx \Big) \\ &= \frac{R_s}{2Z_o I^2} \Big(\int_{-\frac{W}{2}+\Delta_{2l}}^{-\frac{W}{2}+\Delta_{1l}} \left[\frac{1}{2} J_{zo}^2(x) + 2\delta J_{zo}^2(x)\right] dx - \\ &\quad \int_{\frac{W}{2}-\Delta_{1r}}^{\frac{W}{2}-\Delta_{2r}} \left[\frac{1}{2} J_{zo}^2(x) + 2\delta J_{zo}^2(x)\right] dx \Big) \end{aligned} \tag{3.22}$$

The δJ_{zo} terms can be ignored since they are very small in the range of integration, and this will simplify the calculation significantly. (3.22) is the result used to employ the Lewin/Vainshtein current integration technique on the loss effect of different edge shapes.

3.3 Microstrip current profiles

Various formulas for the total longitudinal current distribution of an infinitely thin microstrip can be used in the calculations above. Of course, all have the characteristic that they must integrate to the total current I, or

$$I = \int_{-W/2}^{W/2} J_{zo}(x)dx \tag{3.23}$$

According to the Meixner condition ([3],[4]), these currents should display a $r^{-1/2}$ dependence approaching the edge, where r is distance from the edge.

The simplest of all J_{zo} current profiles is given by the magnetic wall model, which assumes that the total strip current $J_{zo}(x)$ is constant over the strip width, or

$$J_{zo,MW}(x) = \frac{I}{W}. \tag{3.24}$$

Such a distribution would be obtained if a fictitious magnetic wall, the dual of a perfect conductor, were placed from the edges of the strip down to the ground plane. This would eliminate all fringing fields and result in a uniform field (and current) between the bottom of the strip and the ground plane. From Appendix 1, the final form of (3.20) is

$$\alpha_{MW} = \frac{R_s}{2Z_o W^2}(W - 2\Delta), \tag{3.25}$$

assuming identical edge shapes on the left and right edges of the strip. If the magnetic model includes the ground plane, which would also have the current distribution of (3.24), the attenuation constant would double. To be consistent, however, the quantity (3.25) will be retained.

A second current distribution is the Maxwell's current distribution for an isolated strip [9]. This neglects the effect of the ground plane, and the

curve remains the same for all aspect ratios of microstrip width over substrate height (W/H). This distribution is given by

$$J_{zo,MX}(x) = \frac{2}{\pi W\sqrt{1-(2x/W)^2}} = \frac{1}{\pi\sqrt{A^2-x^2}}, \tag{3.26}$$

where $A = W/2$ and $I = 1$. From Appendix 1, the J_{zo}^2 term of (3.20) becomes

$$\int_{-\frac{W}{2}+\Delta}^{\frac{W}{2}-\Delta} J_{zo}^2(x)dx = \frac{2}{\pi^2 W}\ln\left(\frac{W-\Delta}{\Delta}\right), \tag{3.27}$$

while the δJ_{zo}^2 term must be numerically integrated.

Another distribution is the current distribution obtained by Kuester and Chang [12], which is given by

$$J_{zo,KC}(x) = \frac{\pi C_p V}{8Hk'K(k)}\left[\cosh^2\left(\frac{\pi W}{8H}\right) - \cosh^2\left(\frac{\pi x}{4H}\right)\right]^{-1/2}, \tag{3.28}$$

where $C_pV = I$ is the total charge, $K(k)$ is the complete elliptic integral of the first kind, $k = \tanh\left(\frac{\pi W}{8H}\right)$, and $k' = \sqrt{1-k^2}$. This result was obtained by Green's function technique, using the two dimensional Green's function (3.4) containing the image term below the ground plane, and setting $y = 0$ to find the charge (current) density for a given potential difference V. From Appendix 1, the J_{zo}^2 term of (3.20) becomes

$$\begin{aligned}\frac{1}{I^2}\int_{-\frac{W}{2}+\Delta}^{\frac{W}{2}-\Delta} J_{zo}^2(x)dx &= \frac{\pi/8H}{k'^2K^2(k)\sqrt{\varrho(\varrho-1)}}\tanh^{-1}\left[\frac{\tanh\left((A-\Delta)\frac{\pi}{4H}\right)}{\sqrt{1-\frac{1}{\varrho}}}\right], \\ &= \frac{\pi}{8HK^2(k)\,\tanh\left(\frac{\pi W}{8H}\right)}\tanh^{-1}\left[\frac{\tanh\left((A-\Delta)\frac{\pi}{4H}\right)}{\tanh\left(\frac{\pi W}{8H}\right)}\right],\end{aligned} \tag{3.29}$$

where $\varrho = \cosh^2\left(\frac{\pi W}{8H}\right)$, and simplification has been done using $\cosh^2(x) - \sinh^2(x) = 1$.

A normalized closed form expression by Kobayashi [9] is

$$\frac{J_{zo,K}(x)}{J_{zo,K}(0)} = 1 + 10\left(1 - \frac{2x_c}{W}\right)\frac{M(x)-1}{M(x_c)-1}, \tag{3.30}$$

where

$$M(x) = \frac{1}{\sqrt{1-(2x/W)^2}} \tag{3.31}$$

and x_c, given by Kobayashi, is a function of the microstrip geometry w/h. Similar to Kuester and Chang, Kobayashi's result was obtained by a Green's function technique, but the parameter x_c is used to vary the closed form expression according to the aspect ratio. Using Kobayashi's current profile, once again the integral (3.20) can be reduced to closed form (see Appendix 1) except for the δJ_{zo}^2 term, which must be approximated numerically. The J_{zo}^2 term is

$$\begin{aligned}\int_{-\frac{W}{2}+\Delta}^{\frac{W}{2}-\Delta} J_{zo}^2(x)dx &= 2(1-\kappa)^2(A-\Delta) \\ &+ 4A(1-\kappa)\kappa\sin^{-1}\left(1-\frac{\Delta}{A}\right) + A\kappa^2\ln\left(\frac{W-\Delta}{\Delta}\right).\end{aligned} \tag{3.32}$$

The current I, found in Appendix 1 to be

$$I = (1-\kappa)W + \frac{\pi\kappa W}{2}, \quad \kappa = \frac{10\left(1-\frac{x_c}{A}\right)\sqrt{A^2-x_c^2}}{A-\sqrt{A^2-x_c^2}}, \tag{3.33}$$

is also normalized, but in the ratio J_{zo}^2/I^2, the normalizations cancel. This will be considered the most accurate current profile, and will be used in all subsequent calculations.

In Figure 3.3, a plot of the attenuation constants using the given current profiles is shown for a wide range of aspect ratios. The results are shown in percentage difference from the Kobayashi result, or

$$\% = \frac{\alpha_{other} - \alpha_K}{\alpha_K} \times 100\%, \tag{3.34}$$

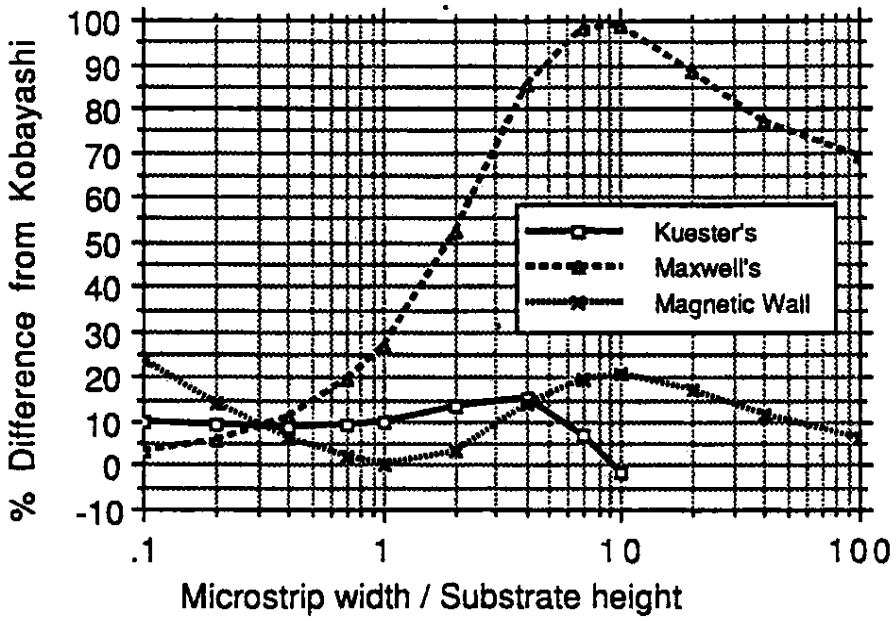

Figure 3.3. Attenuation constants for a variety of strip current profiles J_{zo}, shown in difference from the Kobayashi result.

since Kobayashi's profile is taken for J_{zo} in this thesis. As can be seen from the graph, Kuester's current profile is relatively close to Kobayashi's, as is the magnetic wall model over much of the range, which is surprising. If the ground plane is included in the magnetic wall model losses, the result would have been higher by at least 100%. Maxwell's distribution yields significantly higher loss results, especially for wider strips.

3.4 Numerical results and comparisons

3.4.1 A survey of microstrip conductor loss methods based on the surface impedance condition Various methods may be used to find α_c, such as numerical computation, accurate experiment, or analytical approximations. A comparison of those theoretical methods based on the

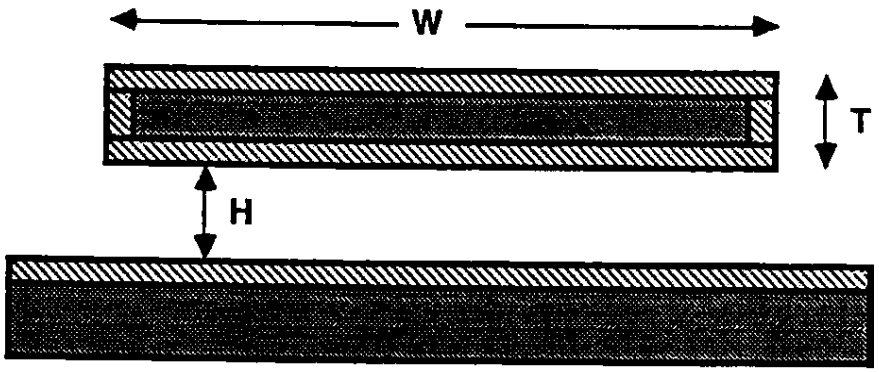

Figure 3.4. Geometry of the incremental inductance rule. The lightly shaded regions are the half skin depth recessions in the metallic walls.

surface impedance boundary condition is done here for a rectangular-edged microstrip. Among those are the Lewin/Vainshtein current integration method of this chapter, using the integration stopping point of $\Delta_{rect} = \frac{T}{290.8}$; approximate analytical loss formulas of Pucel [1], Schneider [19], and Kaden [20]; and numerical results given by Spielman [21] and Wiesbeck [22]. All assume rectangular-edged strips.

Pucel's commonly accepted results are based on Wheeler's incremental inductance rule [5], which is derived from the surface impedance condition, and on approximate closed form expressions for the inductance of nonzero-thickness, rectangular-edged microstrips. The surface impedance $Z_s = R_s + iX_s$ has equal real and imaginary parts, and $X_s = \omega L_i$, where L_i, the internal inductance, is much smaller than the external inductance. The internal inductance can be obtained by finding the increase in the inductance when all metallic boundaries are recessed by half of a skin depth $\delta/2$ (see Figure 3.4). This leads to a result for the total resistance R, power lost $= I^2R$, and eventually the attenuation constant from $\alpha_c = RI^2/(2Z_oI^2)$. The formulas in Pucel's paper

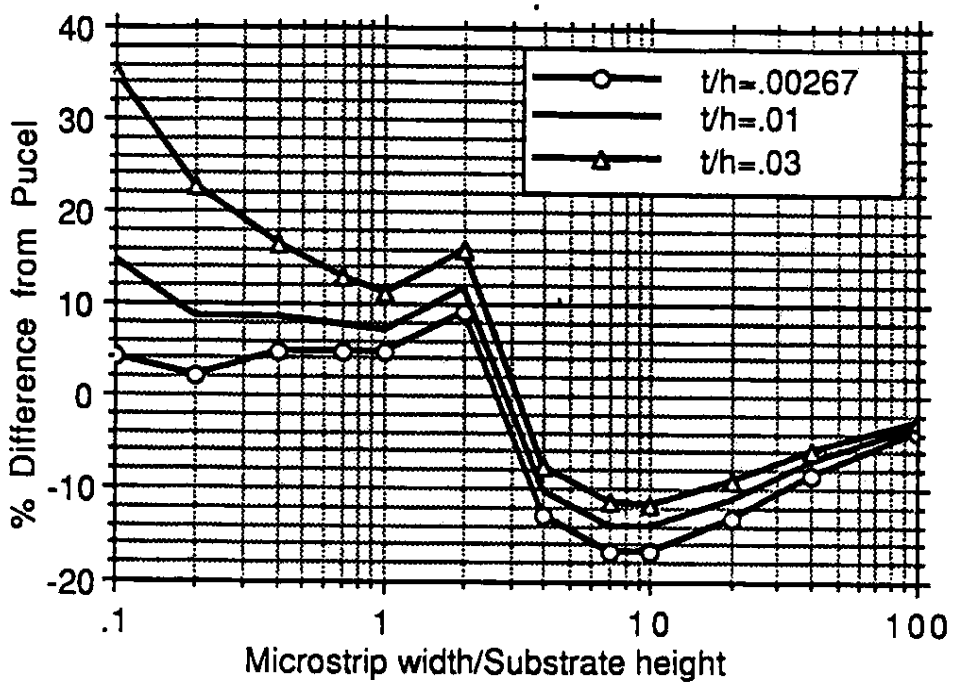

Figure 3.5. A comparison between the Lewin/Vainshtein current integration method and Pucel's formulas for the attenuation coefficient, shown in % difference from Pucel.

include ground plane loss but can be altered to consider only the strip conductor by not receding the ground plane wall. Figure 3.5 thoroughly compares the altered Pucel's results with those obtained by the current integration method for a wide range of normalized widths ($\frac{W}{H}$) and thicknesses ($\frac{T}{H}$). All data is given in the form of a percentage difference from Pucel

$$\% = \frac{\alpha_{c,Lewin} - \alpha_{c,Pucel}}{\alpha_{c,Pucel}} \times 100\%. \tag{3.35}$$

Generally, the Lewin/Vainshtein current integration method predicted higher strip loss than Pucel for narrow strips and lower strip loss for wider strips.

The method of Schneider [19] is similar to Pucel's in that it also is

based on Wheeler's rule, and the ground plane loss contribution can be extracted. However, Schneider's formulas use different closed formed results, in this case approximations for the microstrip characteristic impedance. Kaden [20] uses the conformal transformation technique on thin microstrips, and derives loss formulas for both the ground plane and the strip from approximations of the resulting hyperelliptic integrals. A program for moment method solution of a general microstrip configuration with ground plane loss is given in Spielman [21] (errors exist in the program listing in [21], and were corrected by H. George Oltman of Tecom Industries in a private communication). Another numerical method by Wiesbeck [22] implementing the moment method is used to give results with and without ground plane loss for three specific microstrip substrate heights.

All of the other techniques were compared for one of the specific microstrip configurations used by Wiesbeck. Computation with these methods was done over a range of strip width from $0.1 < W < 1.8\ mm$, while all other parameters were held constant at $H = 0.254\ mm$, $T = 18.19\ \mu m$, $\epsilon_r = 1$, $\sigma = 4.9 \times 10^{-7} \frac{\mho}{m}$, and $f = 1\ GHz$. Results of the total conductor loss including the ground plane are given in Table 3.1 for the methods of Pucel, Schneider, Kaden, Spielman, and Wiesbeck. Table 3.2 compares strip loss only for Pucel, Schneider, Kaden, Wiesbeck, and Lewin/Vainshtein. Once again, all entries are given in the form of a percentage difference from Pucel.

Several observations can be made from the results. First, as the width gets narrower to $0.1\ mm$, the thin strip approximation upon which each of the analytical formulas is founded starts to fail. This results in larger differences from Pucel, one of those analytical methods, at that width. Second, there is a

Table 3.1. Percent difference in four different methods for total conductor losses in microstrip (including ground plane) from the Pucel formulas. $H = 0.254\ mm$, $T = 18.19\ \mu m$, $\epsilon_r = 1$, $\sigma = 4.9 \times 10^{-7} \frac{\mho}{m}$, and $f = 1\ GHz$.

Width (mm)	Loss calculation method			
	Schneider	....Kaden	.Spielman	.Wiesbeck
0.1	22.0	-29.5	-0.9	14.3
0.2	10.9	-20.0	-3.3	9.0
0.2540	9.1	-16.9	-3.0	11.5
0.2541	18.2	-16.9	-3.0	11.5
0.3	10.5	-14.9	-2.5	8.9
0.4	7.7	-9.1	1.6	11.2
0.5	15.2	-0.5	9.5	18.7
0.5080	16.2	0.4	10.6	19.6
0.5081	4.0	-10.2	1.0	7.0
0.6	3.8	-9.9	-1.6	6.3
0.8	3.9	-9.1	-1.3	4.2
1.0	3.3	-8.4	-1.2	2.3
1.2	2.5	-7.7	-0.5	1.4
1.4	1.7	-7.2	-0.1	0.4
1.6	1.2	-6.6	0.1	0.2
1.8	0.9	-6.0	0.3	0.3

sharp discontinuity in Pucel's loss at $\frac{W}{H} = 2$, or $W = 0.508\ mm$. This is where the two closed formed inductance approximations used by Pucel meet, resulting in a discontinuity of 9.0% for $T \rightarrow 0$ and slightly worse for the nonzero thickness here. Judging from the comparisons, it appears that the $\frac{W}{H} < 2$ approximation is at fault, giving losses which are relatively too low. A similar discontinuity appears for Schneider at the junction of two closed form approximations of characteristic impedance, $\frac{W}{H} = 1$ or $W = 0.254\ mm$. The third analytical result, by Kaden, appears to be consistently lower than other results, but improves as the strip width becomes wide. Spielman's numerical code shows excellent agreement with Pucel, but the issue of discretization error should be mentioned. In this application, the finite substrate and ground plane

Table 3.2. Percent difference in four different methods for strip conductor loss in microstrip from the Pucel formulas. $H = 0.254\ mm$, $T = 18.19\ \mu m$, $\epsilon_r = 1$, $\sigma = 4.9 \times 10^{-7} \frac{\mho}{m}$, and $f = 1\ GHz$.

Width (mm)	Loss calculation method			
	Schneider	....Kaden	....Lewin	.Wiesbeck
0.1	23.7	-41.5	29.4	20.4
0.2	12.0	-32.7	19.3	19.3
0.2540	10.2	-29.7	17.5	23.6
0.2541	19.3	-29.7	17.7	23.7
0.3	11.5	-27.5	15.6	22.0
0.4	8.5	-22.0	15.0	26.4
0.5	16.1	-13.9	20.6	36.7
0.5080	17.0	-13.2	21.6	37.7
0.5081	4.6	-22.4	8.6	23.1
0.6	4.5	-21.4	3.7	23.4
0.8	4.3	-19.8	-2.4	21.9
1.0	3.6	-18.3	-4.7	20.1
1.2	2.8	-17.0	-6.0	19.1
1.4	2.0	-15.8	-7.2	17.4
1.6	1.4	-14.6	-8.2	16.6
1.8	1.0	-13.7	-8.6	15.6

width was assigned a value of $L = 10W$. When this ratio was changed, conductor loss was altered significantly, especially for very large $\frac{L}{W}$ ratios. Thus, discretization in numerical methods can drastically alter results. Wiesbeck also compared reasonably with Pucel in *total* loss, particularly for wider strips, but the contribution of *strip* loss varied much differently with substrate height H than Pucel.

3.4.2 Ground plane loss contribution The contribution of the ground plane conductor loss to the total conductor loss has been quantified by the alteration of Pucel's formulas mentioned previously. These changes are listed in Appendix 2. Intuitively, microstrips with a very narrow strip ($\frac{W}{H} < 1$) should have very high current concentration, and hence dominant loss, in the

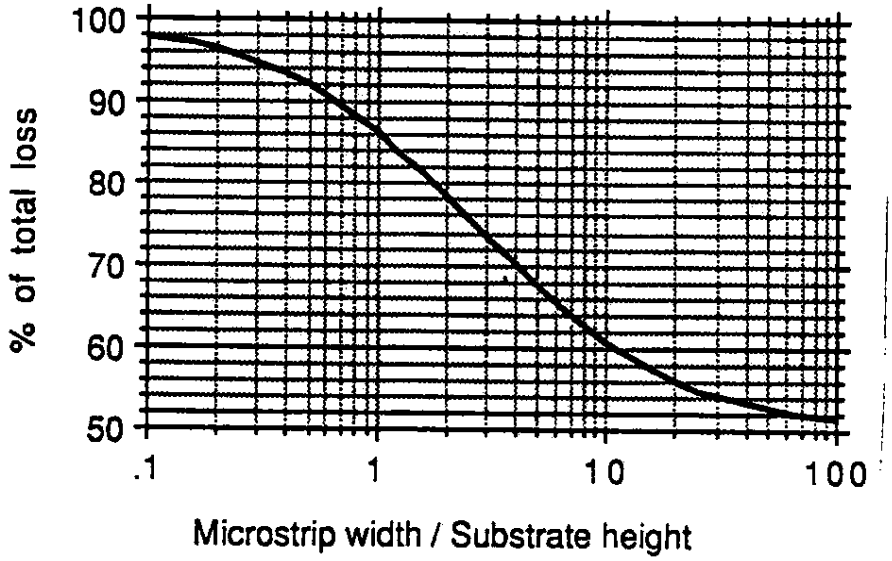

Figure 3.6. Strip percentage of the total loss in a microstrip system as a function of $\frac{W}{H}$. Obtained by an alteration of Pucel's formulas for attenuation constant.

strip. As the strip becomes wider, the current concentration becomes more spread out. In the limit of a very wide strip, it will almost approximate the magnetic wall model, for which the loss is equally divided between the strip and the ground plane. This is indeed true, as seen from the results of Figure 3.6. For practical microstrip, strip loss definitely dominates, although ground plane loss may be significant enough to calculate for a higher degree of accuracy.

3.4.3 Effect of edge shape on loss The effect of edge shape on loss has been investigated by using the various edge stopping points from Table 2.2 with equation (3.20) and Kobayashi's current profile. The results are given for a wide range of widths and thicknesses in Figure 3.7 in the form of percentage difference from the Lewin/Vainshtein prediction for a rectangular edge.

As the edge corner gets sharper, the loss increases, as predicted in Chapter 2. For the sharper edges, the predicted increase in loss seems to be quite high, especially for narrower width strips. Although the tendency of increasing loss with increasing sharpness is probable, the actual increase may be too large, due to the possible breakdown of some assumptions. First, the surface impedance condition is based on a smooth interface between metal and dielectric. The sharp edges might require a modification of the Leontovich condition. Also, in the calculation of integration stopping distances Δ, the fields on a perfectly conducting strip are used. The actual current approached a finite value instead of blowing up with a singularity depending on the edge corner angle. These effects will be discussed in Chapter 5.

When the thickness of the strip becomes larger compared to the width, the increase in loss due to edge shape rises dramatically, as seen from the graph. This is not attributed to an invalid Δ, since the stopping point does not increase much in the thick strip limit, but besides the factors already mentioned, the result can be explained by the inaccuracy of the infinitely thin perturbation. However, for practical microstrip configurations, where the strip thickness is very small compared to the width, the assumption is valid, and the effect of edge shape is seen to be important. The results here compare favorably with a quasi-static moment method study by Chryssomallis *et. al.*[23], who found that for the specific case of $W/H = 0.101$ and $T/H = 0.011$, the microstrip with a circular-edged strip will have 15% less conductor loss than the microstrip with rectangular edges. For the same configuration, the present technique predicts a 10.7% decrease in loss for a circular cross section.

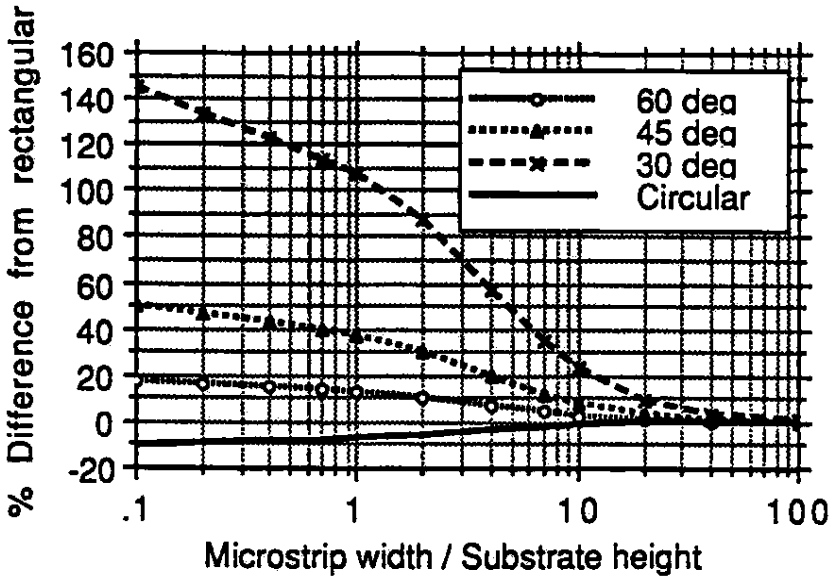

Figure 3.7. Differences in attenuation constant for various edge shapes, shown in difference from a rectangular-edged strip. Obtained by the Lewin/Vainshtein current integration method.

CHAPTER 4

INCREMENTAL WIDTH METHOD

4.1 Introduction

In some quasi-TEM transmission line configurations similar to microstrip, where a relatively small strip conductor forms the major component of loss, expressions for the infinitely thin strip current distribution J_{zo} are not available yet. As discovered in the previous chapter, the use of Maxwell's current distribution for an isolated strip is not acceptable, since the other conductor surfaces change the current distribution enough to significantly affect loss. As a result, the Lewin/Vainshtein current integration method can not be used to calculate loss or the effect of various strip edge shapes. For that reason, a method has been developed to find the edge shape effect on conductor loss from only the strip width inductance derivative $\partial L/\partial W$ and other quasi-TEM transmission line parameters. Once a value for the loss with a certain strip edge shape (usually rectangular) is obtained by other means, the loss of a similar strip differing only in edge shape can be obtained from an expression for the inductance of the corresponding infinitely thin strip. This inductance is significantly easier to obtain than the inductance which includes strip thickness. All of the assumptions used in the previous chapters continue to apply here.

The technique, termed the incremental width method, is developed in this chapter by a perturbational method. The results will be applied to both the microstrip and open coplanar waveguide configurations, and comparison to

results from the Lewin/Vainshtein current integration method will be done for microstrip.

4.2 Development of the incremental width method

4.2.1 Loss difference formula from a current model The total current distribution J_{zo} of the strip near the left edge can be modelled as [9]

$$J_{zo}(x_l) = \frac{K_l I}{\sqrt{x_l}} + F_l(x_l) \quad . \tag{4.1}$$

as $x_l \to 0$, where K_l is a constant, $F_l(x_l)$ is a function of x_l which is bounded as $x_l \to 0$, and x_l is distance from the left edge (see Figure 3.1). Similarly, J_{zo} near the right edge is

$$J_{zo}(x_r) = \frac{K_r I}{\sqrt{x_r}} + F_r(x_r) \tag{4.2}$$

as $x_r \to 0$, where K_r, $F_r(x_r)$, and x_r are analogously defined. Since the stopping points Δ are in general very near the edge, $J_{zo,top}$ and $J_{zo,bot}$ can each be approximated as $\frac{1}{2}J_{zo}$ there, that is, $\frac{K_l I}{2\sqrt{x_l}}$ or $\frac{K_r I}{2\sqrt{x_r}}$. Since $x_l = x + \frac{W}{2}$ and $x_r = \frac{W}{2} - x$ from the geometry of Figure 3.1, (3.22) becomes

$$\begin{aligned} \alpha_{c2} - \alpha_{c1} &= \frac{R_s}{2Z_o I^2}\left[\int_{\Delta_{2l}}^{\Delta_{1l}} \frac{2K_l^2 I^2}{4x_l} dx_l - \int_{\Delta_{1r}}^{\Delta_{2r}} \frac{2K_r^2 I^2}{4x_r} dx_r\right] \\ &= \frac{R_s}{4Z_o}\left[K_l^2 \ln\left(\frac{\Delta_{1l}}{\Delta_{2l}}\right) + K_r^2 \ln\left(\frac{\Delta_{1r}}{\Delta_{2r}}\right)\right]. \end{aligned} \tag{4.3}$$

The constants K_l and K_r, the singularity terms in the current models $J_{zo} = \frac{K_l I}{\sqrt{x_l}}$ and $J_{zo} = \frac{K_r I}{\sqrt{x_r}}$, must be determined. Of course, when J_{zo} is integrated over the entire strip, the result is the current I, but the K terms are different for each geometry and configuration. In the following, K will be related to the inductance of the zero-thickness case, so that a modified incremental inductance rule, called the incremental width method, will be developed

without thickness corrections. Eventually, the separate terms K_l and K_r will combine into the derivative of inductance with respect to width, $\frac{\partial L}{\partial W}$, so the subscripts will be dropped for brevity.

4.2.2 Relating the singular part of the current with the expanded vector potential From (3.6), the quasi-static magnetic field can be expressed as

$$\overline{H} = \frac{1}{\mu}\nabla_T \times \overline{A}, \tag{4.4}$$

where the potential $\overline{A}$ satisfies

$$\nabla_T^2 A_z = 0, \tag{4.5}$$

in the source-free cross-sectional region surrounding the strip as in Figure 4.1a. If A_z is expanded in a sine series near the edge $x = -\frac{W}{2}$ ($\rho = 0$ in Figure 4.1a), the potential becomes

$$A_z(\rho, \phi) = A_{zo} + \sum_{m=1}^{\infty} A_{zm}(\rho) \sin\left(\frac{m\phi}{2}\right), \tag{4.6}$$

where A_{zo} is the arbitrary constant value of the potential on the strip (at angles of $\phi = 0$ and 2π). In this two-dimensional, source-free environment around the edge, the scalar Laplace equation (4.5) becomes, upon substituting (4.6),

$$\left(\frac{1}{\rho}\frac{\partial}{\partial\rho}\rho\frac{\partial}{\partial\rho} - \frac{(m/2)^2}{\rho^2}\right) A_{zm}(\rho) = 0, \tag{4.7}$$

which is solved by

$$A_{zm}(\rho) = \xi_m \rho^{\frac{m}{2}}, \tag{4.8}$$

where ξ_m is an amplitude constant. The other solution $\rho^{-m/2}$ is disallowed due to the Meixner edge condition of finite field energy in any finite volume [24]. From (4.8), (4.6) becomes

$$A_z(\rho, \phi) = A_{zo} + \sum_{m=1}^{\infty} \xi_m \rho^{\frac{m}{2}} \sin\left(\frac{m\phi}{2}\right). \tag{4.9}$$

The transverse magnetic field components H_ϕ and H_ρ are found from (3.6), using only A_z. In terms of the expanded potential A_z,

$$H_\phi(\rho,\phi) = -\frac{1}{\mu}\frac{\partial A_z}{\partial \rho} = -\frac{1}{\mu}\sum_{m=1}^{\infty}\frac{m}{2}\xi_m \rho^{\frac{m}{2}-1}\sin\left(\frac{m\phi}{2}\right) \tag{4.10}$$

and

$$H_\rho(\rho,\phi) = \frac{1}{\mu\rho}\frac{\partial A_z}{\partial \phi} = \frac{1}{\mu}\sum_{m=1}^{\infty}\frac{m}{2}\xi_m \rho^{\frac{m}{2}-1}\cos\left(\frac{m\phi}{2}\right). \tag{4.11}$$

From the magnetic field, the surface current on both sides of the infinitely thin strip can be found from the boundary condition (3.8). On the top surface, the outward unit normal vector $\overline{a}_n = \overline{a}_\phi = \overline{a}_y$, $\overline{a}_\rho = \overline{a}_x$, and $\phi = 0$, so

$$\overline{J}_{zo,top}(\rho) = \overline{a}_y \times (H_\rho \overline{a}_x + H_\phi \overline{a}_y)\mid_{\phi=0} = -\overline{a}_z H_\rho \mid_{\phi=0} = -\frac{1}{\mu}\sum_{m=1}^{\infty}\frac{m}{2}\xi_m \rho^{\frac{m}{2}-1}\overline{a}_z. \tag{4.12}$$

On the bottom surface, $\overline{a}_n = -\overline{a}_\phi = -\overline{a}_y$, $\overline{a}_\rho = \overline{a}_x$, and $\phi = 2\pi$, so

$$\begin{aligned}\overline{J}_{zo,bot}(\rho) &= -\overline{a}_y \times (H_\rho \overline{a}_x + H_\phi \overline{a}_y)\mid_{\phi=2\pi} = \overline{a}_z H_\rho \mid_{\phi=2\pi} \\ &= \frac{1}{\mu}\sum_{m=1}^{\infty}\frac{m}{2}\xi_m \rho^{\frac{m}{2}-1}\cos(m\pi)\overline{a}_z.\end{aligned} \tag{4.13}$$

Thus, the total surface current is

$$J_{zo}(\rho) = -\frac{1}{\mu}\sum_{m=1}^{\infty}\frac{m}{2}\xi_m \rho^{\frac{m}{2}-1}(1-\cos(m\pi)) = -\frac{\xi_1}{\mu}\rho^{-\frac{1}{2}} - \frac{3\xi_3}{\mu}\rho^{\frac{3}{2}} + \cdots. \tag{4.14}$$

Since on the strip surface $\rho = x_l$, (4.14) can be compared with the current expression from (4.1) to find that

$$KI = -\frac{\xi_1}{\mu}, \tag{4.15}$$

where the l subscripts have been omitted from K and ξ_1. A similar derivation using the vector potential expansion about the right edge yields

$$K_r I = \frac{\xi_{r1}}{\mu}. \tag{4.16}$$

The relation (4.15) will be compared with another derivation based on inductances in order to eliminate ξ_1 and determine K in terms of an incremental inductance.

4.2.3 Relating the singular part of the current with the inductance derivative Figure 4.1 illustrates two cases of an infinitely thin strip surrounded by a perfectly conducting surface, both invariant in the z-direction. The first case has associated with it the vector potential A_z, magnetic field $\overline{H}$, width W, and a cylindrical geometry (ρ, ϕ) with origin at the left strip edge. The second, perturbed, case has an extra length δW to the left of the first edge, so its width is $W + \delta W$. It has a different cylindrical geometry (r, θ) centered at the new left edge, as well as quantities $A_{z\delta}$ and $\overline{H}_\delta$. In the first, the vector potential expansion near the edge is (4.9), and in the perturbed case, it is

$$A_{z\delta}(r,\theta) = A_{zo\delta} + \sum_{m=1}^{\infty} \xi_{m\delta} r^{\frac{m}{2}} \sin\left(\frac{m\theta}{2}\right). \tag{4.17}$$

The first term, $A_{zo\delta}$, the arbitrary constant potential of the strip, is set equal to A_{zo}, the potential of the first strip. The outer perfect conductors in each case are assigned potentials of $A_z = 0$.

Starting with the integral

$$\int_S \overline{B}_\delta \cdot \overline{H} dS, \tag{4.18}$$

where S is the enclosed area in Figure 4.1a excluding the strip, and using the definition

$$\overline{B}_\delta = \nabla_T \times \overline{A}_\delta \tag{4.19}$$

along with the vector identity

$$(\nabla_T \times \overline{C}) \cdot \overline{D} = \nabla_T \cdot (\overline{C} \times \overline{D}) + \overline{C} \cdot (\nabla_T \times \overline{D}), \tag{4.20}$$

the integral becomes

$$\int_S \overline{B}_\delta \cdot \overline{H} dS = \int_S (\nabla_T \times \overline{A}_\delta) \cdot \overline{H} dS = \int_S [\nabla_T \cdot (\overline{A}_\delta \times \overline{H}) + \overline{A}_\delta \cdot (\nabla_T \times \overline{H})] dS. \quad (4.21)$$

The region S has no sources, so $\nabla_T \times \overline{H} = 0$ can be used to simplify the integral by eliminating the last term. Also, the divergence theorem

$$\int_S (\nabla_T \cdot \overline{F}_T) dS = \oint_C \overline{F}_T \cdot \overline{a}_n dl, \quad (4.22)$$

where $\overline{a}_n$ is the outward unit normal vector, is applied. In this case, the transverse vector $\overline{F}_T$ is $(\overline{A}_\delta \times \overline{H}) = (A_{zo\delta} \overline{a}_z \times \overline{H})$. Thus,

$$\int_S \overline{B}_\delta \cdot \overline{H} dS = \oint_C (\overline{A}_\delta \times \overline{H}) \cdot \overline{a}_n dl = \oint_{C_W + C_o} (A_{zo\delta} \overline{a}_z \times \overline{H}) \cdot \overline{a}_n dl, \quad (4.23)$$

where C_o is the outer conductor on which $A_z = 0$ and C_W is the closed loop around the strip in Figure 4.1a, on which the potential $A_{z\delta}$ is always the constant $A_{zo\delta}$. From the identity

$$\overline{A} \cdot (\overline{B} \times \overline{C}) = \overline{C} \cdot (\overline{A} \times \overline{B}) \quad (4.24)$$

and defining $\overline{a}_l$ as the unit vector tangential to the strip contour C_W such that $\overline{a}_n \times \overline{a}_z = \overline{a}_l$, the integral (4.23) reduces to

$$= \oint_{C_W} \overline{H} \cdot (\overline{a}_n \times A_{zo\delta} \overline{a}_z) dl = \oint_{C_W} \overline{H} \cdot (A_{zo\delta} \overline{a}_l) dl = \oint_{C_W} A_{zo\delta} \overline{H} \cdot d\overline{l} = A_{zo\delta} I \quad (4.25)$$

since the contour integral

$$\oint_C \overline{H} \cdot d\overline{l} = I \quad (4.26)$$

is defined as the conductor current I. From the definition of inductance, the strip potential A_{zo} can be expressed as $A_{zo} = LI$. Similarly, $A_{zo\delta} = L_\delta I_\delta$. Since the potential of the strips in both cases were set equal,

$$\int_S \overline{B}_\delta \cdot \overline{H} dS = A_{zo\delta} I = L_\delta I_\delta I = A_{zo} I = L I^2. \quad (4.27)$$

Now, if the permeability μ is linear throughout,

$$\int_S \overline{B}_\delta \cdot \overline{H} dS = \int_S \overline{B} \cdot \overline{H}_\delta dS \tag{4.28}$$

is true, and from a derivation similar to (4.18)-(4.24) before,

$$\int_S \overline{B} \cdot \overline{H}_\delta dS = \oint_{C_{W+\delta W}} A_z(\rho, \phi) \overline{H}_\delta \cdot d\bar{l}. \tag{4.29}$$

Previously, the magnetic field of the first case, $\overline{H}$, was integrated around the contour of the first width W. Now, $\overline{H}_\delta$ is being integrated over the perturbed width $W + \delta W$. The difference will arise because $A_{z\delta}$ was constant, $A_{zo\delta}$, over a larger region $W + \delta W$ than what the previous integration was carried over, specifically W. In the present integral, A_z is constant, A_{zo}, over width W only and has the behavior given by the expansion in (4.9) beyond that. If A_z is approximated by

$$A_z(\rho, \phi) \approx A_{zo} + \xi_1 \sqrt{\rho} \sin\left(\frac{\phi}{2}\right) \tag{4.30}$$

in the region $0 \leq r \leq \delta W$, $\theta = 0$, which is also $\delta W \geq \rho \geq 0$, $\phi = \pi$, and it is the constant A_{zo} over the remainder of the strip, then

$$\oint_{C_{W+\delta W}} A_z(\rho, \phi) \overline{H}_\delta \cdot d\bar{l} = \oint_{C_{W+\delta W}} A_{zo} \overline{H}_\delta \cdot d\bar{l} + 2 \int_0^{\delta W} \left[\xi_1 \sqrt{\rho} \sin\left(\frac{\phi}{2}\right)\right] \left[\overline{H}_\delta \cdot d\bar{\rho}\right]. \tag{4.31}$$

Here the factor of two arises from integration of the top and bottom of the extra length of strip δW. Recognizing the right-hand side contour integral as A_{zo} times the current I_δ, and substituting from a first term approximation for $H_{r\delta}$ analogous to (4.11),

$$\overline{H}_\delta = \bar{a}_r H_{r\delta}(r, \theta) \approx \frac{\xi_{1\delta}}{2\mu} r^{-\frac{1}{2}} \cos\left(\frac{\theta}{2}\right) \bar{a}_r, \tag{4.32}$$

and since $\bar{a}_r \cdot \bar{a}_\rho = -1$ on the extra length δW, the expression becomes

$$\oint_{C_{W+\delta W}} A_z(\rho, \phi) \overline{H}_\delta \cdot d\bar{l} \approx A_{zo} I_\delta + 2 \int_0^{\delta W} \left[\xi_1 \sqrt{\rho} \sin\left(\frac{\phi}{2}\right)\right] \left[\frac{-\xi_{1\delta}}{2\mu\sqrt{r}} \cos\left(\frac{\theta}{2}\right)\right] d\rho. \tag{4.33}$$

In the region of integration, $\phi = \pi$, $\theta = 0$, and $r = \delta W - \rho$, so [17]

$$= A_{zo}I_\delta + 2\int_0^{\delta W} \frac{\xi_1\xi_{1\delta}}{2\mu}\sqrt{\frac{\rho}{\delta W - \rho}}d\rho = A_{zo}I_\delta + \frac{-\xi_1\xi_{1\delta}}{\mu}\left(\frac{\pi\delta W}{2}\right). \tag{4.34}$$

From the definition $A_{zo} = LI$,

$$\int_S \overline{B}\cdot\overline{H}_\delta\, dS = LII_\delta + \frac{-\xi_1\xi_{1\delta}\pi\delta W}{2\mu}. \tag{4.35}$$

Equating the integrals (4.27) and (4.35) by (4.28),

$$LII_\delta + \frac{-\xi_1\xi_{1\delta}\pi\delta W}{2\mu} = L_\delta I_\delta I, \tag{4.36}$$

and rearranging, the result is

$$II_\delta(L_\delta - L) = \frac{-\xi_1\xi_{1\delta}\pi\delta W}{2\mu}. \tag{4.37}$$

Taking the limiting case $\delta W \to 0$, $I_\delta \to I$, $\xi_{1\delta} \to \xi_1$, and $\frac{L_\delta - L}{\delta W} \to \frac{\partial L}{\partial W}$, the constant ξ_1 in terms of the inductance derivative is then

$$\xi_1^2 = \frac{-2\mu I^2\frac{\partial L}{\partial W}}{\pi}. \tag{4.38}$$

Using (4.15) in (4.38), it is found that

$$K^2 = \frac{-2\frac{\partial L}{\partial W}}{\mu\pi}, \tag{4.39}$$

the desired expression of K in terms of an incremental inductance. When the right edge is incremented in a similar derivation, then, using (4.16), the identical result (4.39) is obtained. Therefore,

$$K_l^2 = K_r^2 = K^2 = \frac{-2\frac{\partial L}{\partial W}}{\mu\pi}. \tag{4.40}$$

Substituting back into (4.3), the final result for two general strips is

$$\alpha_{c2} - \alpha_{c1} = \frac{-R_s\frac{\partial L}{\partial W}}{2\mu\pi Z_o}\left[\ln\left(\frac{\Delta_{1l}}{\Delta_{2l}}\right) + \ln\left(\frac{\Delta_{1r}}{\Delta_{2r}}\right)\right]. \tag{4.41}$$

This amounts to a kind of incremental width method analogous to Wheeler's [5] for the change in α_c due to edge shape.

4.3 Results from the incremental width method

4.3.1 Microstrip lines Formula (4.41) has been applied to microstrip lines of varying geometries comparing losses from the rectangular, circular, and 45° trapezoidal edges using the conductor loss α_c of the rectangular-edged strip from the Lewin/Vainshtein current integration method. The microstrip inductance for an infinitely thin strip was taken from [1], with the thickness correction terms set equal to zero. Finally, the stopping points for those edges, $\Delta_{rect} = \frac{T}{290.8}$, $\Delta_{circ} = \frac{T}{124.77}$, and $\Delta_{45^\circ} = \frac{T}{20187.3}$, were taken from Table 2.2.

An approximate expression for the inductance of the microstrip [1] is

$$L = \frac{\mu_o}{2\pi}\left[\ln\left(\frac{8H}{W}\right) + \frac{1}{32}\left(\frac{W}{H}\right)\right]^2 + \cdots] \tag{4.42}$$

for $\frac{W}{H} \leq 2$, and

$$L = \frac{\mu_o}{2}\frac{W}{2H} + \frac{1}{\pi}\ln\left[2\pi e\left(\frac{W}{2H} + 0.94\right)\right]^{-1} \tag{4.43}$$

for $\frac{W}{H} \geq 2$. The required derivative $\frac{\partial L}{\partial W}$ is found to be

$$\frac{\partial L}{\partial W} = -\frac{\mu_o}{2\pi H}\left[\frac{H}{W} - \frac{W}{16H}\right] \tag{4.44}$$

for $\frac{W}{H} \leq 2$, and

$$\frac{\partial L}{\partial W} = -\frac{\mu_o}{2\pi H}\frac{2\pi + \frac{4}{W/H+1.88}}{(\frac{W}{H} + \frac{2}{\pi}\ln[2\pi e(\frac{W}{2H} + 0.94)])^2} \tag{4.45}$$

for $\frac{W}{H} \geq 2$.

In Figure 4.2 the results of the loss comparison over a large range of strip widths and thicknesses are given. The results are very close to those of the current integration method of Chapter 3. As the corner gets sharper, the

loss increases. Also, as expected, edge shape becomes unimportant for very wide strips, since less of the total current is concentrated in the edges of the strip. Again, in that extreme, ground plane loss grows significantly and can no longer be ignored. Another observation is that as the strip grows thicker, the dependence on edge shape increases as well.

4.3.2 Open coplanar waveguide Formula (4.41) has also been applied to the problem of open coplanar waveguides, shown in Figure 4.3, to investigate the theoretical increase in loss when trapezoidal edges are used instead of rectangular edges. From the expressions for characteristic impedance of that transmission line [7]

$$Z_o = \sqrt{\frac{l_s}{c_s}} = \frac{30\pi}{\sqrt{\epsilon_{re}}} \frac{K(k')}{K(k)}, \tag{4.46}$$

capacitance

$$c_s = 4\epsilon_o \left[\frac{K(k)}{K(k')} + \frac{\epsilon_r - 1}{2} \frac{K(k_1)}{K(k_1')} \right], \tag{4.47}$$

and effective dielectric constant

$$\epsilon_{re} = 1 + \frac{\epsilon_r - 1}{2} \frac{K(k')}{K(k)} \frac{K(k_1)}{K(k_1')}, \tag{4.48}$$

where $k = \frac{S}{S+2W}$, $k' = \sqrt{1-k^2}$, and $k_1 = \sinh(\frac{\pi S}{4H}) / \sinh[\frac{\pi(S+2W)}{4H}]$, the inductance l_s is found to be

$$l_s = Z_o^2 c_s = \frac{\mu_o}{4} \frac{K(k')}{K(k)}. \tag{4.49}$$

The required inductance derivative would not be simply $\frac{\partial l_s}{\partial S}$, where S is now the strip width. Instead, the ground plane edges can now be considered and incremented. These changes will cause a decrease of gap width W on each side of the gap. If all the edges are the same for each respective structure, the

correct form of (4.41) is

$$\alpha_{c2} - \alpha_{c1} = \frac{-R_s\left(\frac{\partial l_s}{\partial S} - \frac{\partial l_s}{\partial W}\right)}{2\mu\pi Z_o}\left[\ln\left(\frac{\Delta_1}{\Delta_2}\right)\right]. \tag{4.50}$$

One of the required derivatives, $\frac{\partial l_s}{\partial S}$, is found by the chain rule to be

$$\frac{\partial l_s}{\partial S} = \frac{\mu_o}{4}\left[\frac{K(k)\frac{dK(k')}{dk'}\frac{\partial k'}{\partial S} - K(k')\frac{dK(k)}{dk}\frac{\partial k}{\partial S}}{K^2(k)}\right], \tag{4.51}$$

where $\frac{\partial k'}{\partial S} = \frac{-WS}{\sqrt{WS+W^2}(S+2W)^2}$, $\frac{\partial k}{\partial S} = \frac{2W}{(S+2W)^2}$, and $\frac{dK(k)}{dk} = \frac{E(k)-(k')^2K(k)}{k(k')^2}$ [17]. The other derivative, $\frac{\partial l_s}{\partial W}$, is found analogously, where $\frac{\partial k'}{\partial W} = \frac{S^2}{\sqrt{WS+W^2}(S+2W)^2}$ and $\frac{\partial k}{\partial W} = \frac{-2S}{(S+2W)^2}$. The rectangular-edged loss is read, although not very precisely, from a graph [25] for a wide range of the normalized parameters $\frac{S}{H}$ and $\frac{W}{H}$. The stopping points Δ are once again obtained from Table 2.2. The results of the comparison are given in Figure 4.4. It is seen that the trapezoidal edges increase the loss, as expected, and the difference increases with decreasing width S while maximizing at small gap size W.

4.4 Comparison with the current integration method

The effect of edge shape on microstrip loss was examined according to the incremental width method in Figure 4.2. To compare the results from this method with the Lewin/Vainshtein current integration results, the current integrations were carried out for the edges of interest and compared. Results for a single normalized thickness, $\frac{T}{H} = 0.01$, are shown in Figure 4.5, along with the results from (4.41) in Figure 4.2 for the same thickness. An analysis of the results indicates that the two contrasting methods have roughly the same edge shape dependence over a wide range of strip widths. Thus, either of the two methods can be used for transmission lines in which both the infinitely thin inductance and current profile J_{zo} are known, while the incremental width method could be used in situations in which only the inductance is known.

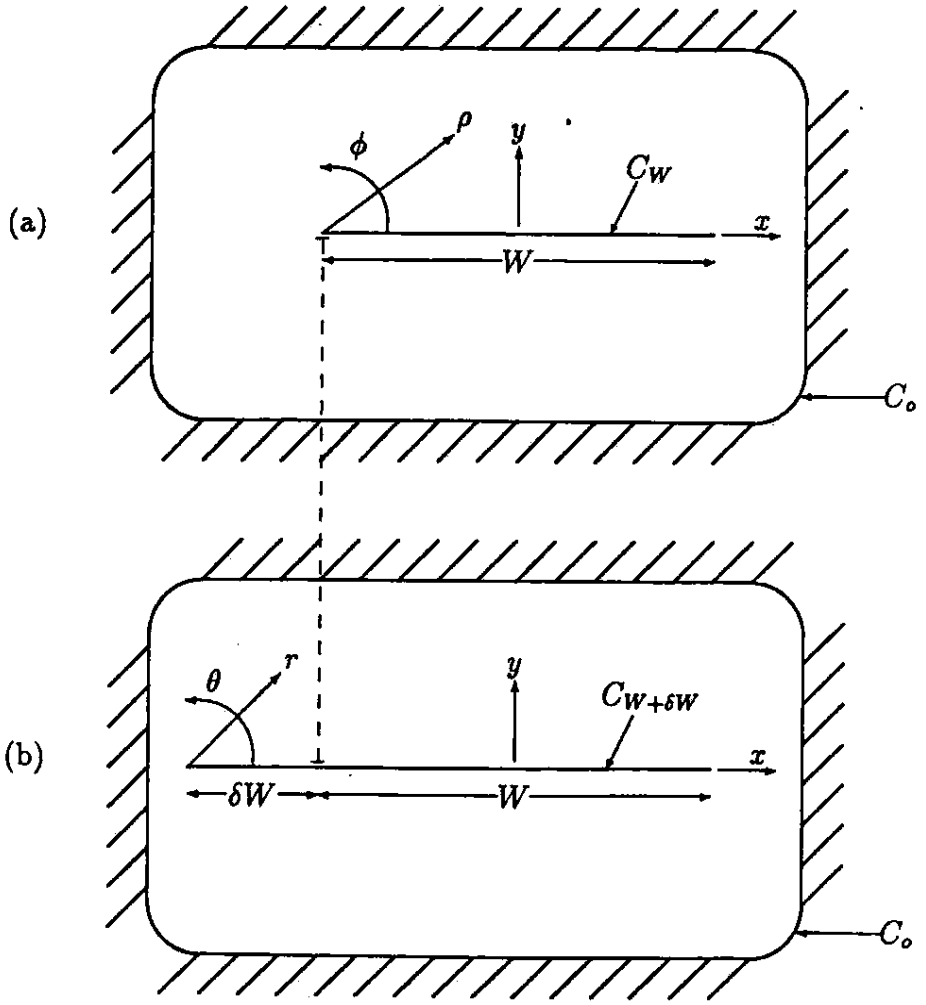

Figure 4.1. (a) First case, with strip of width W and cylindrical geometry (ρ, ϕ) centered at the left edge; (b) Perturbed case, having strip width $W + \delta W$ and a new cylindrical geometry (r, θ) centered at the new left edge.

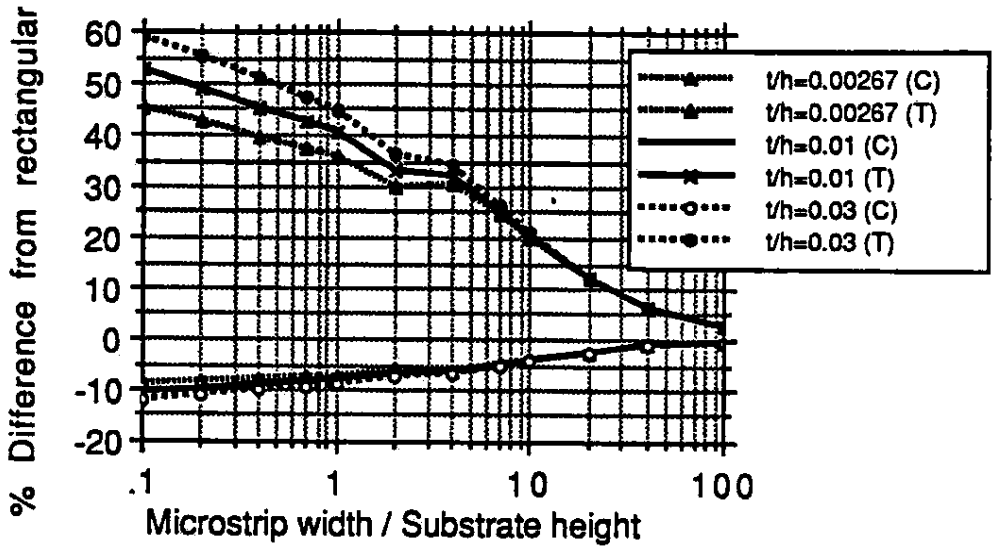

Figure 4.2. Comparison of loss between rectangular, circular, and 45° trapezoidal microstrip edges using the incremental width method. Shown in % difference from rectangular.

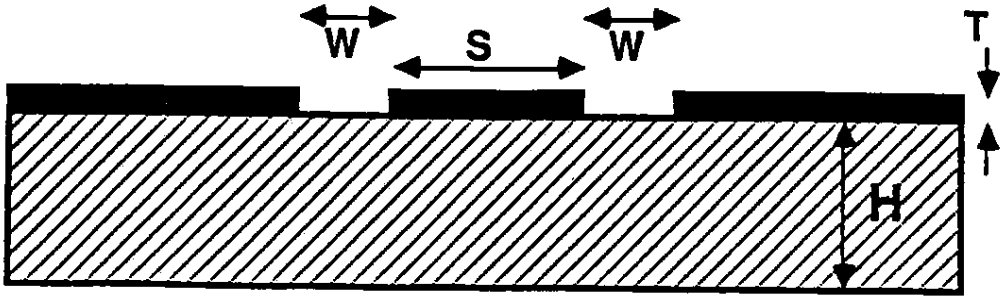

Figure 4.3: Geometry of the open coplanar waveguide.

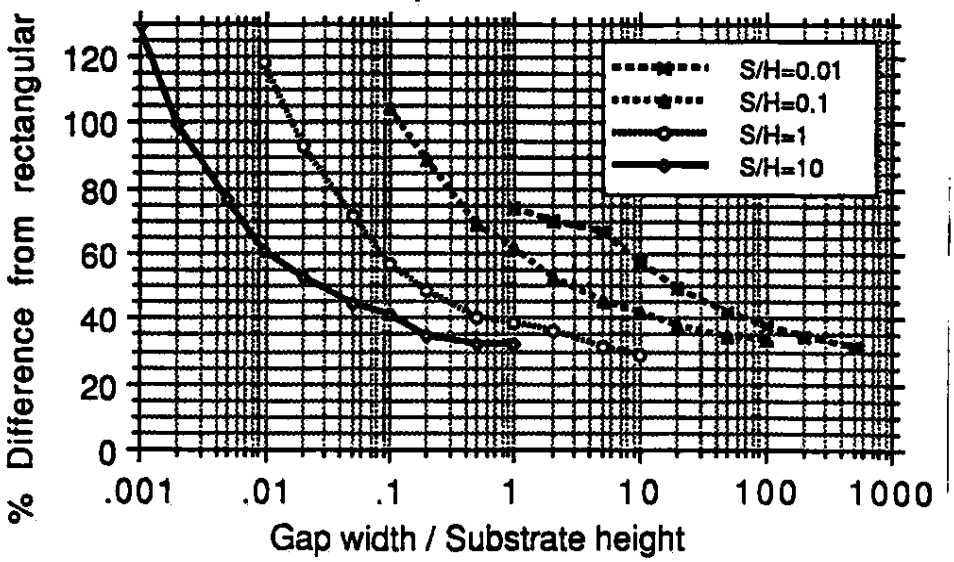

Figure 4.4. Comparison of loss between rectangular and 45° trapezoidal edges on open coplanar waveguide using the incremental width method. Shown in % difference from rectangular.

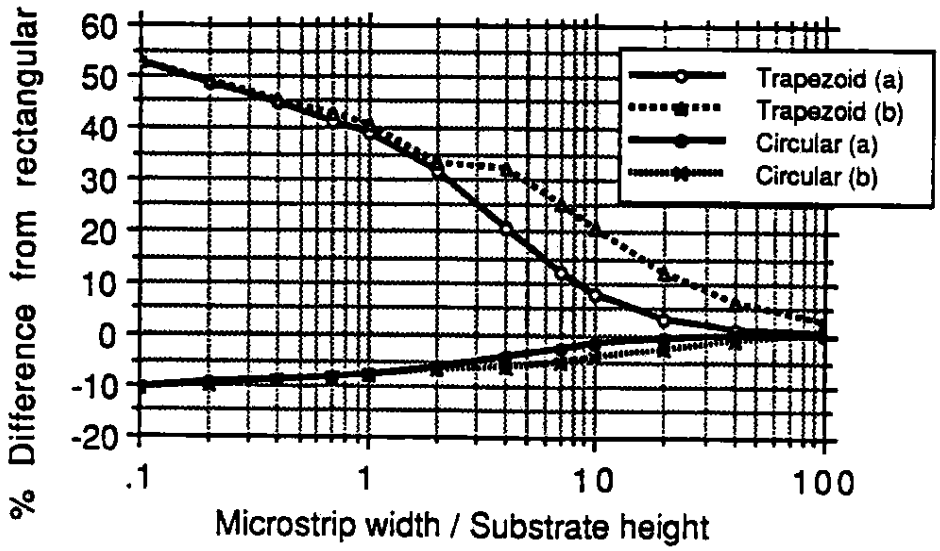

Figure 4.5. Comparison of loss between rectangular, circular, and 45° trapezoidal microstrip edges for $\frac{T}{H} = 0.01$ using both (a) last chapter's current integration method and (b) the incremental width method. Shown in % difference from rectangular.

CHAPTER 5

VALIDITY OF LEONTOVICH CONDITION AND PERFECT CONDUCTOR APPROXIMATIONS

5.1 Introduction

The results of the previous three chapters have been based on the assumptions listed in Chapter 1. It has been briefly mentioned that two of them, the surface impedance (Leontovich) boundary condition and the perfect conductor approximation, are particularly important and may be subject to question near the edges. Since it has been shown that the effect of edge shapes can drastically change conductor loss results, a further examination of these assumptions is necessary. Both of these assumptions will be reviewed and compared with relevant results, mostly numerical in nature, from the literature.

5.2 Perfect conductor approximation

5.2.1 Behavior of perfect conductor fields The approximation that the fields (and currents) at the surface of the finitely-conducting strip being equal to the fields of the perfectly conducting strip is described in Chapter 1. According to Meixner [3],[4], the perfectly conducting strip will have a surface tangential magnetic field $\overline{H}_{tan}$ and hence a longitudinal current singularity at the edge. This singularity is of the order r^{t-1}, where r is the distance from the edge and t depends on the edge angle $\nu\pi$ by $t = \frac{1}{2-\nu}$. The orders of the singularity for the various edges are listed in Table 5.1. Far from the edge, the total strip current J_{zo} should approach the $r^{-1/2}$ behavior of an infinitely

thin strip. However, the top and bottom strip current components $J_{zo,top}$ and $J_{zo,bot}$ should be distorted from that behavior in the presence of a ground plane.

The Schwarz-Christoffel transformations of Chapter 2 have been used to derive and integrate expressions for the current near the various edges. Since all of the singularities encountered in the actual strips are weaker than the $r^{-1/2}$ singularity that leads to a logarithmic divergence for the infinitely thin strip, the integration of the current squared $|J|^2$ were all bounded. The currents, given by $\frac{du}{dx}$, the inverse of the derivatives of (2.6) and (2.34)-(2.36), have been plotted for distances away from the various edges in Figures 5.1 and 5.2. Figure 5.2 demonstrates, for the isolated strip, how the current tends toward the $r^{-1/2}$ behavior sufficiently far from the edge. Assuming the current near the edge can be expressed by $|J_o|\, r^{t-1}$, asymptotic values of the constant $|J_o|$ have been found from numerical results for the various trapezoidal strips from the transformations of the coordinates and currents. These values are listed with the $|J_o|$ thickness dependences in Table 5.1. For the rectangular and 45° strip edges, approximations to first order in distance from the edges were obtained and are compared with the results below. For the 90° edge:

$$|J_{o,90°}| = \left(\frac{\pi}{8T}\right)^{2/3} \frac{2}{\sqrt[3]{12}} \approx 0.4685\, T^{-2/3}, \tag{5.1}$$

which is very close to the numerical value, and for the 45° and 135° edges encountered in the 45° strip:

$$\begin{aligned} |J_{o,45°}| &= \left(\frac{3\pi}{32T}\right)^{4/7} \left(\frac{5}{8}\right)^{3/7} \approx 0.4066\, T^{-4/7} \\ |J_{o,135°}| &= \left(\frac{3\pi}{32T}\right)^{4/5} \left(\frac{7}{8}\right)^{1/5} \approx 0.3662\, T^{-4/5}, \end{aligned} \tag{5.2}$$

which are relatively close to the values in the table.

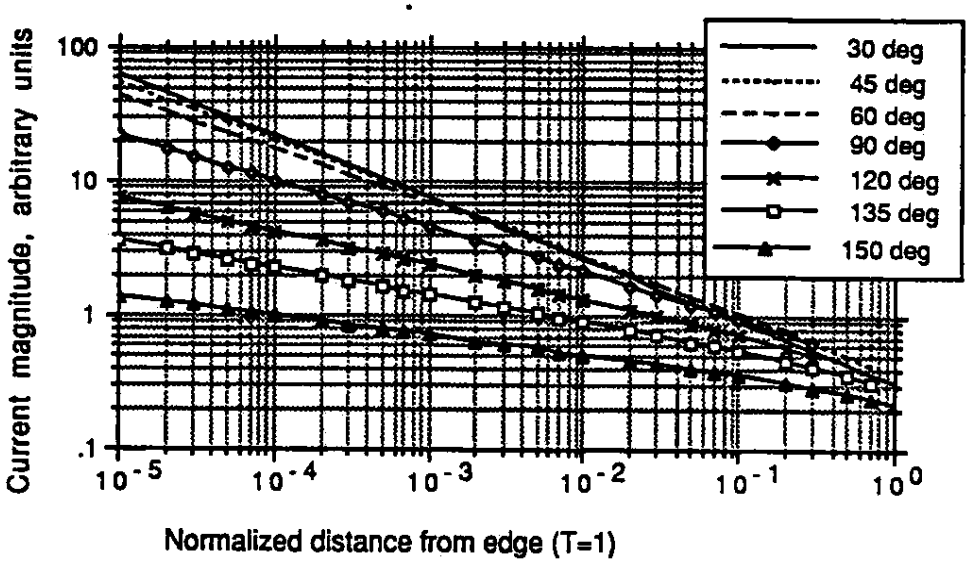

Figure 5.1. Magnitude of normalized currents near various edges against distance from the edges.

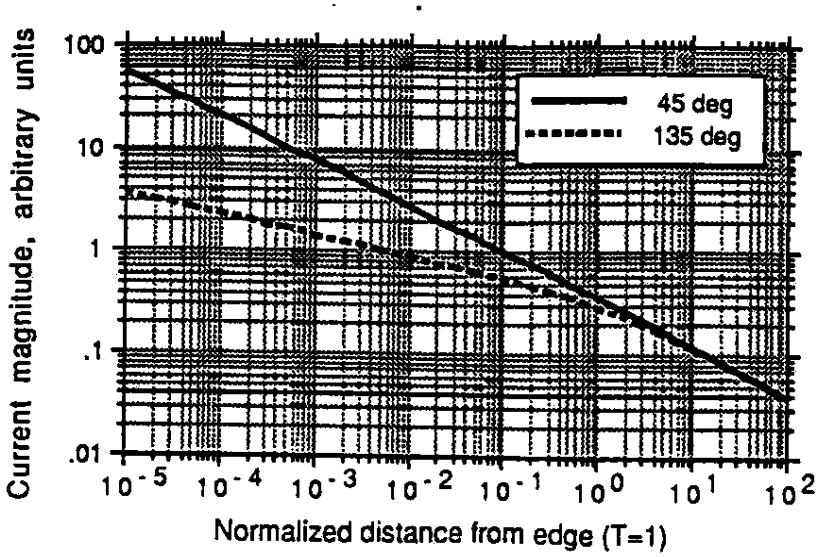

Figure 5.2. Magnitude of normalized currents for the 45° trapezoidal strip against distance from the edges.

Table 5.1. Normalized currents of perfect conductor for various trapezoidal edges.

Strip edge shape	x of $\lvert J_o\rvert/r^x$	y of T^y in $\lvert J_o\rvert$	$\lvert J_o\rvert_{T=1}$
Rectangular edge	1/3	-2/3	0.4684
60° edge	2/5	-3/5	0.4334
120° edge	1/4	-3/4	0.4225
45° edge	3/7	-4/7	0.3912
135° edge	1/5	-4/5	0.3593
30° edge	5/11	-6/11	0.3308
150° edge	1/7	-6/7	0.2652

5.2.2 Behavior of imperfect conductor fields In the actual case of an imperfect conductor, these singularities do not exist, according to various authors [26]-[29]. As a result, the importance of edge shape would decrease, if the surface impedance condition is still maintained.

Chisholm [26] expands the longitudinal components of the fields both inside and outside a circular wedge waveguide in a power series in r, the distance from the edge. After examining the resulting eigenvalues, he concludes that a coupled mode must exist in the finitely conducting case, and that the coupled tangential magnetic field H_r^e is large only near the edge. In fact, at the edge, H_r^e is the negative of the perfectly conducting H_r^o, so the total H_r and longitudinal current is zero at the edge. An expression and graph of the total H_r are given, showing how near the edge H_r peaks before H_r^e becomes large and decreases H_r to zero at the edge, but unfortunately the expression depends on the diameter of the wedge waveguide. This is not correct, and the effect of a peak in H_r before a decrease near the edge should be an edge effect only.

Faraji-Dana and Chow [27] use a separation of variables method and the moment method to demonstrate that as the normalized frequency, which depends on the conductivity as well as the actual frequency, becomes larger, the

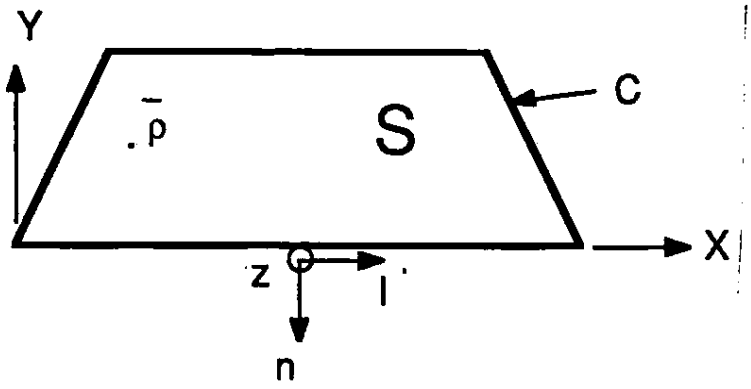

Figure 5.3. Conducting region S with boundary C and coordinates $\overline{a}_n$, $\overline{a}_l$, and $\overline{a}_z$. Observation point $\overline{\rho} = (x, y)$ is in S.

growth of the tangential magnetic field near a rectangular edge tends toward the predicted $r^{-1/3}$ variation. However, this behavior ceases at small enough r and J_z is not singular.

Fawzi et al. [28] use an integral equation and boundary elements technique to graphically demonstrate the same non-singular behavior of H_{tan} and J_z, even predicting a nonzero, finite result for H_{tan} at the edge. Numerical results show that H_{tan} peaks between $0.5 - 0.8\ \delta$ (skin depths) from the edge, while the longitudinal current J_z peaks around $0.1\ \delta$ and surface power density somewhere in between. The deviation of H_{tan} from the perfectly conducting case is mainly in the region $r < 2\delta$, and this is demonstrated in each of the above. Similar numerical results are given by [29].

5.3 Leontovich surface impedance approximation

5.3.1 Development of a nonlocal boundary condition for the rectangular edge Suppose that a conducting region S with boundary

C and parameters ϵ_m, σ_m, and μ_m, as seen in Figure 5.3, operates under quasi-TEM conditions so all fields have only a dependence of $e^{-i\beta z}$. Let a Green's function $G(\overline{\rho},\overline{\rho}')$ satisfy

$$\left(\nabla^2+\zeta^2\right)G=-\delta(\overline{\rho}-\overline{\rho}') \tag{5.3}$$

with a boundary condition $\frac{\partial G}{\partial n'}=0$ on the surface ($\overline{\rho}'\in C$). Since a two-dimensional Green's function is relevant, $\nabla\rightarrow\nabla_{xy}$ only, and $\zeta^2=k_m^2-\beta^2$, where

$$k_m^2=\omega^2\mu_m\left(\epsilon_m-i\,\frac{\sigma_m}{\omega}\right) \tag{5.4}$$

is the conductor wavenumber. If $\overline{E}_m$ and $\overline{H}_m$ satisfy Maxwell's equations in the metal, and so the Helmholtz equation

$$\left(\nabla^2+\zeta^2\right)E_{mz}=0 \tag{5.5}$$

is satisfied, then for the Green's function G and from Green's theorem,

$$E_{mz}(\overline{\rho})=\oint_C G(\overline{\rho},\overline{\rho}')\,\frac{\partial E_{mz}(\overline{\rho}')}{\partial n'}\,dl' \tag{5.6}$$

inside the metal. On the surface C, the boundary conditions require continuous tangential $\overline{E}$, normal $\overline{D}$, and tangential $\overline{H}$. Dropping the subscript m for all fields and parameters outside the conductor, the boundary conditions on the surface C are

$$E_{mz}=E_z,\quad H_{ml}=H_l, \tag{5.7}$$

and, for the case of high conductivity of the metal,

$$E_{mn}=\frac{\epsilon}{\epsilon_m-i\,\sigma_m/\omega}\,E_n\approx 0. \tag{5.8}$$

From the l component of Faraday's law in the metal,

$$\frac{\partial E_{mn}}{\partial z}-\frac{\partial E_{mz}}{\partial n}=-i\omega\mu_m H_{ml}=-i\omega\mu_m H_l=-i\omega\mu_m J_{sz}\approx\frac{-\partial E_{mz}}{\partial n}, \tag{5.9}$$

where $J_{sz} \equiv H_l$ is the equivalent surface current on the surface C. Letting the observation point be on the surface C ($\overline{\rho} \to C$), (5.6) is simplified to

$$E_z(\overline{\rho})|_C \approx i\omega\mu_m \oint_C G(\overline{\rho},\overline{\rho}')\, J_{sz}(\overline{\rho}')\; dl'. \tag{5.10}$$

If the conductor S were infinite in extent, then the Green's function G would be the two-dimensional infinite Green's function

$$G_\infty(\overline{\rho},\overline{\rho}') = -\frac{i}{4}\, H_o^{(2)}(\zeta|\overline{\rho}-\overline{\rho}'|). \tag{5.11}$$

If the space S were the upper half-plane $y > 0$ and C is the x-axis, then from image theory $G_\pi = 2G_\infty$ for $\overline{\rho}' \in C$. This would remain approximately true for an arbitrary region S if there are no corners in C so that (a) it is locally flat on the scale of $|\zeta|^{-1}$, or roughly a skin depth, and (b) the "diameter" of S is large compared to a skin depth. If these conditions are true, then J_{sz} is slowly varying, and, like [26], the Leontovich surface impedance can be derived:

$$E_z(\overline{\rho})|_C \approx \frac{\omega\mu_m}{2}\, J_{sz}(\overline{\rho}) \oint_C H_o^{(2)}(\zeta|\overline{\rho}-\overline{\rho}'|)\; dl' = \frac{\omega\mu_m}{2}\, J_{sz}(\overline{\rho}) \int_{-\infty}^{\infty} H_o^{(2)}(\zeta|l'|)\, dl'. \tag{5.12}$$

If an approximation to the Hankel function

$$H_o^{(2)}(\zeta|\overline{\rho}-\overline{\rho}'|) \approx \frac{2}{\zeta}\,\delta(l-l') \tag{5.13}$$

is made, then

$$E_z(\overline{\rho}) \approx \frac{\omega\mu_m}{2}\, J_{sz}(\overline{\rho})\, \frac{2}{\zeta} = Z_s J_{sz}(\overline{\rho}), \tag{5.14}$$

where

$$Z_s \equiv \frac{\omega\mu_m}{\zeta} = \sqrt{\frac{\mu_m}{\epsilon_m - i\,\sigma/\omega}} \tag{5.15}$$

is the standard Leontovich surface impedance.

If C does have corners, the Leontovich surface impedance is invalid because both J_{sz} is not slowly varying and the Green's function G_π is an

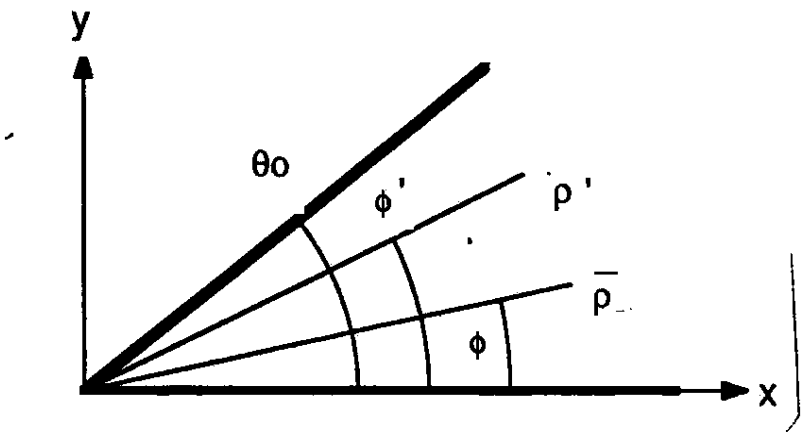

Figure 5.4. Coordinate system of θ_o° wedge, with source point $(\overline{\rho}', \phi')$ and observation point $(\overline{\rho}, \phi)$.

inadequate approximation near the corner. If S is the interior of a wedge of angle θ_o, as shown in Figure 5.4, the proper Green's function G can be calculated by Sommerfeld's technique. For a corner with angle $\theta_o = \frac{\pi}{2}$, the Green's function is

$$\begin{aligned} G_{\pi/2}(\overline{\rho}, \overline{\rho}') &= -\frac{i}{4}\left[H_o^{(2)}\left(\zeta\sqrt{\rho^2+\rho'^2-2\rho\rho'\cos(\phi-\phi')}\right)\right. \\ &+ H_o^{(2)}\left(\zeta\sqrt{\rho^2+\rho'^2+2\rho\rho'\cos(\phi-\phi')}\right) \\ &+ H_o^{(2)}\left(\zeta\sqrt{\rho^2+\rho'^2-2\rho\rho'\cos(\phi+\phi')}\right) \\ &+ \left. H_o^{(2)}\left(\zeta\sqrt{\rho^2+\rho'^2+2\rho\rho'\cos(\phi+\phi')}\right)\right], \end{aligned} \tag{5.16}$$

which can be interpreted as two-dimensional free space Green's functions from the source point $\overline{\rho}'$ and its three image terms in the other three quadrants. When the source point is on the x-axis ($\phi' = 0$), the Green's function becomes

$$G_{\pi/2}(\overline{\rho}, \overline{a}_x x') = \frac{-i}{2} H_o^{(2)}\left(\zeta\sqrt{(x-x')^2+y^2}\right) - \frac{i}{2} H_o^{(2)}\left(\zeta\sqrt{(x+x')^2+y^2}\right), \tag{5.17}$$

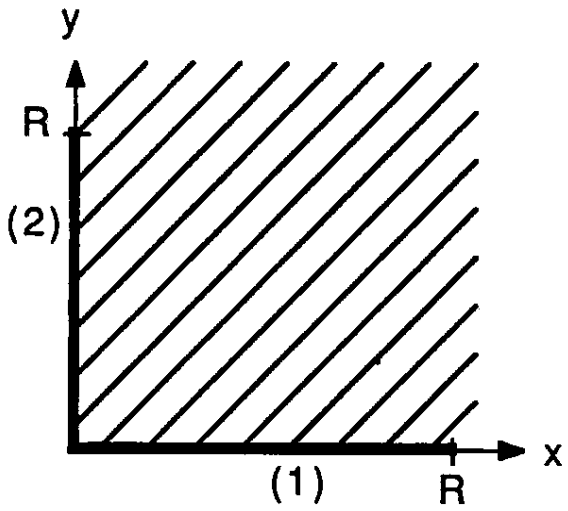

Figure 5.5: Coordinate system of 90° corner with faces 1 and 2.

and when it is on the y-axis ($\phi' = \frac{\pi}{2}$), it becomes

$$G_{\pi/2}(\overline{\rho}, \overline{a}_y y') = \frac{-i}{2} H_o^{(2)}\left(\zeta\sqrt{x^2 + (y-y')^2}\right) - \frac{i}{2} H_o^{(2)}\left(\zeta\sqrt{x^2 + (y+y')^2}\right). \tag{5.18}$$

The conductor loss near a square (90°) corner, as shown in Figure 5.4, may be found with more accuracy by using this Green's function to calculate the complex power into the segments from $y = R$ to $y = 0$ and from $x = 0$ to $x = R$, where R is some distance from the edge where the Leontovich condition is valid. It is desired that the result will be a modified, nonlocal surface impedance condition with two terms. The first term would be the Leontovich term, while the second would be a correction term.

The complex power into this corner is given by

$$P \equiv \int_0^R E_z(x) J_{sz}^{(1)*}(x)\, dx + \int_0^R E_z(y) J_{sz}^{(2)*}(y)\, dy, \tag{5.19}$$

where $J_{sz} = H_l$ on the surface. The portion from the bottom segment $x = 0$ to $x = R$ is given by

$$P^{(1)} \equiv \int_0^R E_z(x) J_{sz}^{(1)*}(x)\, dx = P_1^{(1)} + P_2^{(1)} + P_3^{(1)} \tag{5.20}$$

$$= \frac{\omega\mu_m}{2}\int_0^R J_{sz}^{(1)*}(x)\left[\int_0^R J_{sz}^{(1)}(x')[H_o^{(2)}(\zeta|x-x'|)+H_o^{(2)}(\zeta|x+x'|)]dx'\right]dx$$
$$+ \omega\mu_m\int_0^R J_{sz}^{(1)*}(x)\left[\int_0^R J_{sz}^{(2)}(y')\,H_o^{(2)}\left(\zeta\sqrt{x^2+y'^2}\right)\,dy'\right]dx.$$

If the first term is rewritten letting $u = x' - x$, and allowing $R \to \infty$ in the inner product, then

$$P_1^{(1)} = \frac{\omega\mu_m}{2}\int_0^R J_{sz}^{(1)*}(x)[\int_0^{\dot{\infty}} J_{sz}^{(1)}(x+u)H_o^{(2)}(\zeta u)du + \int_0^x J_{sz}^{(1)}(x-u)H_o^{(2)}(\zeta u)du]dx. \tag{5.21}$$

If the second term is similarly rewritten with $u = x' + x$, then

$$P_2^{(1)} = \frac{\omega\mu_m}{2}\int_0^R J_{sz}^{(1)*}(x)\int_x^\infty J_{sz}^{(1)}(u-x)H_o^{(2)}(\zeta u)du\,dx. \tag{5.22}$$

From (5.13), the Leontovich terms would come from

$$P_{Leon}^{(1)} = \frac{\omega\mu_m}{2}\int_0^R J_{sz}^{(1)*}(x)\,2\int_0^\infty J_{sz}^{(1)}(x)H_o^{(2)}(\zeta u)du = \frac{\omega\mu_m}{2}\int_0^R |J_{sz}^{(1)}(x)|^2\,\frac{2}{\zeta} = Z_s\int_0^R |J_{sz}^{(1)}(x)|^2dx. \tag{5.23}$$

So, by adding and subtracting this term,

$$P_1^{(1)} + P_2^{(1)} = Z_s\int_0^R |J_{sz}^{(1)}(x)|^2dx + \frac{\omega\mu_m}{2}\int_0^R J_{sz}^{(1)}(x) \int_0^\infty \left[J_{sz}^{(1)}(x+u) + J_{sz}^{(1)}(|x-u|) - 2J_{sz}^{(1)}(x)\right] H_o^{(2)}(\zeta u)du\,dx. \tag{5.24}$$

In this way, the power obtained can be expressed as a Leontovich term and a correction term consisting of the remaining components. Further simplification of the correction term was attempted at this point using the perfectly conducting current $J_{sz}^{(1)}(x) = |J_o|x^{-1/3}$. The result included many Gamma functions and reduced to

$$P_{Correction}^{(1)} = 1.1937\omega\mu_m|J_o|^2e^{-i\pi/6}\zeta^{-4/3}, \tag{5.25}$$

where $J_o = 0.4684\ T^{-2/3}$ from Table 5.1. This correction term has correct dependences on thickness T and ζ, and has argument of 150°, so, as anticipated, there is a decrease in power from the standard Leontovich condition. However, this cannot be used, since the currents do not behave as in a perfect conductor. Therefore, a numerical integration would most likely have to be performed once an acceptable solution of the current $J_{sz}^{(1)}(x)$ is obtained.

The derivation developed here can be applied to the general edge angle, although computation becomes significantly more difficult. The correct Green's function must be obtained for each angle, and then similar edge power correction terms may be found.

5.3.2 Published surface impedance studies Chisholm [26] derived a modified surface impedance condition,

$$E_z = Z_s(H_\tau^o + H_\tau^e), \tag{5.26}$$

which he claimed could be utilized throughout a surface to an edge. The first term, where H_τ^o is the magnetic field of the perfect conductor, is exactly the condition used in the first three chapters. The second term, containing the coupled magnetic field H_τ^e, is used to correct the total magnetic field and longitudinal current in an imperfect conductor. Actually, Chisholm uses the Leontovich impedance Z_s throughout, and his work is simply a correction to the longitudinal current. Unfortunately, that correction depends on the diameter of the wedge waveguide.

The numerical results by Fawzi et al. [28] included a scalar multiplication factor for the Leontovich impedance Z_s for a particular skin depth and set of aspect ratios with a rectangular edge. This factor increases from one far from the edge to just above two at the edge.

Deeley [30] has examined the surface impedance for both TE and TM modes, and for the latter case has developed curve-fitted empirical formulas from numerical results. The TM results, which are applicable here, demonstrate an exponential increase in the surface impedance $Z = \frac{E_z}{H_{tan}}$ up to two at the edge.

Zhurav [31] also recognized the failure of the Leontovich impedance near a rectangular edge. After expanding the fields inside a periodic lattice waveguide in the eigenvalues and outside the waveguide in a Fourier series, and by utilizing the boundary conditions, the complex roots of the characteristic equation are derived. Zhurav used this to add a correction term to the rectangular edge integration stopping point, Δ_{rect}, so that

$$\Delta_{rect,zhur} = \frac{T}{290.8}\left[1 + 0.32\left(\frac{2\delta}{T}\right)^{1/3}\right]. \tag{5.27}$$

A comparison of losses in a rectangular-edged strip using the two stopping points is given in Figure 5.6. In both, the Leontovich surface impedance Z_s is used on the entire infinitely thin strip, but the extra stopping distance length, due to a correction for the surface impedance, decreases the loss. In effect, Zhurav predicts a decrease in the Leontovich impedance near the edges, but in [32], as in [28] and [30], numerical results indicate that the impedance actually increases near the edge.

An application of a modified surface impedance condition using the previously developed integration stopping points has been developed by Slepyan [33],[34]. The Slepyan surface impedance is given by

$$Z = R_s - i\omega\mu_o\Delta, \tag{5.28}$$

where the real part retains the dissipative properties of the conductor and the

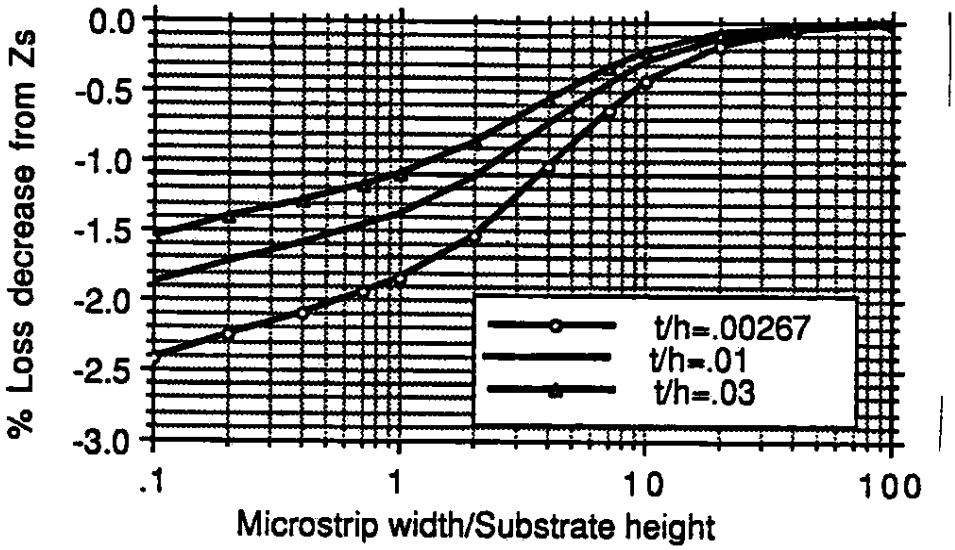

Figure 5.6. Comparison of losses on rectangular-edged strip using Chapter 3 techniques on both Δ_{rect} and Zhurav's stopping point correction.

imaginary part provides the correct current density near the edge for an infinitely thin strip. To obtain the imaginary part of the impedance, a technique similar to the derivation of Δ in Chapter 2 is used. The current squared of an infinitely thin strip, as obtained with the variable Z, is equated with the current squared of an actual strip, as obtained by conformal transformation. This impedance might be useful as a surface impedance for the entire length of infinitely thin strips in numerical codes, but, as in Chapter 3, the top and bottom components of current on the strip must be separated. This problem of division of the total current into its components has up to this point prevented the correct use of Slepyan's impedance to account for loss in those numerical codes.

5.4 Discussion

From the derivation of the integration stopping points Δ, the two approximations of a perfect conductor and the Leontovich surface impedance Z_s were examined. The currents of the perfect conductor, obtained near the various edges by the Schwarz-Christoffel transformation, were shown to agree with the Meixner edge singularities. According to various published results, there is indeed no singularity in the longitudinal current of the imperfect conductor. The current agrees with the perfect conductor current until within approximately two skin depths in a rectangular edge. Closer to the edge than that, the current peaks before reaching a finite value. Since much of the importance of edge shapes is in this range, it would seem that the current nonsingular behavior would decrease both the loss and the importance of edge shape.

Most numerical results show that the surface impedance $Z = \frac{E_z}{H_{tan}}$ increases from the Leontovich impedance Z_s within two skin depths of the edge to a value around $2Z_s$. Zhurav, on the other hand, finds that the impedance decreases. The increase in the surface impedance would cause an increase in loss around the edges, but coupled with the significant decrease in current magnitude in this range, the net total effect would still probably decrease the conductor loss and the edge shape importance from results predicted in Chapters 3 and 4.

What is needed is a numerical formulation, possibly continuing the work in Section 5.3.1, to incorporate a nonlocal surface impedance condition with a correct expression, although probably not closed-form, of the longitudinal current. This seems necessary since an analytical attempt to solve the problem has proven extremely difficult, if not impossible. From this should

come a new table of integration stopping points (Δ) as a function of edge shape and other factors such as skin depth and strip thickness. These points, once tabulated, could be used with any of the formulations developed in Chapters 2, 3, and 4 to accurately describe the effect of edge shape on conductor loss.

CHAPTER 6

EXPERIMENTAL PROCEDURES

6.1 Introduction

In order to verify some of the results above describing the effect of microstrip edge shape, careful experimentation was planned. Although the experiment in this project was not performed in the end, this chapter will describe some of the techniques and investigations done in preparation for the experiment.

A first guess at the method to measure microstrip conductor loss might be a direct two-port measurement of a uniform microstrip line. If there were a perfect match condition on this line ($S_{11} = S_{22} = 0$), the quantity $1-|S_{21}|$ could be directly attributed to loss, although not exclusively conductor loss. The problem is that the loss occurring in practical-sized circuits would be too small to measure accurately. The signal-to-noise ratio of this measurement would be unacceptable, so a different measurement must be performed. That measurement is a Q-measurement of a coupled microstrip resonator circuit.

In a microstrip resonator, a wave continues to reflect between two open-ended gaps, one or both of which being coupled to a feed line, and this establishing a standing wave. In this way, electromagnetic energy is stored, except for that energy lost in each cycle due to dielectric, conductor, and radiation losses. A resonator can be characterized by its resonant frequency f_r and its quality factor Q. The Q is a measure of the power lost per cycle and

can be related to the 3-dB bandwidth of the resonator by [35]

$$Q = 2\pi \frac{E_s}{P_l} = \frac{f_r}{BW}, \tag{6.1}$$

where E_s is the energy stored, and P_l is the power lost per cycle. Individual values of Q can be given to dielectric (Q_d), conductor (Q_c), and radiation (Q_r) losses, and these combine into the total Q_t by [35]

$$\frac{1}{Q_t} = \frac{1}{Q_d} + \frac{1}{Q_c} + \frac{1}{Q_r}. \tag{6.2}$$

The total Q is also called the unloaded Q, Q_0. When the resonator is coupled by one or more feed lines, the Q lowers to a value called the loaded Q, Q_L. The relationship between Q_0 and Q_L will be investigated in Section 1.5.

The dielectric loss is the best understood of the three components of loss, while the radiation loss, which will here include losses due to excited surface waves, is the least understood. Conductor loss has been widely measured, but the experimental effect of edge shape has not been reported in the literature. The goal here is to eliminate radiation loss, including surface wave loss, and account for dielectric loss. That which remains should be conductor loss. The elimination of radiation has been accomplished in [36],[37] by shielding the resonator in a waveguide in which the resonant frequency f_r is below the cutoff frequency $f_{c,WG}$. In this way, the excited radiation modes should be evanescent.

A preliminary investigation of this technique was performed using a ground plane backed duroid substrate and copper tape for the strip. This was done to study the various coupling schemes and Q-measurements, as well as experimental factors affecting reliability and repeatability. A study of a method to accurately control edge shape for the necessary comparisons was

done, and it was determined that the sizes of normal circuitry would not allow such control with the facilities available. As a result, an electromagnetic scaling experiment was proposed, in which the sizes involved would increase by a factor of 100, while the frequencies would decrease by that same factor. This idea is described further in the next section, but it was cancelled due to a lack of suitable materials.

6.2 Electromagnetic scaling

According to [38], an electromagnetic scale model experiment can be designed in order to make a certain configuration more manageable in the laboratory. Size and frequency are the parameters most often changed from the full-sized system by the factors k_l and k_ω, respectively. Similarly, k_E and k_H are the scaling factors for the original electric and magnetic fields. All other parameter scaling factors can be determined from these four scaling factors. When only the ratio k_E/k_H is specified, the model is called a geometric model, but when k_E and k_H are both specified, it is an absolute model. In a geometric model, in contrast to an absolute model, not all parameters can be exactly specified, such as voltage, current, and power, but the ratio of powers necessary to calculate attenuation constant can be obtained. Because of this, a geometric model was planned.

Other scaling factors which directly affect materials are the permeability factor $k_\mu = \frac{k_E}{k_H k_l k_\omega}$, the permittivity factor $k_\epsilon = \frac{k_H}{k_E k_l k_\omega}$, and the metal conductivity factor $k_\sigma = \frac{k_H}{k_l k_E}$. In both the original and the model, nonmagnetic materials are desired, so $k_\mu = 1$. Also in both, the region above the microstrip should be air, and so the dielectric scaling factor k_ϵ should be one. From these factors, the ratio k_E/k_H must equal one, and the size and frequency factors

are related by $k_\omega = 1/k_l$. As a result, the model transmission line parameters resistance R and characteristic impedance Z remain the same, but capacitance C and inductance L are divided by the factor k_ω.

The original problem was an attempt to model a gallium arsenide MMIC transmission line. The circuit considered had a substrate height and strip width of approximately 5 *mils* and a metallization of gold or copper with thickness 4 μm, operating at a frequency of approximately 100 GHz. Since careful control of the strip edge shape was desired, a metallization thickness that was accurately machinable for the hardness of that material was the primary consideration. It was determined that a thickness of 16 $mils = 400\ \mu m$ was barely acceptable, and so $k_l = 100$. The other dimensions of the model would be $W \approx H = 0.5\ in$, while the frequency becomes 1 GHz. The loss tangent of the dielectric remains the same, and so does its fraction of total loss. A substrate with as low a loss tangent as possible was desired to ensure that the conductor loss was dominant. A glass-like substrate ($\epsilon_r = 4.25$) of low loss ($\tan\delta < 0.0005$) and correct height was donated by Schott America. The problem in the model was to find a material with conductivity in the range of $5 \times 10^5 \frac{S}{m}$, approximately 1% that of gold. No suitable, machinable material was found anywhere in that range. The model ground plane could have been copper or some other metal with conductivity much greater than the strip, and that would have eliminated most of the model's ground plane conductor loss. The same is true with the shielding of the waveguide below cutoff. Using that high of a conductivity on the strip, however, would have prevented much of the strip conductor loss as well, and thus the accuracy of the conductor loss measurement would have suffered. Although it is the relative effect of a change

of edge shape which was being studied, a significant conductor loss was still necessary. As a result, the scaling experiment was cancelled.

6.3 Other losses

6.3.1 Dielectric loss As mentioned previously, other losses contribute to the total Q_t of the resonator, and must be removed to obtain the conductor loss. Dielectric loss is well known and can be readily calculated ([39]). The dielectric attenuation constant is given by

$$\alpha_d = 27.3 \frac{\epsilon_r}{\epsilon_r - 1} \frac{\epsilon_{re} - 1}{\sqrt{\epsilon_{re}}} \frac{\tan \delta_d}{\lambda_o} \quad \frac{dB}{m}, \tag{6.3}$$

where ϵ_{re}, the effective relative dielectric constant, is given by

$$\epsilon_{re} = \frac{\epsilon_r + 1}{2} + \frac{\epsilon_r - 1}{2} \left(1 + \frac{10H}{W}\right)^{-0.5}, \tag{6.4}$$

and λ_o is a free-space wavelength. The attenuation constant (in dB/m) is related to Q_d as well as an effective loss tangent $\tan \delta_{d,eff}$ by [25]

$$Q_d = \frac{27.3}{\alpha_d \lambda_o} = \frac{1}{\tan \delta_{d,eff}}, \tag{6.5}$$

where the effective loss tangent is related to the dielectric loss tangent by

$$\tan \delta_{d,eff} = \tan \delta_d \frac{\epsilon_r(\epsilon_{re} - 1)}{\epsilon_{re}(\epsilon_r - 1)}. \tag{6.6}$$

6.3.2 Other conductor loss factors In thin-film fabrication, often an adhesive layer of a metal different than the strip material must be deposited between the substrate and the strip conductor [25]. This adhesive layer, nominally between $0.02 - 0.1$ μm thick, is usually a metal of lower conductivity than the gold or the copper of the strip, for example, chrome or tantalum. This fact, although this layer is very much thinner than the

strip thickness, leads to an increase in conductor loss for the strip. Results of that increase are given in Figure 6.2 of [25], but in commonly used circuit dimensions, the increase in loss is small.

Another effect contributing to conductor loss is surface roughness of the substrate. Metal is deposited onto the substrate surface, and so it takes the shape of that surface. If the roughness is characterized by an effective roughness σ_{eff}, which is the root mean square of the roughness $\sigma(x)$, a further increase in attenuation constant can be found from Figure 6.3 of [25]. Duroid is a fairly rough substrate, and this was found to cause a significant increase in loss, but other common substrates such as alumina and gallium arsenide have relatively smooth surfaces, diminishing the magnitude of the increased loss.

A final contributing factor to increased conductor loss is the deviation of the conductivity from the bulk conductivity value. In general, processes such as electroplating and depositing will reduce the conductivity of the metal [37], sometimes to a significant extent.

6.3.3 Radiation losses Radiation due to the open ends of the resonator contributes a large fraction of the total power lost per cycle. It tends to increase with decreasing characteristic impedance, thicker substrates, lower relative dielectric constants, and higher frequencies. An expression for radiation power from an open end is given by Lewin [40], [41] as

$$P_r = 60(k_o h)^2 F_1(\epsilon_{re}), \quad F_1(x) = \frac{x+1}{x} - \frac{(x-1)^2}{2x^{1.5}} \ln\left(\frac{\sqrt{x}+1}{\sqrt{x}-1}\right). \qquad (6.7)$$

The radiation conductance is given by Sobol [42],[41] as

$$g_r = \frac{\sqrt{\epsilon_{re}}}{240\pi^2} F_2\left(\sqrt{\epsilon_{re}}\,\frac{2\pi}{\lambda_o} W_{eq}\right), \qquad (6.8)$$

where the equivalent strip width is $W_{eq} = \frac{120\pi H}{Z_o\sqrt{\epsilon_{re}}}$ and $F_2(x) = x\ Si(x) - 2\sin^2(x/2) + \frac{\sin(x)}{x} - 1$. When two open ends are combined into a resonator of length $n\lambda/2$, an easily utilized formula for Q which takes into account mutual coupling ([35],[41]) is

$$Q_r = \frac{nZ_o}{480\pi(H/\lambda_o)^2(1+m)F_1(\epsilon_{re})}, \tag{6.9}$$

where m, the mutual coupling factor, is given in Figure 5 of [41] as a function of electrical length between the open ends when $k_o\rho = \frac{n\pi}{\sqrt{\epsilon_{re}}}$. Van der Pauw [43] gives somewhat more difficult expressions for a half-wave linear resonator and a full-wave ring resonator. Equation (6.9) will be used, despite the fact that at least one of the resonator ends is coupled to a feed line, and so is not a true open end. When the feed line is end-coupled, the open-end approximation is even less valid.

Another component of radiation loss is surface wave excitation. The lowest order surface wave modes are TM_0 and TE_1. The TM_0 mode, which does not have a cutoff frequency but increases with frequency, has significantly less power than the other radiation modes, and can be neglected. The TE_1 mode, however, is more prominent and can be avoided by operating below its cutoff frequency [41]

$$f_{c,TE1} = \frac{c}{4H\sqrt{\epsilon_r - 1}}. \tag{6.10}$$

The surface wave power becomes appreciable when $H/\lambda_o > 0.09$ for $\epsilon_r \approx 2.3$ and $H/\lambda_o > 0.03$ for $\epsilon_r \approx 10$ ([44],[41]).

6.4 Choice of type of resonator

6.4.1 Ring and linear resonators In preparation for the experiment, a decision had to be made about whether to use a ring or linear

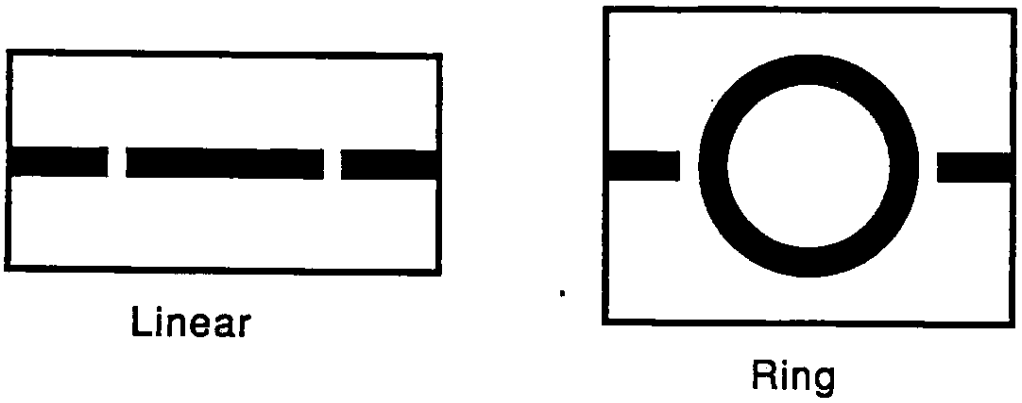

Figure 6.1: 2-port linear and ring resonators for transmission measurements.

resonator (see Figure 6.1). A ring resonator resonates when the circumference of the middle of the strip equals an integral number of guide wavelengths. The feed lines are coupled to the resonator by small gaps, causing a resonator voltage maximum to be at these locations. There is a minimum of radiation from these gaps, but the curvature of the resonator causes a large surface wave excitation. The linear resonator, on the other hand, radiates considerably at its open ends, one or both of which may be coupling gaps from the feed lines. Since there is no curvature, surface wave excitation is minimized. The resonances occur when the resonator length, including fringing effects, is an integral multiple of a half guide wavelength.

To study the differences between the two types of resonator, three circuits were designed, fabricated, and tested at 5 GHz. The first two were linear resonators of length $\frac{\lambda_{G,5GHz}}{2}$ and $\lambda_{G,5GHz}$, while the third was a ring resonator of mean circumference $3\lambda_{G,5GHz}$. Using microstrip synthesis formulas ([39]), a 50 Ω line was designed on a duroid ($\epsilon_r = 2.5$) substrate with loss tangent $\tan\delta_d = 0.002$ and surface roughness $\sigma_{eff} = 2.54\ \mu m$. Copper is the

Table 6.1: Theoretical and experimental comparison of resonator types.

Circuit	Q_d	$Q_{c,sm}$	$Q_{c,ro}$	Q_r	Q_{cd}	Q_{tou}	$Q_{o,the}$	$Q_{o,exp}$
Linear $\frac{\lambda_G}{2}$	568	798	400	120	235	227	79	83
Linear λ_G	568	798	400	501	235	226	160	147
Ring $3\lambda_G$	568	798	400	?	235	223	?	170

metallization, and no adhesive layer was used. The circuits were analyzed with the EESof Touchstone simulation software, as well as the theoretical formulas of Section 6.3. Theoretical radiation Q (Q_r) for the ring resonator was not obtainable, although relevant measurements were done by Van Heusen [37]. Finally, experiment was performed with the HP8510 network analyzer. All three circuits had two ports, and so transmission measurements were done according to the procedure of Section 6.5, with results for the unloaded Q, Q_o, being found. These are compared in Table 6.1, where Q_d and Q_r, the theoretical dielectric and radiation Q, are obtained from (6.3),(6.5), and (6.9); the smooth surface conductor Q, $Q_{c,sm}$, is obtained from Pucel's corrected formulas [1]; and an estimated roughness factor of 2 yields $Q_{c,ro}$. The combination of theoretical conductor and dielectric Q, Q_{cd}, is calculated for comparison with the result from Touchstone, Q_{tou}. The total theoretical unloaded Q, $Q_{o,the}$, can be compared to the experimental result, $Q_{o,exp}$.

A similar set of calculations and measurements were done with the same circuits at 10 GHz, so that each electrical length is multiplied by two. In this case, the theory for the linear resonators predicted $15-30\%$ more loss than was obtained in experiment.

Some observations can be made from these results. First, in these circuits, the conductor loss of interest is lower than both dielectric and radiation

loss, which is undesirable. Second, this is a very rough surface, which drastically increases the conductor loss, and the factor of two is a large guess which plays an important role. Also, lengthening the resonator seems to change the Q_o only by its effect on radiation. In addition, Touchstone seems to ignore the radiation from the gaps, considering them only as a π-network of capacitors instead of including a radiation conductance, and because it can not simulate a ring physically, it also ignores surface wave excitation by the ring. It seems to have been a relative stroke of luck that the experimental results at 5 GHz so closely matched theoretical predictions, since the results at 10 GHz differed significantly. It is encouraging to note that excluding radiation, both the ring and linear resonators predict the same loss.

6.4.2 Shielding with a waveguide below cutoff Obviously, the elimination of radiation is important, as is choosing a better substrate. The solution of shielding the resonator in a waveguide below cutoff [36], [37],[45] shows promise. For the reason that a linear resonator could easily be shielded in such a way, but the ring resonator, due to its larger two-dimensional size, could not, it has been decided that a linear resonator in a waveguide below cutoff is the optimal means of measurement.

This technique was attempted with the two linear resonators used before. Both transmission and reflection measurements were attempted, the latter being accomplished by removing the SMA connector of one port.

The transmission measurements suffer from some problems which prevent the waveguide from eliminating much of the radiated power, and so the shielded Q values do not increase much from the unshielded values. First, due

to the circuit sizes, the radiating gaps are not far from the ends of the waveguide, and the radiation modes are not fully attenuated. Second, due to the SMA connectors, contact between the waveguide and the ground plane could not be obtained, establishing a kind of TEM waveguide from which radiation can escape. As a result, the positioning of the circuit in the waveguide resulted in significant changes in the Q_0. Another factor, which will be discussed in Section 6.6, is that the feedline itself acts as a transmission line for the gap radiation.

As discussed in Section 6.5, reflection measurements should produce the same unloaded Q for a given resonator. The reflection measurements corrected for the problem of good ground plane to waveguide contact. Also, a longer waveguide section could be used, so the truly open end of the resonator was deep inside the waveguide. As a result, unloaded Q values of up to $Q_0 = 210$ were obtained, which is closer to the theoretical value around 230. This indicates that a good portion of the radiated power is being eliminated. According to Van Heuven [37], this value would not be affected by losses in the waveguide shielding, since those conduction losses are negligible and can be ignored.

6.5 Reflection and transmission measurements

Reflection or transmission implies the method of measurement of the resonator. Reflection measurements are done on resonators with a single launcher. Quantities such as S_{11} (Γ) and $VSWR$ are measured. Resonators with two launching ports are measured by transmission, since the second port would alter reflection measurements. The quantities of interest are either S_{21} or S_{12}. Typical measurements of each type are shown in Figure 6.2.

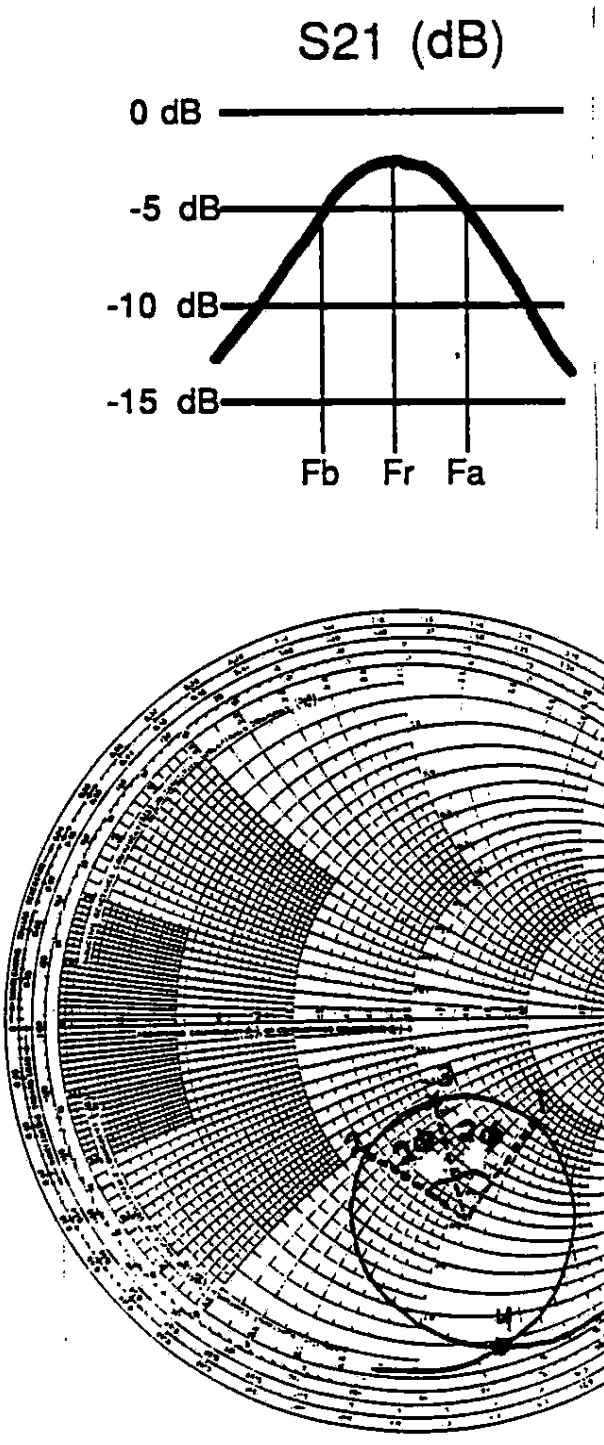

Figure 6.2. (a) Typical S_{21} transmission measurement with resonance and half-power frequencies, (b) Reflection measurement shown as Γ on the Smith Chart.

For a transmission measurement [25], the resonant frequency f_r is at the maximum transmission $|S_{21,max}|$. The points Fa and Fb in Figure 6.2a have a value of $|S_{21}|$ 3 dB below the maximum, and they correspond to the frequencies above ($f_{3dB,a}$) and below ($f_{3dB,b}$) the resonant frequency whose difference is the 3 dB bandwidth. Thus, the loaded Q is defined from (6.1) to be

$$Q_L = \frac{f_r}{BW} = \frac{f_r}{f_{3dB,a} - f_{3dB,b}}. \tag{6.11}$$

Coupling to the feed lines is measured by the coupling coefficient κ, which will be discussed further in Section 6.6. Assuming negligible losses in the system (connectors, adapters, and feed lines), the coupling coefficient is found from

$$\kappa = \frac{|S_{21,max}|}{2(1 - |S_{21,max}|)}. \tag{6.12}$$

Once the coupling coefficient is determined, the desired unloaded Q can be obtained from

$$Q_0 = \frac{Q_L}{1 - |S_{21,max}|} = Q_L(1 + 2\kappa). \tag{6.13}$$

Reflection measurements can be converted into Q_0 by one of two methods. A technique has been developed by Kajfez [46] and converted in Appendix 3 into easily utilized formulas. The method is based on the fact that the Smith Chart Γ response of Figure 6.2b nearly forms a circle. It is applicable when the feed gap is slightly undercoupled and is not too lossy, which is true when point 4 is close to the $\Gamma = 1$ border. Point 3 is at the resonance frequency f_r and its reflection coefficient there has magnitude $|\Gamma_r|$ and angle θ_r. Points 1 and 2, not in general the 3 dB points, and their corresponding frequencies f_1 and f_2, are found by finding the points on the curve closest to the following:

$$\Gamma_{f1} = \left(\frac{|\Gamma_r| + 1}{2}\right) e^{i\theta_r} + \left(\frac{|\Gamma_r| - 1}{2}\right) e^{i(\theta_r - 2\phi)} \tag{6.14}$$

$$\Gamma_{f2} = \left(\frac{|\Gamma_r|+1}{2}\right)e^{i\theta_r} + \left(\frac{|\Gamma_r|-1}{2}\right)e^{i(\theta_r+2\phi)},$$

where ϕ is some arbitrary small angle, as seen in Figure 6.2b, nominally $\phi = 20°$. Once these frequencies are obtained, the loaded Q is

$$Q_L = \frac{f_r}{f_1 - f_2}\tan\phi. \tag{6.15}$$

The coupling coefficient κ can be found from

$$\kappa = \frac{1-|\Gamma_r|}{1+|\Gamma_r|} = \frac{D}{2-D}, \tag{6.16}$$

where $D = 1 - |\Gamma_r|$ is the diameter of the approximate circle, or the distance from point 3 to the outside $|\Gamma| = 1$ border. From this, the desired unloaded Q is

$$Q_0 = Q_L(1+\kappa). \tag{6.17}$$

A different technique by Ginzton [47] examines the $VSWR$ measurements. By the same principles, the minimum $VSWR$, r_o, occurs at resonant frequency f_r. If the gap is undercoupled, then $\beta = 1/r_o$. The $VSWR$ at point 4 in Figure 6.2b is called r_{min}, and $\alpha = 1/r_{min}$. The parameter γ is equal to

$$\gamma = \frac{\alpha}{\beta} = \frac{r_o}{r_{min}}. \tag{6.18}$$

The 3 dB half-power points on the $VSWR$ curve have values

$$r_{1/2} = \frac{2+\beta^2(1+\gamma^2) + \sqrt{4+\beta^4(1+\gamma^4) - 2\gamma\beta^2(4-\gamma\beta^2)}}{2\beta(1+\gamma)}, \tag{6.19}$$

and the frequencies having these values are called f_1 and f_2. The loaded and unloaded Q are obtained by

$$Q_0 = \frac{f_r}{f_1 - f_2}, \quad Q_L = Q_0\left(\frac{1+\gamma\beta}{1+\beta}\right). \tag{6.20}$$

Table 6.2: Comparison of Kajfez and Ginzton reflection Q

	κ_{out}	$Q_{L,out}$	$Q_{O,out}$	κ_{in}	$Q_{L,in}$	$Q_{O,in}$
Kajfez	0.2079	90.0	108.6	0.405	198.0	278.3
Ginzton	0.2079	100.7	118.5	0.405	210.9	289.8

A comparison of these two methods was done for a copper tape resonator measured both inside and outside a waveguide below cutoff, and the results are given in Table 6.2. Kajfez's technique makes the approximation that the Γ curve forms a circle which is tangent to the $|\Gamma| = 1$ border, thus neglecting the coupling loss radiation. Still, that method predicts losses which are greater than those predicted by Ginzton. The Kajfez method has been chosen for these experiments.

Because Touchstone neglects radiation, a comparison of reflection and transmission measurements shows that the Q_0 of both should be equal in both the ring and linear resonators. In actuality, experiments in which two-port copper tape resonators were measured, and then measured as one-port devices after one of their feed lines were removed, showed that transmission Q_0 was slightly lower both inside and outside the waveguide shielding. Perhaps this was due to losses in the system, since the measurement is dependent on the magnitude of S_{21}. This will be investigated in Section 6.7. The reflection Q_0 showed somewhat more stability in measured values, both shielded and unshielded.

6.6 Resonator feeding mechanisms

For the case of a lossless coupling mechanism modelled by a π-network as in Touchstone, the resonator unloaded Q should be independent of the size of the gap. In actuality, radiation should change with the size of the gap, thus

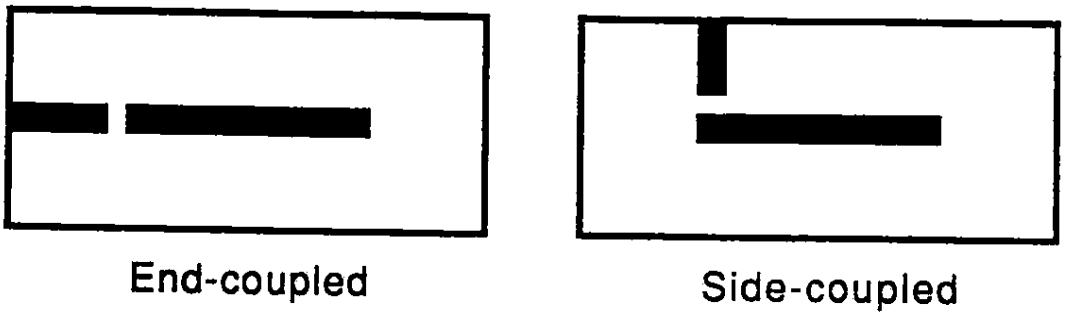

Figure 6.3. One-port linear resonators for reflection measurements: end-coupled and side-coupled.

affecting Q_0. A gap which is too large is called undercoupled ($\kappa < 1$) and produces a reflection response such as in Figure 6.2b. On the other hand, an overcoupled gap ($\kappa > 1$) is too small and results in Γ curves with diameters $D > 1$. The optimal coupling for a resonator is called critical coupling ($\kappa = 1$), where the resonator is perfectly matched to the input port at resonance. The advantage of this type of coupling ([1], [47]) is that it suppresses spurious resonances caused by mismatch. As would be expected, by decreasing the gap size, which increases the coupling and κ, the loaded Q, Q_L, decreases according to both Touchstone and experiment. In addition, gap size changes seemed to affect the Q_0 of transmission measurements more $(20 - 25\%)$ than the Q_0 of reflection measurements $(10 - 15\%)$.

Further effects examined were the length of the feed lines and the SMA connectors. According to experiment and Touchstone, the length of the feed line has very little effect on Q_0. If the SMA connectors are modelled as 0.2 nH inductors, the resonator Q does not change, but if radiation effects are included, losses will increase.

A final issue in the design of the experimental set-up was mentioned in Section 6.4.2. The feed lines can act as TEM waveguides to transport the gap radiation to the outside of the actual waveguide. The same can happen if good contact does not exist between the circuit ground plane and the waveguide floor. To correct these possible scenarios, first, good contact can be ensured by using some sort of conductive paste between the two metal surfaces. An attempt to reduce the feed line transport of radiation is to side feed the resonators instead of end feeding, as shown in Figure 6.3. This method, which was adopted by van Heuven [36],[37], assumes that most of the gap radiation is excited in the direction of the resonator, rather than to the side. A side feed could possibly reduce the amount of radiation transported to the outside, and instead allow most of it to be attenuated in the waveguide. Although a shielding jig to test this idea was not built, unshielded measurements were performed on copper tape resonators using alternatively end and side feed mechanisms. The losses when side feed lines were used averaged $5 - 10\%$ lower than the end feeds. Therefore, there was more radiation from the end gap than the side gap, which seems to agree with the tendency of transmission measurements (two end gaps) having more loss than reflection measurements (one end gap and one open end). As a result, the side fed linear resonator shielded in a waveguide below cutoff, as shown in Figure 6.4, was chosen, although not used.

6.7 Other experimental observations

During many of the above investigations, certain experimental effects were observed and studied. Most of the time, copper tape resonators, designed with very similar substrate material for 50 Ω, were utilized because of their versatility and ease of alterations. It was discovered that the Q_0 of the copper

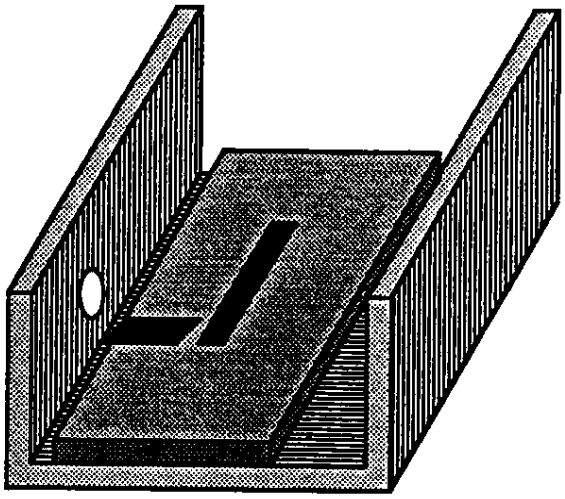

Figure 6.4. Final experimental choice: one-port linear resonator shielded in a waveguide below cutoff (top not shown).

tape resonators were slightly higher than the etched versions. This could not be readily explained.

To investigate the system losses, relevant especially to transmission measurements, a copper tape through line standard was built. The HP8510 calibrations were performed on its 7 *mm* connectors. This through line standard was a test of the $7 - 3.5$ *mm* adapters, the radiation from the SMA connectors and solder joints, and the copper tape, assumed to be 50 Ω. The resulting S_{11} and S_{22} were around -23 *dB*, while the S_{12} and S_{21} were about -0.55 *dB*. These results are fairly good, but not spectacular. While some of the transmission loss is expected from the copper tape strip, there apparently is other loss, and these results could account for the larger losses in transmission measurements.

It was found to be imperative to use the torque wrenches properly,

or results drifted wildly. The dependence of Q_0 on new (proper) calibrations, time (up to weeks), shaking of the circuit, and disconnecting and reconnecting the SMA connectors was less than 5%, so repeatability should be high. The SMA tab connections to the strip were more important, causing Q_0 to change by 10% for various contact qualities. Finally, the orientation of the unshielded circuit was very important. Turning the circuit so that the ground plane faced up resulted in differences in Q_0 of 20% or more.

In conclusion, although the experiment was cancelled, some valuable techniques were learned. It was found that repeatability of resonator Q measurements were fairly high as long as a few factors were kept constant. The shielded, side-fed, linear resonator was found to be the best measurement of loss available, and although reflection and transmission measurements were fairly close, reflection measurements may be the best choice.

CHAPTER 7

CONCLUSIONS AND FUTURE WORK

7.1 Conclusions

It has been found that the shape of the strip edge in microstrip should have a significant effect on conductor loss. In general, as the edge shape gets sharper, the loss increases. Under a set of approximations listed in Chapter 1, microstrip conductor loss can be easily calculated with some simple formulas convenient for computer-aided design.

Schwarz-Christoffel transformations have been developed for various trapezoidal edges in order to obtain the appropriate surface current distributions, and these have the edge singularities predicted by Meixner. These currents have been used to derive integration stopping points Δ, listed in Table 2.2, for loss calculations on an infinitely thin strip. Given an infinitely thin strip current distribution J_{zo}, (3.2) can be used to perform the calculations. The top and bottom strip current components are divided with a difference term δJ_{zo} given by (3.19), and J_{zo} and δJ_{zo} can be used to find loss in (3.20). Figure 3.7 shows these results for the various edge shapes, although the effect of edge shape seems larger than what would be expected.

An incremental width method has also been developed by a perturbation method from the perfect conductor current model. This technique is applicable when an inductance expression is available for a transmission line with an infinitely thin strip, and it is especially useful for cases where current

expressions are not readily available. The result (4.41) has been used to examine edge shape effect in open coplanar waveguide as well as microstrip. The two formulas (3.20) and (4.41) are in close agreement for microstrip.

The validity of these results is somewhat suspect, since they are based on a series of approximations which needed to be studied. Instead of having a shape-dependent singularity at each sharp edge, the longitudinal surface current actually peaks and then decreases in magnitude as it approaches the edge. Using the local Leontovich surface impedance condition up to the edge is wrong, and a nonlocal condition has been derived for a rectangular edge. From published results, it is expected that the surface impedance will increase near the edge.

A proposal for an experiment using the method of electromagnetic scaling is outlined. A linear side-coupled resonator in a waveguide below cutoff can be used to eliminate radiation loss so that conductor loss can be extracted. Either reflection or transmission measurements may be performed to extract the resonator quality factor Q_0, and hence loss, with a reasonable degree of repeatability.

7.2 Future work

The most important future direction of this project is the derivation of integration stopping points which do not take the assumptions studied in Chapter 5. Work on the rectangular edge can be extended beyond (5.20), and other edge shapes can be studied. The approximations fail only near the edges, so numerical techniques need be applied only to this area in order to tabulate new integration stopping points. Once these are compiled, all work in Chapters 2, 3, and 4 may be used with confidence, probably in a computer-aided design

environment. The results may be extended to other planar transmission lines as well.

A very promising extension of this work is the use of the modified surface impedance developed by Slepyan. If the top and bottom components of total strip current can be divided, numerical codes on infinitely thin strips could use these Δ points to correctly account for edge shape. Possibly a closed-form approximation of the division, based on the Chapter 3 results, can be developed to enable this technique to be feasible.

Finally, experimental verification of these theories is possible. If either suitable materials for a scaled experiment are found, or if precise, actual-sized edge shapes could be reliably controlled in fabrication, the effect of edge shape could be measured.

APPENDIX A

DERIVATION OF ATTENUATION CONSTANTS FROM $J_{ZO}(X)$ STRIP CURRENT PROFILES

A.1 Magnetic wall current model

The infinitely thin strip current profile under the magnetic wall model is given in (3.24). The integral of this distribution along the strip becomes the current I. Squaring the current profile yields

$$J^2_{zo,MW}(x) = \frac{I^2}{W^2}. \tag{A.1}$$

The integral of this quantity, excluding the stopping points, is

$$\int_{-W/2+\Delta}^{W/2-\Delta} \frac{I^2}{W^2} dx = \left[\frac{I^2}{W^2}\, x\right]_{-W/2+\Delta}^{W/2-\Delta} = \frac{I^2}{W^2}\,(W - 2\Delta), \tag{A.2}$$

which is the only quantity needed to derive (3.25) from (3.2), since $J_{zo,top}(x) = 0$.

A.2 Maxwell's current model

When the Maxwell's current distribution of (3.26) is integrated along the entire strip width, the current $I = 1$. The integral of this distribution squared is given by

$$\int_{-W/2+\Delta}^{W/2-\Delta} \frac{dx}{\pi^2(A^2 - x^2)} = \frac{1}{\pi^2}\left[\frac{1}{2A}\ln\left|\frac{x-A}{x+A}\right|\right]_{-W/2+\Delta}^{W/2-\Delta} = \frac{2}{\pi^2 W}\ln\left(\frac{W-\Delta}{\Delta}\right). \tag{A.3}$$

Half of this quantity is the $\frac{1}{2}J^2_{zo}$ term of (3.20).

A.3 Kuester/Chang current model

The current distribution (3.28) results in a total current of $I = C_p V$. To find the J_{zo}^2 term of (3.20), the integral of the current distribution squared,

$$\int_{-W/2+\Delta}^{W/2-\Delta} \left(\frac{\pi C_p V}{8Hk'K(k)}\right)^2 \frac{dx}{\cosh^2\left(\frac{\pi W}{8H}\right) - \cosh^2\left(\frac{\pi x}{4H}\right)}, \tag{A.4}$$

must be found. Removing constants and making the change of variable $x' = \frac{\pi x}{4H}$, the integral reduces to

$$\int \frac{dx}{\cosh^2\left(\frac{\pi W}{8H}\right) - \cosh^2\left(\frac{\pi x}{4H}\right)} = \frac{4H}{\pi} \int \frac{dx'}{a + b\cosh^2 x}, \tag{A.5}$$

where $a = \cosh^2\left(\frac{\pi W}{8H}\right)$ and $b = -1$. From (2.458.2) of [17], this integral becomes

$$\frac{4H}{\pi} \left[\frac{1}{\sqrt{a(a+b)}} \coth^{-1}\left(\sqrt{1+\frac{b}{a}}\coth x'\right)\right]_{-W/2+\Delta}^{W/2-\Delta}, \tag{A.6}$$

since $-1 < \frac{b}{a} < 0$ and $\cosh^2(x) < \frac{-a}{b} = a$. When this is evaluated and constants included, the result is given by 3.29.

A.4 Kobayashi's current profile

The normalized current distribution of Kobayashi is given by (3.30) and can be rewritten as

$$\frac{J_{zo}(x)}{J_{zo}(0)} = 1 + K_A\left(\frac{A}{\sqrt{A^2-x^2}} - 1\right) = 1 - K_A + K_A\frac{A}{\sqrt{A^2-x^2}}, \tag{A.7}$$

where

$$K_A = \frac{10\left(1-\frac{x_c}{A}\right)}{\frac{A}{\sqrt{A^2-x_c^2}} - 1} = \frac{10\left(1-\frac{x_c}{A}\right)\sqrt{A^2-x_c^2}}{A-\sqrt{A^2-x_c^2}}. \tag{A.8}$$

Integrating (A.7) over the strip width, the current I becomes

$$\begin{aligned} I &= [(1-K_A)x]_{-W/2}^{W/2} + K_A\left[\sin^{-1}\left(\frac{x}{A}\right)\right]_{-W/2}^{W/2} \\ &= (1-K_A)W + \frac{\pi K_A W}{2} \end{aligned} \tag{A.9}$$

The J_{zo}^2 term is found by integrating (A.7) squared, or

$$\int_{-W/2+\Delta}^{W/2-\Delta} \left[(1-K_A)^2 + \frac{K_A^2 A^2}{A^2-x^2} + \frac{2AK_A(1-K_A)}{\sqrt{A^2-x^2}}\right] dx \tag{A.10}$$

$$= \left[(1-K_A)^2 x + \frac{K_A^2 A^2}{2A} \ln\left|\frac{x-A}{x+A}\right| + 2K_A(1-K_A)\sin^{-1}\left(\frac{x}{A}\right)\right]_{-W/2+\Delta}^{W/2-\Delta}.$$

and the result when evaluated is given in (3.32).

APPENDIX B

ALTERNATIONS TO PUCEL'S FORMULAS TO EXTRACT GROUND PLANE LOSS

From [1], the formulas for normalized conductor attenuation constant can be altered to extract the ground plane contribution to the loss. These results are

$$\frac{\alpha_c Z_o H}{R_s} = \frac{8.68}{2\pi}\left[1-\left(\frac{W'}{4H}\right)^2\right]\left[\chi + \frac{H}{W'} + \frac{H}{\pi W'}\left(\ln\frac{4\pi W}{T} + \frac{T}{W}\right)\right], \quad \text{(B.1)}$$

for the range $\frac{W}{H} \leq \frac{1}{2\pi}$,

$$\frac{\alpha_c Z_o H}{R_s} = \frac{8.68}{2\pi}\left[1-\left(\frac{W'}{4H}\right)^2\right]\left[\chi + \frac{H}{W'} + \frac{H}{\pi W'}\left(\ln\frac{2H}{T} - \frac{\chi T}{H}\right)\right], \quad \text{(B.2)}$$

for $\frac{1}{2\pi} < \frac{W}{H} \leq 2$, and

$$\frac{\alpha_c Z_o H}{R_s} = \frac{8.68}{\left[\frac{W'}{H} + \frac{2}{\pi}\ln\left(2\pi e(\frac{W'}{2H} + 0.94)\right)\right]^2}\left[\frac{W'}{H} + \frac{\frac{W'}{\pi H}}{\frac{W'}{2H} + 0.94}\right] \left[\chi + \frac{H}{W'} + \frac{H}{\pi W'}\left(\ln\frac{2H}{T} - \frac{\chi T}{H}\right)\right] \quad \text{(B.3)}$$

for $\frac{W}{H} \geq 2$. Here $W' = W + \Delta W$, where ΔW is a thickness correction term to the width such that

$$\begin{aligned} \Delta W &= \frac{T}{\pi}\left(\ln\frac{4\pi W}{T} + 1\right), \quad \frac{W}{H} \leq \frac{1}{2\pi} \\ &= \frac{T}{\pi}\left(\ln\frac{2H}{T} + 1\right), \quad \frac{W}{H} > \frac{1}{2\pi}. \end{aligned} \quad \text{(B.4)}$$

When the ground plane loss is included, as in the original formulas, the parameter $\chi = 1$, however, when the ground plane loss is extracted and only the strip is considered, use $\chi = 0.5$.

APPENDIX C

DERIVATION OF REFLECTION Q_O FORMULAS

According to [46], the Γ response in Figure 6.2b nearly traces a circle, with point 3 the resonance with magnitude $|\Gamma_r|$ and argument θ_r. Point 4 has the same argument θ_r, and if it is approximated as being on the Smith Chart border $|\Gamma| = 1$ at a point $\Gamma_D = 1e^{i\theta_r}$, then the diameter D is equal to $1 - |\Gamma_r|$. Therefore, the center of this approximate circle is at the midpoint between point 3 and $\Gamma = 1e^{i\theta_r}$, or

$$\Gamma_{cen} = \frac{1e^{i\theta_r} + |\Gamma_r|e^{i\theta_r}}{2} = \left(\frac{1 + |\Gamma_r|}{2}\right) e^{i\theta_r}. \tag{C.1}$$

Suppose, as in [46], that two points (1 and 2) on the Γ curve exist, relatively close to the resonance point, and that the lines between these points and Γ_D form an angle of ϕ with the diameter along θ_r. Then, the radii to these points form an angle of 2ϕ with the radius along θ_r. The length of the radius is equal to half of the diameter, or

$$R = \frac{D}{2} = \frac{1 - |\Gamma_r|}{2}. \tag{C.2}$$

The arguments of the rays between the center and points 1 and 2 are given by $-\theta_r \mp 2\phi$, and so the locations of 1 and 2 on the Γ plane are given by

$$\left(\frac{|\Gamma_r| + 1}{2}\right) e^{i\theta_r} + \left(\frac{1 - |\Gamma_r|}{2}\right) e^{i(-\theta_r \mp 2\phi)} = \left(\frac{|\Gamma_r| + 1}{2}\right) e^{i\theta_r} - \left(\frac{1 - |\Gamma_r|}{2}\right) e^{i(\theta_r \mp 2\phi)}. \tag{C.3}$$

Very near these locations should be actual points on the Γ curve corresponding to the frequencies f_1 and f_2. Although Kajfez's technique will work for overcoupled resonators as well as undercoupled, these derived formulas will work only for slightly undercoupled gaps.

BIBLIOGRAPHY

[1] R. A. Pucel, D. J. Massè and C. P. Hartwig, 'Losses in Microstrip,' **IEEE Trans. Micr. Theory Tech.**, vol. 16, pp. 342-350, 1968. Correction in **IEEE Trans. Micr. Theory Tech.**, vol. 16, p. 1064, 1968.

[2] J. D. Kraus, **Electromagnetics.** New York, NY: McGraw-Hill, 1984.

[3] J. Meixner, 'The Behavior of Electromagnetic Fields at Edges,' **Inst. Math. Sci. Res. Rept. EM-72,** New York University, New York, NY, 1954.

[4] R. Mittra and S. W. Lee, **Analytical Techniques in the Theory of Guided Waves.** New York, NY: The Macmillan Company, 1976, chapter 1.

[5] H. A. Wheeler, 'Formulas for the Skin Effect,' **Proc. IRE**, vol. 30, pp.412-424, 1942.

[6] S. Ramo, J. R. Whinnery, and T. Van Duzer, **Fields and Waves in Communication Electronics.** New York, NY: John Wiley and Sons, 1984.

[7] E. F. Kuester and D. C. Chang, **Theory of Waveguides and Transmission Lines.** University of Colorado Electromagnetics Laboratory, 1990.

[8] R. E. Collin, **Field Theory of Guided Waves.** New York, NY: Mc-Graw Hill, 1960.

[9] M. Kobayashi, 'Longitudinal and Transverse Current Distributions on Microstriplines and their Closed-form Expression,' **IEEE Trans. Micr. Theory Tech.**, vol. 33, pp. 784-788, 1985.

[10] M. A. Leontovich, **Investigations of Propagation of Radiowaves, Part II.** Moscow, 1948.

[11] T. B. A. Senior, 'Impedance Boundary Conditions for Imperfectly Conducting Surfaces,' **Applied Scientific Research, Section B**, vol. 17, pp. 418-436, 1960.

[12] E. F. Kuester and D. C. Chang, 'Closed-Form Expressions for the Current or Charge Distribution on Parallel Strips or Microstrip,' **IEEE Trans. Micr. Theory Tech.**, vol. 28, pp. 254-259, 1980.

[13] L. Lewin, 'A Method of Avoiding the Edge Current Divergence in Perturbation Loss Calculations,' **IEEE Trans. Micr. Theory Tech.**, vol. 32, pp. 717-719, 1984.

[14] L. A. Vainshtein and S. M. Zhurav, 'Strong Skin Effect at the Edges of Metal Plates,'[Russian], **Pis'ma Zh. Tekh. Fiz.**, vol. 12, pp. 723-729, 1986 [Engl. transl. in **Sov. Tech. Phys. Lett**, vol. 12, no. 6, pp. 298-299, 1986].

[15] R. V. Churchill and J. W. Brown, **Complex Variables and Applications.** New York, NY: McGraw-Hill, 1984.

[16] P. Henrici, **Applied and Computational Complex Analysis, Vol. 1.** New York, NY: John Wiley and Sons, 1974, section 5.14.

[17] I. S. Gradshteyn and I. M. Ryzhik, **Table of Integrals, Series, and Products.** San Diego, CA: Academic Press, Inc., 1980.

[18] W. von Koppenfels and F. Stallman, **Praxis Der Konformen Abbildung.** Berlin: Springer-Verlag, 1959, pp. 207-209.

[19] M. V. Schneider, 'Microstrip Lines for Microwave Integrated Circuits," **Bell System Technical Journal**, vol. 48, no. 5, pp. 1421-1444, 1969.

[20] H. Kaden, 'Advances in Microstrip Theory,' **Siemens Forsch. u Entwickl. Ber.**, vol. 3, no. 2, pp.115-124, 1974.

[21] B. E. Spielman, 'Computer-aided Analysis of Dissipation Losses in Isolated and Coupled Transmission Lines for Microwave and Millimeter Wave Integrated Circuit Applications,' Naval Research Laboratory, Washington, DC, NRL Rep. 8009, 1976.

[22] W. Wiesbeck, 'Berechnung der Dämpfung ungeschirmter Streifenleitungen," **Wiss. Ber. AEG-TELEFUNKEN**, vol. 45, no.4, pp. 162-166, 1972.

[23] M. Chryssomallis, K. Siakavara, and J. N. Sahalos, 'A Study of Open Thick Microstrip: the Hybrid Quasistatic Approximation,' **Canadian Journal of Physics**, vol. 67, pp. 747-752, 1989.

[24] E. F. Kuester and D. C. Chang, **Electromagnetic Boundary Problems (ECEN 5144 Course Notes)**. University of Colorado Electromagnetics Laboratory, 1988.

[25] R. K. Hoffman, **Handbook of Microwave Integrated Circuits.** Norwood, MA: Artech House, 1987.

[26] R. M. Chisholm, 'Boundary Conditions and Ohmic Losses in Conducting Wedges,' **IRE Trans. Micr. Theory Tech.**, vol. ??, pp. 189-198, 1960.

[27] R. Faraji-Dana and Y. Chow, 'Edge Condition of the Field and A.C. Resistance of a Rectangular Strip Conductor,' **IEE Proceedings, Part H**, vol. 137, pp. 133-140, 1990.

[28] T. H. Fawzi, P. E. Burke, and M. T. Ahmed, 'Application of the BEM and Surface Impedance Method for the Computation of the High-Frequency TM Eddy Current Losses in Conductors with Edges,' **IEEE Trans. on Magnetics**, vol. 20, pp. 2010-2012, 1984.

[29] W. Kern, 'Skineffekt im ebenen Keilraum,' **Archiv für Elektrotechnik**, vol. 63, pp. 247-252, 1981.

[30] E. M. Deeley, 'Surface Impedance near Edges and Corners in Three-dimensional Media,' **IEEE Trans. on Magnetics**, vol. 26, pp. 712-714, 1990.

[31] S. M. Zhurav, 'Edge loss in Metal Plates of Rectangular Cross Section,'[Russian], **Pis'ma Zh. Tekh. Fiz.**, vol. 13, pp. 358-361, 1987 [Engl. transl. in **Sov. Tech. Phys. Lett.**, vol. 13, pp. 147-148, 1987].

[32] A. V. Tikhomirov and A. B. Manenkov, 'Skin Effect in a Wire of Square Cross Section, **Radiotekhnika i Elektronika**, vol. 34, pp. 1166-1171, 1989.

[33] A. S. Il'inskiy and G. Ya. Slepyan, 'Calculation of Joule Losses in Electrodynamic Systems with Thin Open Metal Surfaces,' [Russian], **Radiotekhnika i Elektronika**, vol. 31, pp. 670-675, 1986 [Engl. transl. in **Sov. J. Commun. Tech. Electron.**, vol. 31, pp. 68-73, 1986].

[34] G. Ya. Slepyan, 'More Precise Impedance Conditions for Calculating the Heat Losses in a Thin Open Metal Screen,'[Russian], **Radiotekhnika i Elektronika**, vol. 32, pp. 2446-2450, 1987 [Engl. transl. in **Sov. J. Commun. Tech. Electron.**, vol. 33, pp. 172-175, 1988].

[35] E. Belohoubek and E. Denlinger, 'Loss Considerations for Microstrip Resonators,' **IEEE Trans. Micr. Theory Tech.**, vol. 23, pp. 522-526, 1975.

[36] J. H. C. van Heuven and T. H. A. M. Vlek, 'Anisotropy in Alumina Substrates for Microstrip Circuits,' **IEEE Trans. Micr. Theory Tech.**, vol. 20, pp. 775-777, 1972.

[37] J. H. C. van Heuven, 'Conduction and Radiation Losses in Microstrip,' **IEEE Trans. Micr. Theory Tech.**, vol. 22, pp. 841-844, 1974.

[38] R. W. P. King and G. S. Smith, **Antennas in Matter.** Cambridge, MA: The MIT Press, 1981.

[39] K. C. Gupta, R. Garg, and I. J. Bahl, **Microstrip Lines and Slotlines.** Dedham, MA: Artech House, 1979.

[40] L. Lewin, 'Radiation from Discontinuities in Stripline,' **Proc. IEEE,** pp. 163-170, 1960.

[41] E. J. Denlinger, 'Losses of Microstrip Lines,' **IEEE Trans. Micr. Theory Tech.**, vol. 28, pp. 513-522, 1980.

[42] H. Sobol, 'Radiation Conductance of Open-circuit Microstrip,' **IEEE Trans. Micr. Theory Tech.**, vol. 19, pp. 885-887, 1971.

[43] L. J. van der Pauw, 'The Radiation of Electromagnetic Power by Microstrip Configurations,' **IEEE Trans. Micr. Theory Tech.**, vol. 25, pp. 719-725, 1977.

[44] J. James and A. Henderson, 'High-frequency Behavior of Microstrip Open-circuit Terminations,' **IEEE J. Microwave, Optics, and Acoustics,** vol. 3, pp. 205-218, 1979.

[45] E. J. Denlinger, 'Radiation from Microstrip Resonators,' **IEEE Trans. Micr. Theory Tech.**, vol. 17, pp. 235-236, 1969.

[46] D. Kajfez and E. J. Hwan, 'Q-Factor Measurement with Network Analyzer,' **IEEE Trans. Micr. Theory Tech.**, vol. 32, pp. 666-670, 1984.

[47] E. L. Ginzton, **Microwave Measurements.** New York, NY: McGraw-Hill, 1957.